Applications of the Wormlike Chain Model in Polymer Physics: Self-consistent Field Theory

by

Ying Jiang

A thesis
presented to the University of Waterloo
in fulfilment of the
thesis requirement for the degree of
Doctor of Philosophy
in
Physics

Waterloo, Ontario, Canada, 2013

AUTHOR'S DECLARATION

I hereby declare that I am the sole author of this thesis. This is a true copy of the thesis, including any required final revisions, as accepted by my examiners.

I understand that my thesis may be made electronically available to the public.

Abstract

The self-consistent field theory (SCFT) has reveived a great success in prediction of the physical properties of a variety of polymeric systems in the recent two decades. However, the traditional SCFT is based on the Gaussian chain model, completely neglecting the chain rigidity effects, which is ascribed to one of the intrinsic properties of polymer chains. This thesis concentrates on the development of SCFT in the framework of the wormlike chain model and studies the influence of the chain rigidity on the chain configuration which directly determines properties of polymer materials in the mesoscale. Firstly, considering Onsager-type, orientational-dependent repulsive interactions, we study a model for the isotropic-nematic interface in liquid-crystals. Through adjusting the ratio of total contour length L to the persistence length λ, we consider systems consisting of molecules with various degrees of flexibility: from rods to flexible chains. Physical properties such as the surface tension, interfacial width and density- and order-parameter profiles were numerically calculated as functions of the flexibility L/λ and tilt angle, which is defined as the angle between the interfacial normal and the nematic director. Secondly, We examine the influence of persistency on the phase diagram of AB diblock copolymers and the properties of the phase transition as a function of volume fraction, Flory-Huggins parameter and chain rigidity, covering a broad regime spanning from Gaussian chains to rigid rodlike chains. On one hand, we demonstrate that results from a Gaussian-weight based theory can be recovered in the long-chain limit, and on the other hand, we display that significant revisions to the phase diagram, due to the persistency effects, exist for shorter chains. To achieve this, an efficient numerical scheme is designed for implementing the calculations of the wormlike-chain SCFT in a full six-dimensional space.

Acknowledgments

I would like to express my gratitude to Professor Jeff Z. Y. Chen, for his patient supervision and the interesting topics he provided to me throughout my Ph.D. program. I also want to thank my thesis committee composed of Prof. Wing-Ki Liu, Prof. Don Sullivan and Prof. Marcel Nooijen, who have provided me many insightful suggestions on my work. Especially, I would like to thank Prof. Zhen-Gang Wang, Prof. Bae-Yeun Ha and Prof. Nasser M. Abukhdeir, who were the examiners in my oral examination. They provided me very helpful corrections for my thesis, which made this final version much better in literature. In addition, I would also like to thank support from my parents and brother as well. Especially, I am very much in debt to the emotional supports from my wife and my daughter. Furthermore, I also want to express thanks to my friends, Dr. Wu-Yang Zhang, Dr. Ming-Ge Deng, Mr. Yu-Cheng Su, Dr. Zi Jian Long and Dr. Sergey Mkrtchyan for their help in the completion of this thesis. Finally, I would like to thank the Natural Sciences and Engineering Research Council of Canada for financial support and SHARCNET for computational time.

Contents

List of Figures

Chapter 1

Introduction

1.1 Self-consistent field theory (SCFT) for polymers

Polymer chains consist of a sequence of many chemically repeating units (or monomers) through covalent bonds. A molecule composed of a single type of monomers is called *homopolymer*. The *block copolymer* is a polymer which has two or more types of identical monomers, linked together in block forms. The simplest block copolymers are AB diblock copolymers containing two types of constituent monomers A and B, *e.g.* A-A-A-A-B-B-B.

A scheme extensively used in modern computer simulation for polymers is the coarse-grained approach, in which a group of atoms are recognized as a larger particle (or segment). Fig. 1.1 shows a coarse-grained version of the polypropylene chain: a *bead-spring* model. Intuitively, a standard Monte Carlo (MC) or molecular dynamics (MD) simulation method [42] can be straightforwardly implemented based on the appropriate descriptions of polymer chain configurations and interactions between segments. However, MC and MD computations for the equilibrium properties of polymeric systems in large scale are always expensive, especially for a system where macro- or micro-phase separations are expected.

An alternative approach is the field-theoretic simulation (FTS), which smears

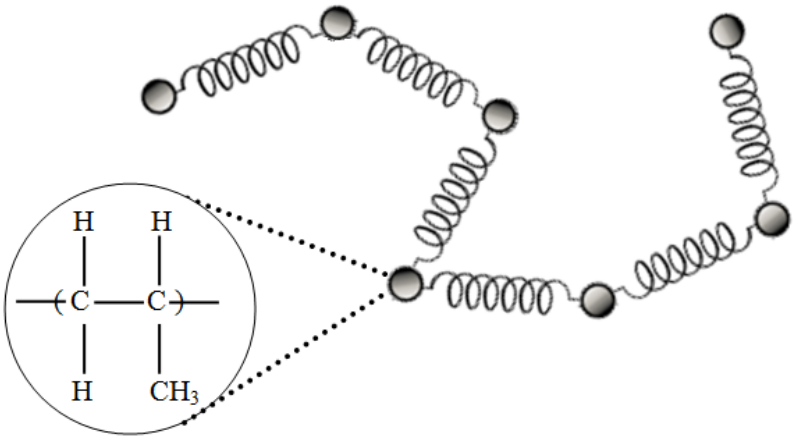

Figure 1.1: A coarse-grained scheme: the bead-spring model for a polypropylene chain.

out the segments uniformly along the polymer backbones so that a discrete nature (e.g. bead-spring model) can be transformed into a continuous model. The physical perspective of FTS is that the generalized coordinates on basis of particles, usually used in MC and MD methods, is integrated out from the partition function describing the chain statistics and is replaced by the auxiliary field functions conjugated to the molecular densities by a standard field transformation, the *Hubbard-Stratonovich transformation* [35]. Because of the difficulty of evaluating the partition function in the form of functional integrals, furthermore one commonly adopts the saddle point approximation, which takes the assumption that a *single* field configuration dominates the functional integrals of the partition function [40]. This approximation seems extremely poor for atomic or small molecule fluids, but it indeed works very well for concentrated polymer solution or melts made of polymers of high molecular weight. This mean-field approach is referred to as the *self-consistent field theory* (SCFT) [39], which needs to be solved either analytically or numerically.

SCFT employed in polymers can be traced back to Edwards' work [34] in 1965

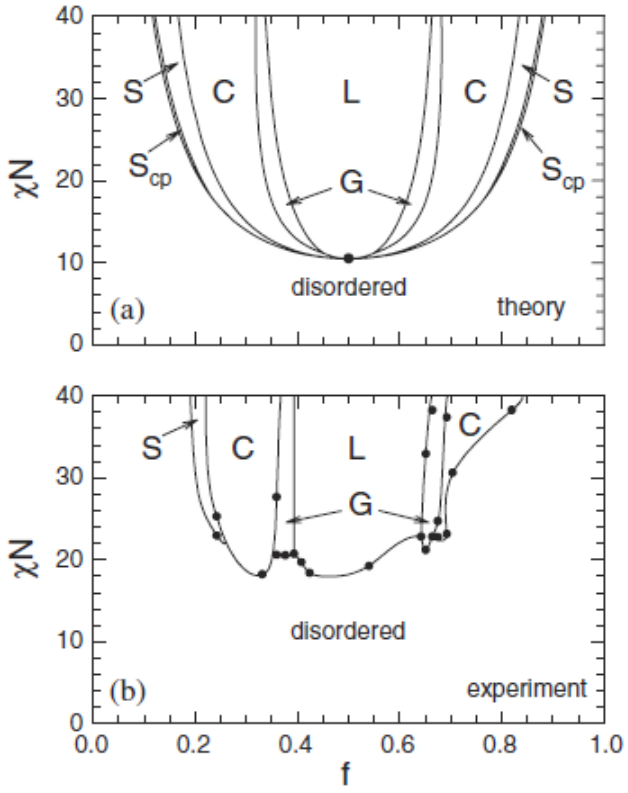

Figure 1.2: (taken from Ref. [73]) Phase diagrams of AB diblock copolymers from (a) the prediction of SCFT [77] and (b) experiment [6] in the coordinates of χN. χ and N represent the Flory interaction parameter and the polymerization of diblock copolymers, respectively. The volume fraction of component A is f. The phases shown in the figure are BCC spheres (S), close-packed spheres (S_{cp}), hexagonal cylinders (C), cubic gyroid (G), and lamellae (L). The experimental results are for a polystyrene-polyisoprene system [6].

and then was adopted by Helfand *et al* [55, 56, 54, 53] and Hong and Noolandi [60]. Since 1990s, SCFT has been successfully applied in the study of a variety of systems, such as blends, block copolymers, grafted copolymers, polymer brushes and polyelectrolytes [39], partially ascribed to the rapid development of computational capability. One remarkable feature of SCFT is that it is capable of calculating the free energy which is an important thermodynamic variable to determine physical properties of phase transitions and can be taken as a criterion to construct a phase boundary between different phases. One successful story is the prediction of the SCFT phase diagram of diblock copolymers, in agreement with the corresponding experimental results, as shown in Fig. 1.2. SCFT has been universally recognized as an indispensable theoretic tool to study the self-organization of polymers.

1.2 Wormlike chain (WLC) model

One of the most important and basic assumptions taken in the majority of previous theoretical studies based on SCFT is that the chain configuration is depicted by a Gaussian chain (GSC) model, as shown in Fig. 1.3. The polymer chain is depicted by a continuous space curve $\mathbf{R}(s)$, where $s \in [0, 1]$ is the contour variable which describes the location of a segment along the chain backbone. The stretching energy of a continuous GSC [31] reads

$$U[\mathbf{R}] = \frac{3}{2Na^2} \int_0^1 \mathrm{d}s \left| \frac{\mathrm{d}\mathbf{R}(s)}{\mathrm{d}s} \right|^2 \tag{1.1}$$

where $U[\mathbf{R}]$ denotes a functional of a space curve $\mathbf{R}(s)$. The mean-squared end-to-end vector for a GSC satisfies $R^2 = Na^2$, where a denotes the Kuhn length [38] and N is polymerization of a polymer chain. $(1/N)\mathrm{d}\mathbf{R}(s)/\mathrm{d}s$ can be looked as a local stretch of a segment with a length $N\mathrm{d}s$ at contour location s and then Eq. 1.1 is the summation of the harmonic potential of the differentiable segmental length over the whole backbone of the polymer chain. It is worth emphasizing that sN doesn't indicate the arc length in GSC model but a parameterized index along the chain. Thus, the magnitude of vector $(1/N)\mathrm{d}\mathbf{R}(s)/\mathrm{d}s$ is not constrained to be unity and is allowed to fluctuate freely.

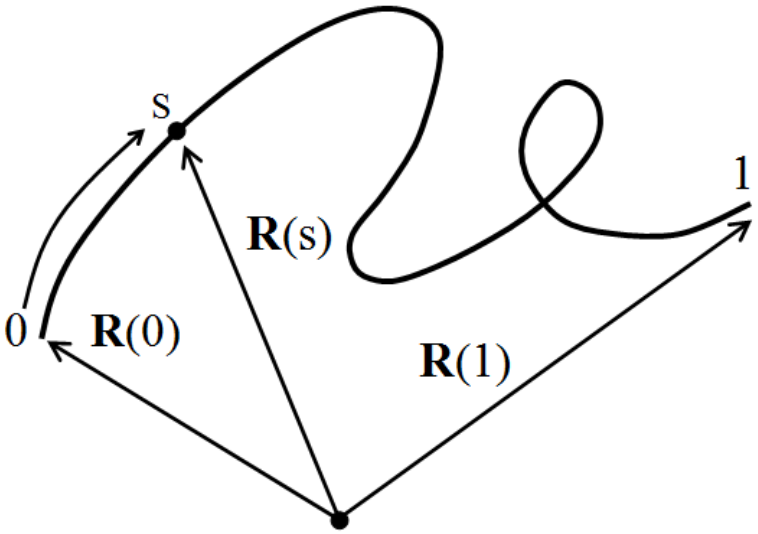

Figure 1.3: Continuous Gaussian chain model: a polymer chain is described by a space curve $\mathbf{R}(s)$, where $s \in [0, 1]$ is a contour parameter. The two ends of this chain are at positions $\mathbf{R}(0)$ and $\mathbf{R}(1)$, respectively.

A GSC model entirely neglects the orientational correlations between different segments and assumes that the polymer chain is extremely *flexible*. However, chain configurations of many biological and synthetic macromolecules such as conjugated polymers and polymers with polypeptide backbones, or aromatic groups tend to behave more like rigid or semiflexible chains. It is believed that the chain rigidity associated with the bending energy plays a crucial role in the phase behavior and conformation properties of polymeric systems [76, 43, 63]. Thus, in order to deal with such a system, a model considering the chain rigidity is desirable.

A suitable alternative model is the freely rotating chain (FRC) model [31] shown in Fig. 1.4(a), in which two successive segments with an *equal* bond length b are connected with a fixed angle θ but can rotate freely. As shown in Fig. 1.4(b), the $(i+1)$th bond vector $\triangle\mathbf{r}_{i+1}$ starting from the end of the ith bond vector $\triangle\mathbf{r}_i$ can terminate at anywhere on the circle of a cone. Then

$$\left\langle \triangle\mathbf{r}_i \cdot \triangle\mathbf{r}_{i+1} \right\rangle = b^2 \cos\theta \tag{1.2}$$

where the bracket $< \cdots >$ denotes the ensemble average. It is straightforward to

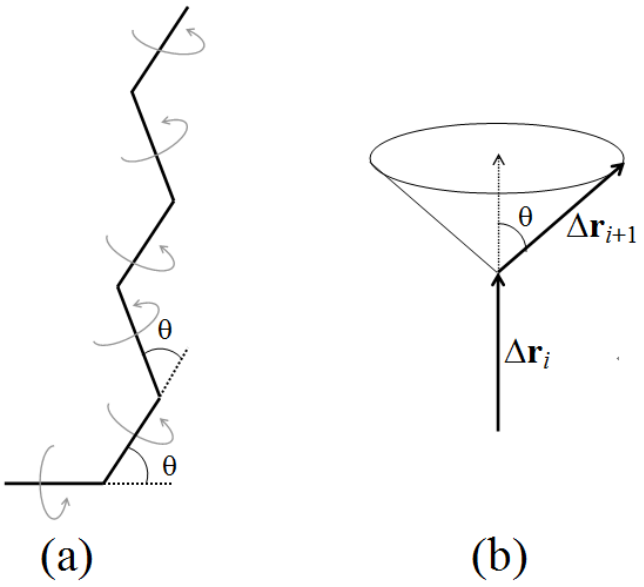

Figure 1.4: (a) Freely rotating chain. (b) Average of $\triangle\mathbf{r}_{i+1}$ for a given $\triangle\mathbf{r}_i$ gives $\triangle\mathbf{r}_i \cos\theta$.

.

arrive at the orientational correlation between two arbitrary bond vectors i and j

$$\langle \mathbf{u}_i \cdot \mathbf{u}_j \rangle = \cos^{|i-j|}\theta \tag{1.3}$$

Here, the orientation of the bond vector can be defined as $\mathbf{u} \equiv \triangle\mathbf{r}/b$ on account of the equal bond length assumed in the FRC model. In the limit of $\theta \to 0$, Eq. 1.3 can be reduced further into

$$\langle \mathbf{u}_i \cdot \mathbf{u}_j \rangle = \exp(-b|i-j|/\lambda) \tag{1.4}$$

where $\lambda \equiv 2b/\theta$ is the persistence length. This is the so-called wormlike chain (WLC) model, firstly proposed by Kratky and Porod [68] in interpreting small angle x-ray scattering measurements of polymer solutions. Thereafter, Saito, Takahashi, and Yunoki [100] generalized the WLC model into a continuous version, also referred to as the STY model. In this thesis, I concentrate on the applications of continuous WLC (i.e. STY) model in polymer physics.

In the STY model, a polymer chain is treated as an inextensible thread with a

fixed total contour length L, but the linear-elastic bending energy of each differentiable segment is taken into account. Similar to the continuous GSC model, the chain configuration in the STY model is also described as a continuous space curve $\mathbf{R}(s)$ where the arc length along the polymer backbone is denoted by sL. Again, the contour variable is set to be $s \in [0, 1]$. The vector $\mathbf{u}(s) \equiv (1/L)\mathrm{d}\mathbf{R}(s)/\mathrm{d}s$ represents the tangential direction of a chain at contour location s and is constrained to be a unit vector *i.e.* $|\mathbf{u}(s)| = 1$. The local curvature of a polymer at contour location s can be described by the magnitude of a vector $\mathrm{d}\mathbf{u}(s)/\mathrm{d}s = (1/L^2)\mathrm{d}^2\mathbf{R}(s)/\mathrm{d}s^2$. The bending energy of the STY model can be obtained by summing up the infinitesimal harmonic curvature terms along the chain

$$U[\mathbf{u}] = \frac{\lambda}{2L}\int_0^1 \mathrm{d}s \left|\frac{\mathrm{d}\mathbf{u}(s)}{\mathrm{d}s}\right|^2 \tag{1.5}$$

where the parameter λ is the persistence length. Then, the orientational correlation between contour location positions s and s' can be obtained [39]

$$\big\langle \mathbf{u}(s)\cdot\mathbf{u}(s')\big\rangle = \exp(-|s-s'|L/\lambda) \tag{1.6}$$

which shows that correlation of the orientation vector is lost with an increasing segment distance, as illustrated in Fig. 1.5. Now the physical significance of persistence length λ is clear. It is a length scale, describing the distance along the contour of a wormlike chain over which the orientational correlation exponentially decays

Eq. 1.6 leads to the calculation of mean-squared end-to-end vector for a WLC

$$R^2 \equiv \left\langle |\mathbf{R}(1)-\mathbf{R}(0)|^2 \right\rangle = L^2\int_0^1 \mathrm{d}s\int_0^1 \mathrm{d}s' \big\langle \mathbf{u}(s)\cdot\mathbf{u}(s')\big\rangle \tag{1.7}$$

Substituting Eq. 1.6 into this formula, we can conveniently obtain

$$R^2 = 2\lambda\Big\{L - \lambda\big[1-\exp(-L/\lambda)\big]\Big\} \tag{1.8}$$

which builds a continuous connection of the properties between the flexible chain and the rodlike chain. Note, in the following part we set a definition of Kuhn length

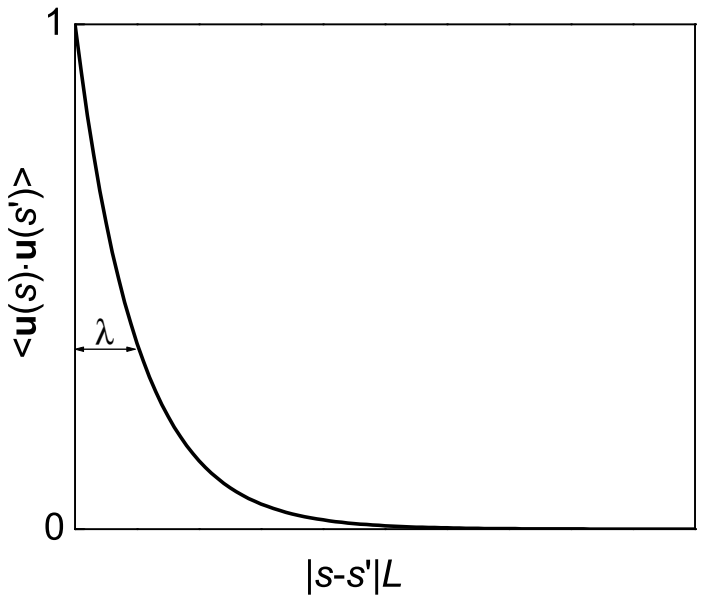

Figure 1.5: Orientational correlation function of a continuous WLC model.

$a \equiv 2\lambda$, in order to make a direct comparison to the GSC model. In the *flexible* limit $L/a \gg 1$, Eq. 1.8 reduces to

$$R^2 = aL \tag{1.9}$$

This is consistent with the corresponding prediction from the GSC model $R^2 = Na^2$, if we define the polymerization parameter $N \equiv L/a$. In the opposite (*i.e. rod*) limit $L/a \ll 1$,

$$R^2 = L^2 \tag{1.10}$$

which exactly corresponds to the prediction from a rodlike chain. Hence, the chain configuration of a single WLC is determined by a chain flexibility parameter L/a only, whose variation controls the statistical properties of a polymer ranging from a flexible chain to a rodlike chain. In the crossover regime $L/a \sim 2-3$, interestingly, the WLC model undergoes a first-order transition between rodlike configurations and flexible configurations [108, 81]. In addition, it is worth noting that the WLC model is an elegant model to describe the helix formation of double-stranded DNA

[121] so it also has a biological significance.

1.3 Modified diffusion equation for WLC-based SCFT

The orientational correlation between segments along the chain backbone is a major concern in the WLC model; the advantage of the WLC-based SCFT is its ability to predict and extract useful information about the structure and thermodynamic properties of orientation-dependent polymeric fluids, such as liquid crystalline polymers. In these systems, the orientational properties of constituent molecules are strongly coupled with the spatial variation. However, in order to capture the additional orientation-dependent information, WLC-based SCFT takes more computational cost than the GSC-based model.

In the framework of SCFT, there is an important physical quantity called the propagator, used to calculate many thermodynamic variables, such as molecular density, pressure, chemical potential, free energy. Specifically, in a continuous WLC-based SCFT, the propagator $q(\mathbf{r}, \mathbf{u}, s)$ describes the probability density that the end of a polymer chain with contour length sL is at position $\mathbf{r}$ and the tangent vector of the end segment is $\mathbf{u}$. It satisfies an elegant partial differential equation well-known as the modified diffusion equation (MDE) [41]

$$\frac{\partial}{\partial s} q(\mathbf{r}, \mathbf{u}, s) = \left[\frac{L}{a} \nabla_{\mathbf{u}}^2 - L\mathbf{u} \cdot \nabla_{\mathbf{r}} - w(\mathbf{r}, \mathbf{u}) \right] q(\mathbf{r}, \mathbf{u}, s) \tag{1.11}$$

which is subject to an initial condition $q(\mathbf{r}, \mathbf{u}, 0) = 1$. Eq. 1.11 can be directly derived from the Eq. 1.5 associated with an auxiliary external field $w(\mathbf{r}, \mathbf{u})$, in terms of the path integral of a functional [41] or a Chapman-Kolmogorov equation of the conditional transition probability [70]. The first operator on the right hand of Eq. (1.11) $\nabla_{\mathbf{u}}^2$ is a standard Laplacian on a unit sphere, associated to an adjustable coefficient relevant with the chain rigidity L/a. In the rod limit $L/a \ll 1$, after dropping the term $(L/a)\nabla_{\mathbf{u}}^2$, Eq. (1.11) exactly recovers the rigid-rod model; the detailed derivation was well-established in our recent publication, shown in

Appendix A. The second term describes the coupling effect between the orientational and positional factors. In the flexible limit $L/a \gg 1$, expanding $q(\mathbf{r}, \mathbf{u}, s)$ in spherical harmonics $Y_l^m(\mathbf{u})$ and then truncating the term proportional to $(L/a)^{-l/2}$ beyond the index $l = 2$, we can verify in Appendix C that Eq. (1.11) can exactly recover to the MDE usually used for the GSC model. This is demonstrated in the full 3D space for the first time by us (in Chapter 3), though similar proofs existed previously in 1D space.

1.4 Numerical approaches

In general, the full solution to Eq. (1.11) depends on numerical computations. The first difficulty we encounter is that Eq. (1.11) has six variables in full space, including 3 for $\mathbf{r}(x, y, z)$, 2 for $\mathbf{u}(\theta, \varphi)$ and 1 for s. The second one is that the coupling operator $\mathbf{u} \cdot \nabla_{\mathbf{r}}$ increases the complexity of numerical treatments in the orientation- and positional-dependent propagator [39]. Actually, the developments of proper numerical algorithms for the applications of WLC-based SCFT have struggled all along. Until recently, most work solved Eq. (1.11) by a reduction of the dimensionality benefiting from the assumed symmetry on specific systems. A complete exploration to the WLC system in full space will be developed in this thesis in Chapter 3. In the following, I will briefly review some progress of numerical schemes for MDE.

Computationally, the spatial and orientational variables in the WLC probability function need to be simultaneously represented in numerical approaches. Recent algorithms are summarized in Tables 1.1 and can roughly be classified into the following categories. (1) Both orientational and spatial dependencies are treated by finite-difference schemes [107, 27, 46]. In numerical results, to achieve the same precision as those from (2) and (3) below, an extremely high computational resource is required. The direct discretization is a poor candidate for high dimensional computation. (2) The orientational dependence is treated by an expansion in terms of the spherical harmonics and the spatial dependence by a finite difference scheme [24, 25, 45]. In Chapter 2, we utilize a similar scheme, in which the positional and timelike variables are treated by the unconditionally stable Crank-

Nicolson algorithm and the orientational variables are treated by a software package, SPHEREPACK, which provides a fast and efficient spherical-harmonic analysis and synthesis transformations [1]. For a sharp boundary condition and interface, this method works successfully only with a high resolution on the spatial variable, resulting in high computational demand too. The intermediate and strong segregation regimes of the phase-separated problem corresponds to a relatively sharp interface, especially in complex morphologies [70]. (3) Both orientational and spatial dependencies are treated by combinatorial orthonormal eigenfunctions [76]. The number of eigenfunctions containing the spatial variables can be significantly lowered than the number of divisions in the spatial-variable space, hence this method is much less computationally demanding than the two methods above. The drawback of the full spectral scheme is that it needs to spend a huge cost on inversion of an asymmetric matrix with computational operations proportional to $\sim (KM)^3$ at every propagating step s. Here K and M represents the numbers of Fourier basis and spherical harmonics used, respectively. (4) The orientational and spatial dependence are treated by the expansions in terms of the spherical harmonics plane wave basis, respectively. One scheme commonly treating with the diffusion-like equation is the split-step algorithm [36, 37]. The corresponding version for WLC-based SCFT previously proposed by Fredrickson [39] will be presented in Chapter 3. This approach approximately has $O(NKM^{3/2}\log_2 M)$ computational operation. Here, N is the number of the contour steps for variable s. At the same time, in Chapter 3, we have also developed a new numerical strategy incorporating the spherical harmonics expansion and plane-wave spectral collocation method with a multi-step backward differentiation formula (BDF). Computationally, this algorithm achieves an estimated $O(NKM)$ computational operation, which speeds up the computation by orders of magnitude in computation time, in comparison with a split-step algorithm [39] mentioned above. With this powerful numerical tool in hand, we are capable of broadening our study to more complicated micro-structures in two- and three-dimensional space, especially for the network-like structures Q^{230} (see chapter 3). The fact that BDF has a truncation error of (Δs^4) allows us to use larger step size in s. This can be contrasted with the fact that the truncation error is of the order (Δs^3) in the split-step algorithm.

Table 1.1: Numerical approaches in solving MDE for wormlike polymer models.

System	Variables	Numerical approaches	References (Year)
Nematic state for any L/a	s, θ	Direct discretization in θ; Crank-Nicolson method for the s-dependence.	Chen [16] (1993)
Isotropic-Nematic interface for $L/a \gg 1$	θ, φ, z	Spherical harmonics expansion in θ, φ; Finite difference scheme for the z-dependence.	Cui *et al* [24] (1995)
Lamella structure of AB diblock copolymers at $f = 1/2$ for any L/a	s, θ, z	Legendre expansion for the θ-dependence and Fourier expansion for the z-dependence; Analytical treatment on the s-dependence.	Matsen [76] (1996)
Smectic structure of rod-coil polymers	s, θ, φ, z	Spherical harmonics expansion for the θ, φ-dependence; Finite difference scheme for the z-dependence; Forward Euler method for the s-dependence.	Düchs and Sullivan [25] (2002)
A general suggestion	s, θ, φ, x, y, z	SPHEREPACK application for both θ- and φ-dependencies; Fourier expansion for all x, y, z-dependencies; Split-step algorithm for the s-dependence.	Fredrickson [39] (2006)

... ... to be continued

Continuing from table 1.1

System	Variables	Numerical approaches	References (Year)
Depletion of semiflexible polymers near a spherical particle	s, θ, r	Legendre expansion for θ; Finite difference for radial variable r in spherical coordinate; Forward Euler method for the s-dependence.	Ganesan *et al* [45] (2008)
Smectic structure of rod-coil polymers	s, θ, φ, z	Finite difference scheme for z-dependence; Discretizing the θ and φ on a triangulated surface of a unit sphere; Forward Euler method for the s-dependence.	Song *et al* [107] (2009)
Homopolymer brush for any L/a	s, θ, z	Finite difference scheme in both θ and z dependence; Crank-Nicolson method for the s-dependence.	Deng *et al* [27] (2010)
Isotropic-Nematic interface for any L/a	s, θ, φ, z	SPHEREPACK application for both θ- and φ-dependencies; Finite difference scheme for the z-dependence; Crank-Nicolson method for the s-dependence.	Jiang and Chen [61] (2010)
Lamella structure of AB diblock copolymer for any f and L/a	s, θ, z	Legendre/plane wave basis expansion in θ/z; Split-step algorithm for s-dependence.	Jiang, Zhang and Chen [63] (2011)

... ... to be continued

Continuing from table 1.1

System	Variables	Numerical approaches	References (Year)
Smectic structure of semiflexible-coil diblock copolymers	s, θ, φ, z	Fourier basis expansion in z; Discretizing the θ and φ on a triangulated surface of a unit sphere; Forward Euler method for the s-dependence.	Song *et al* [106] (2011)
Smectic structure of semiflexible block copolymers	s, θ, φ, x, y	Finite difference scheme for z-dependence; Discretizing the θ and φ on a triangulated surface of a unit sphere; Forward Euler method for the s-dependence; GPU (graphics processing units) technique is utilized.	Gao *et al* [46] (2011)
Three dimensional structures in AB diblock copolymers	s, θ, φ, x, y, z	Spherical harmonics expansion for the θ, φ-dependence; Fourier expansion in x, y, z; BDF for the s-dependence.	this work in Chapter 3

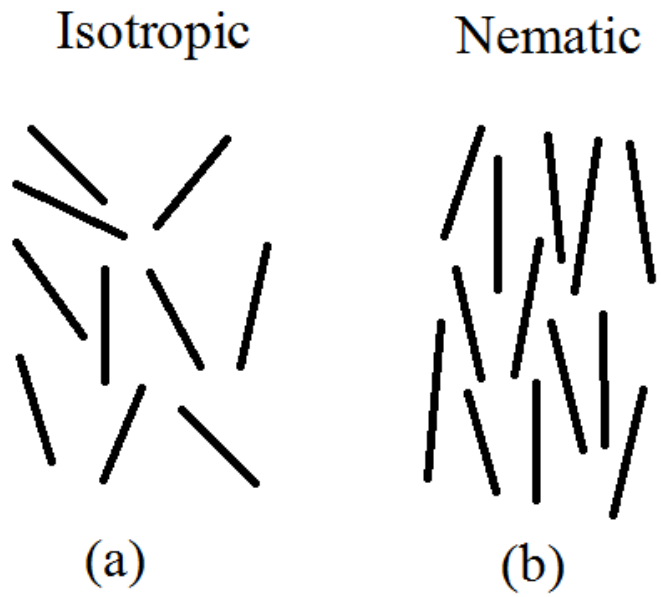

Figure 1.6: (a) Isotropic and (b) Nematic phases for rod-like particles.

1.5 Physical backgrounds

1.5.1 Isotropic-nematic transition

The orientational distribution of anisotropic molecules shows an isotropic phase in low density. Increasing the density of molecules beyond a critical value, the system displays an orientational order and shows a nematic phase, due to the anisotropic interactions stemming from excluded-volume effects between molecules. This is the so called isotropic-nematic (I-N) transition as shown in Fig. 1.6.

The anisotropic interaction has been well testified to play an important role in the formation of orientation-dependent systems. Specifically, it is straightforward to take the anisotropic interaction as a part of Hamiltonian in the WLC model in the framework of SCFT. Before formulating the orientational interaction potential which results in nematic orders, it is necessary to define a segment density operator

related to its position and orientation to a WLC system containing n polymer chains

$$\hat{\rho}(\mathbf{r},\mathbf{u}) = \frac{L}{a}\sum_{i=1}^{n}\int_0^1 \mathrm{d}s\Big[\mathbf{r}-\mathbf{R}_i(s)\Big]\Big[\mathbf{u}-\mathbf{u}_i(s)\Big] \tag{1.12}$$

Then, the potential energy from the non-bonded interaction among segments is approximated to be a "two-body" interaction as a quadratic form in $\hat{\rho}(\mathbf{r},\mathbf{u})$

$$U = \frac{1}{2}\int \mathrm{d}\mathbf{r}\int \mathrm{d}\mathbf{r}'\int \mathrm{d}\mathbf{u}\int \mathrm{d}\mathbf{u}'\hat{\rho}(\mathbf{r},\mathbf{u})w(\mathbf{r},\mathbf{r}',\mathbf{u},\mathbf{u}')\hat{\rho}(\mathbf{r}',\mathbf{u}') \tag{1.13}$$

where the coefficient $1/2$ compensates for the double counting for the same pair-wise interactions. The kernel function $w(\mathbf{r},\mathbf{r}',\mathbf{u},\mathbf{u}')$ is a generalized pair potential function describing the excluded volume between two anisotropic segments with the centers of mass at position $\mathbf{r}$ and $\mathbf{r}'$ and the orientations denoted by two unit vectors $\mathbf{u}$ and $\mathbf{u}'$, respectively. In order to deal with Eq.(1.13) easier, further, the function w is usually assumed to have a local form for positional variables, i.e.

$$w(\mathbf{r},\mathbf{r}',\mathbf{u},\mathbf{u}') \approx \delta(\mathbf{r}-\mathbf{r}')v(\mathbf{u},\mathbf{u}') \tag{1.14}$$

where $v(\mathbf{u},\mathbf{u}')$ is a local orientation-dependent interaction. Theoretically, there are two types of phenomenological approaches to deal with such a steric interaction.

Onsager interaction: Consider two spherocylinders labelled by 1 and 2, both having the exactly same length l and diameter d. The excluded volume occupied by these two spherocylinders can be expressed by [90]

$$v(\mathbf{u},\mathbf{u}') = 2l^2d|\mathbf{u}_1\times\mathbf{u}_2| + O(d^2) \tag{1.15}$$

where the last term at the right hand can be dropped for a slender rod limit i.e. $l \gg d$. The polymer segment is described as a cylindrical filament which reflects the nature of a self-avoiding chain between different chain segments. In a lyotropic case, the orientational dependence of the excluded-volume interaction is responsible for driving the system to form a nematic phase in relatively high densities, as originally discussed by Onsager [90] for rigid rods, and later generalized to wormlike polymers by Khokhlov, Semenov [65] and Grosberg [48].

Maier-Saupe interaction: Consider rod-like molecules interacting via van der Waals interactions. We assume that a particular molecule feels the orientation-dependent interaction arising from its surrounding molecules. It leads to the interaction potential for each molecule

$$v(\mathbf{u},\mathbf{u}') = -\frac{1}{2}C_{MS}S_{\alpha\beta}\bigg(3u_\alpha u_\beta - \delta_{\alpha\beta}\bigg) \qquad (\alpha,\beta = x,y,z) \tag{1.16}$$

where the positive coefficient C_{MS} is proportional to $1/T$ (temperature) and the order parameter $S_{\alpha\beta}$ describes the average distribution of orientations of each molecule. Note, Einstein summation notation is used in Eq. (1.16). Herein, a polymer segment is considered to stand in an averaged orientational field formed by its surrounding ones. The orientational alignment of molecules is driven by an attractive interaction whose magnitude is controlled by a parameter associated with temperature. The Maier-Saupe interaction [75] is commonly regarded as a fundamental theory of thermotropic liquid crystals on a mean-field level.

The order tensor $S_{\alpha\beta}(\mathbf{r})$ is a suitable order parameter describing the orientation of the director in a nematic mesophase, defined as

$$S_{\alpha\beta}(\mathbf{r}) = \frac{1}{2}\int \mathrm{d}\mathbf{u}\phi(\mathbf{r},\mathbf{u})(3u_\alpha u_\beta - \delta_{\alpha\beta}) \tag{1.17}$$

where $\phi(\mathbf{r},\mathbf{u})$ is the normalized probability distribution of molecules at position $\mathbf{r}$ with orientation $\mathbf{u}$. $S_{\alpha\beta}$ is a symmetric and traceless 3×3 matrix and can be diagonalized in a Cartesian coordinate system. The resulted eigenvalues are sorted in the descending order S, $(P-S)/2$ and $-(P+S)/2$. The eigenvector corresponding to the largest eigenvalue S represents the *director* for a nematic phase. P is a biaxiality of the molecular distribution, describing the degree of biaxial effect of a nematic phase. For a uniaxial nematic phase, $P = 0$.

Onsager [90] firstly predicted such a first-order I-N transition for a system consisting of rodlike molecules by taking the hard-rod excluded volume effects into account. Later Lekkerkerker *el al* [72] extended the study to a system of rodlike particles with different lengths. On the other hand, even for the flexible polymer chains, the existence of the I-N transition was also suggested [65, 86, 118] at a higher density compared to rodlike particles. Using the WLC model based SCFT, Chen

[16] checked the influence of continuous variation of chain rigidity L/a ranging from the rigid rod limit to the flexible limit on the properties of coexisting isotropic and nematic phases. Furthermore, Chen *et al* studied the interface between the isotropic and nematic phases separately in the limits $L/a \ll 1$ [18, 17] and $L/a \gg 1$ [24] and found that particles prefer to align parallel to the interface independent of chain rigidity, by analysing the surface tension as a function of angle between the director of nematic phase and the normal direction of the interface. But the influence of intermediate chain rigidity on the physical properties of the I-N coexisting interface was not studied in their work. In Chapter 2, implementing the Onsager-type interaction, I will study the thermodynamic properties of the isotropic-nematic interface with a wide range of chain rigidity by virtue of WLC-based SCFT.

1.5.2 Microphase separations for AB diblock copolymers

AB diblock copolymers, which are composed of two chemically different subchains connected by covalent bonds, are a fascinating category of soft materials with unique structural and mechanical properties [52]. In the past three decades, tremendous experimental and theoretical research efforts have been dedicated to the study of nano-scale ordered structures self-assembled from AB diblock copolymers, as shown in Fig. 1.2. These complicated mesostructures result from the phase separation which is determined by the competitive balance between the interaction energy and the chain stretching. The repulsive interaction between different chemically blocks drives the system to phase separate, *i.e.* form A-rich and B-rich regions, whereas the connectivity of copolymer chains only leads to the microphase separation instead of macrophase separation (*e.g.* oil-water separation). The immiscibility between components A and B is commonly described by a reduced combinatorial parameter χN, in which χ is the Flory-Huggins interaction parameter characterizing the A-B interaction and N is the polymerization of a copolymer chain. On basis of the GSC assumption for the chain configuration, Leibler predicted the critical microphase separation transition point for diblock copolymers at $\chi N = 10.495$ [71] by virtue of the random phase approximation (RPA) in the spirit of a phenomenological Landau methodology. In addition to the lamellar phase, he also verified the existence of complicated ordered phases, such as hexagonally ordered cylinders, and body-

centered-cubic spheres, depending on another parameter f, the volume fraction of component A. Thereafter, the entire phase diagrams of diblock copolymers were obtained by numerical solution to GSC-based SCFT [79, 20] in the coordinates of χN and f.

An extra chain rigidity parameter L/a is introduced into WLC-based SCFT and enriches the ordered mesostructures previously obtained by GSC-based SCFT. However, the corresponding exploration based on the WLC model was only constrained for lamellar phases due to the increased computational cost. Matsen studied the disorder-lamellar (DL) phase transition for the symmetric AB diblock copolymer using a WLC based SCFT [76]. In comparison with flexible chains, he found the increase of chain rigidity will highly decrease the Flory-Huggins parameter required for phase separation between A and B. Furthermore, Netz and Schick [83] considered the Maier-Saupe anisotropic interaction and extended the exploration of symmetric AB diblock copolymers into smectic phases. Recently, Düchs and Sullivan [25] studied the phase behavior of rod-coil diblock copolymers by considering the Onsager type interaction. Shortly thereafter, Song *et al* [107] extended the theoretical calculations to morphologies without the rotational symmetry imposed, i.e. azimuthal effects involved. Taking the Maier-Saupe interaction into account, Shah and Ganesan [103] present a theoretical study evaluating the bridging/looping fractions in a model of coil-semiflexible multiblock copolymers. Unfortunately, all works mentioned above constrained their calculations only in one spatial dimension, so that more fascinating mesophases in higher dimension were unexplored. In Chapter 3, an efficient and accurate numerical scheme is proposed to attack this problem.

1.6 Present work and organization of the thesis

In this thesis, I focus on the development of efficient numerical algorithms in the framework of WLC-based SCFT for two specific systems:

In Chapter 2, the effects of the flexibility of constituent WLCs on the interfacial properties between isotropic and nematic phases are investigated in a SCFT

approximation [61]. The model is built from a WLC formalism which crosses over from the rod limit to the flexible limit, and the Onsager-type interaction which describes the orientational-dependent repulsive interaction. Physical properties such as the surface tension, interfacial width and density- and order-parameter profiles were numerically calculated as functions of flexibility (defined as the ratio between the total polymer length and the persistence length) and tilt angle (defined as the angle between the interfacial normal and the nematic director in the nematic phase). The resulting MDE was numerically solved by using a combination of the Crank-Nicolson algorithm and SPHEREPACK, a software package that deals with the analysis and synthesis of spherical-harmonics functions.

In Chapter 3, we study the disorder-order transition boundary of wormlile AB diblock copolymers on the basis of the WLC formalism aided by a SCFT treatment [63, 62]. We examine the influence of the persistency on the phase diagram and properties of the phase transition as a function of the volume fraction, Flory-Huggins parameter and relative chain rigidity, covering a broad regime spanning from the Gaussian chain to rigid rodlike chain. On one hand, we demonstrate that the results from a Gaussian-weight based theory can be recovered in the long-chain limit, and on the other hand, we display that significant revisions to the phase diagram, due to the persistency effects, exist for shorter chains. A split-step numerical algorithm and a multistep implicit-explicit BDF scheme are designed for the computational task.

In Chapter 4, a summary of this thesis and outlook for new research directions is presented.

It is worth noting that some of published work completed during my PhD period are not covered in this thesis on account of consistency, including the wormlike polymer brush problem [27], the adsorption of wormlike polymers on a planar surface [28] and rigid polymers confined on the surface of a sphere [123, 124].

Chapter 2

Isotropic-Nematic Interface in a Lyotropic System of Wormlike Chains with the Onsager Interaction

2.1 Introduction

The spacial variation of an isotropic-nematic interface is closely coupled with the orientational properties of constituent molecules, microscopically; in comparison with the interface produced in a small-molecule system where the orientational degrees of freedom of a molecule can be ignored, an isotropic-nematic interface also macroscopically depends on the angle that the interfacial normal makes with respect to the nematic director far away on the liquid-crystal side. Models of the isotropic-nematic interface in liquid crystals consisting of semiflexible, interacting polymer chains have been actively studied by theoretical work [80, 18, 24, 2, 104, 33, 67, 32, 17, 50, 59] in recent years, and related experimental work in colloids [14, 15], tactoidal droplets [117, 85] and viruses [29, 30] have been reported as well.

The flexibility of a wormlike polymer chain can be described by the ratio between the total chain length L and the persistence length λ. Past theoretical studies of

a polymeric liquid-crystal interface mostly focused on the limit of a rigid, rodlike system ($L \ll \lambda$) where the rod length L is a characteristic length scale [80, 104, 18, 115, 32, 17], or the limit of a flexible system ($L \gg \lambda$) where the persistence length λ plays a dominating role [24, 50]; in these two limits, theoretical treatments can be somewhat simplified. Experimental measurements can be done in systems where the chain length may change but the persistence length is kept fixed [15]. The effects of semi-flexibility on a polymeric liquid-crystal interface remain theoretically unexplored.

A theoretically well-defined model for a liquid crystal consisting of lyotropic wormlike polymer chains can be traced back to the classical work of Onsager [90]. In such a system, a polymer chain can be modelled by a cylindrical filament (a microscopic version of a garden hose) where the diameter d characterized the self-avoiding nature between different polymer segments. In a lyotropic case, the orientational dependence of the excluded-volume interaction is responsible for driving the system to form a nematic phase in relatively high densities, as originally discussed by Onsager [90] for rigid rods, and latter generalized to wormlike polymers by Khokhlov, Semenov [65] and Grosberg [48]. The bulk properties, for example, dependencies of the transition densities, orientational order parameter, and free-energy related properties such as the chemical potential and osmotic pressure on the flexibilty L/λ, are now known through an exact numerical solution to the differential equation yielded from this model [16].

This work examines the influence of the flexibility on the isotropic-nematic interface of a lyotropic polymer system that incorporates the Onsager interaction, for any ratios of L/λ. The only two ingredients in the model are: a statistical description for the wormlike polymer where the ratio L/λ is introduced and the Onsager interaction which drives the isotropic-nematic transition. This interfacial study fills the gap between the limit of $L \ll \lambda$ [80, 104, 17] and the limit of $L \gg \lambda$ previously examined [50, 24]. This interfacial study is also an extension to the earlier work on the determination of the isotropic-nematic transition, where the bulk properties were calculated [16]. The results in the current study can be compared with experimental systems where the isotropic-nematic interface is inherently flat, or having a curved interface where the curvature is much less than

the inverse interface width, to be examined below.

The method used in this study is similar in spirit to the treatment proposed by Cui *et al* [24]; the main difference is that our algorithm utilizes a software package, SPHEREPACK, which provides a fast and efficient spherical-harmonic analysis and synthesis transformations [1] to deal with the orientational dependence; the positional and path variables are treated by the unconditionally stable Crank-Nicolson algorithm. This treatment can be generalized to systems without the type of periodical boundary conditions proposed by Matsen [76]; the method also has the advantage of letting the software package to deal with the mathematical complexities in handling the spherical expansion which no longer requires manual calculations [24, 25].

This study is organized as follows. In Section 2.2, we introduce the theoretical framework that the current calculation is based on for an arbitrary flexibility. The discussion and proof that this model exactly yields the rod formalism and flexible-chain formalism in the corresponding limits are given in Appendices A and B, respectively. We also discuss the numerical algorithm in detail within this section. In Section 2.3, the main numerical results are given and discussed.

2.2 General formalism

In this section, we introduce the general formalism yielded from the self-consistent field theory (SCFT) for a wormlike chain problem that is used for the calculations in this work. We consider a system of volume V consisting of n wormlike homopolymers. Each polymer chain is a cylindrical filament and has a total contour length L and a diameter of d. We assume that the configuration of a chain is described by the Saito-Takahashi-Yunoki model [100], which is a continuous version of the Kratky-Porod model [68]. Mathematically the configuration of a chain is described by a continuous space curve $\mathbf{R}(s)$, where $s \in [0, 1]$ is the arc variable along the polymer backbone. The vector $\mathbf{u}(s) \equiv (1/L)\mathrm{d}\mathbf{R}(s)/\mathrm{d}s$ specifies the tangent direction at s and is restricted to be a unit vector in our treatment, i.e. $|\mathbf{u}(s)| = 1$.

We are interested in the calculation of the free energy, which is related to the partition function of the system,

$$Z = \frac{1}{n!} \int \prod_{k=1}^{n} \mathcal{D}\left[\mathbf{R}_k\right] \exp\left(-\mathcal{H}\right), \tag{2.1}$$

where the Hamiltonian $\mathcal{H}$ consists of two parts: $\mathcal{H} = \mathcal{H}_1 + \mathcal{H}_2$. The first part is the bending energy of wormlike chains,

$$\mathcal{H}_1 = \frac{\lambda}{2L} \sum_{k=1}^{n} \int_0^1 \mathrm{d}s \left| \frac{\mathrm{d}\mathbf{u}_k\left(s\right)}{\mathrm{d}s} \right|^2. \tag{2.2}$$

The microscopic parameter, bare *persistence length* λ, describes the distance along the contour of a wormlike chain over which the orientational correlation exponentially decays. The other part is the Onsager-type excluded-volume interaction potential [90, 65],

$$\mathcal{H}_2 = a^2 d \int \mathrm{d}\mathbf{r}\, \mathrm{d}\mathbf{u}\, \mathrm{d}\mathbf{u}' \hat{\rho}(\mathbf{r}, \mathbf{u}') |\mathbf{u} \times \mathbf{u}'| \hat{\rho}(\mathbf{r}, \mathbf{u}), \tag{2.3}$$

where a represents the Kuhn length and is related to λ by [100]

$$a = 2\lambda, \tag{2.4}$$

in the limit of $L \gg \lambda$ of a $d = 0$ polymer in free space (i.e. $\mathcal{H}_2 = 0$). We can introduce a segment density operator

$$\hat{\rho}(\mathbf{r}, \mathbf{u}) = \frac{L}{a} \sum_{k=1}^{n} \int_0^1 \mathrm{d}s \delta \left[\mathbf{r} - \mathbf{R}_k(s)\right] \delta \left[\mathbf{u} - \mathbf{u}_k(s)\right], \tag{2.5}$$

which is a function of both $\mathbf{r}$ and $\mathbf{u}$ [39].

Following the SCFT treatment, where a self-consistent field $w(\mathbf{r}, \mathbf{u})$ is introduced [39] in conjugation to the operator $\hat{\rho}$, we can write the Helmholtz free energy per chain as

$$\frac{F}{k_B T} = \ln\left(\frac{C}{Q}\right) + \frac{1}{V} \int \mathrm{d}\mathbf{r}\, \mathrm{d}\mathbf{u} \left[C \int \mathrm{d}\mathbf{u}' \phi(\mathbf{r}, \mathbf{u}) |\mathbf{u} \times \mathbf{u}'| \phi(\mathbf{r}, \mathbf{u}') - w(\mathbf{r}, \mathbf{u}) \phi(\mathbf{r}, \mathbf{u}) \right], \tag{2.6}$$

where a constant shift, $\ln(L^2 d/V)$, in the free energy has been used and

$$C \equiv \frac{n L^2 d}{V} \tag{2.7}$$

is the overall reduced chain density in the system. We have kept the same reduction prefactor $L^2 d$ and the symbol C for the chain density following Onsager's original work [90]. The density distribution function $\phi(\mathbf{r}, \mathbf{u})$ is the statistical average of $\hat{\rho}/\rho_0$ and represents the density of segments of length a, satisfying the normalization condition

$$\int \mathrm{d}\mathbf{r}\, \mathrm{d}\mathbf{u} \phi(\mathbf{r}, \mathbf{u}) = V. \tag{2.8}$$

The partition function of a single chain can be calculated from $Q = (1/4\pi V) \int \mathrm{d}\mathbf{r} \int \mathrm{d}\mathbf{u} q(\mathbf{r}, \mathbf{u}, 1)$, where the propagator $q(\mathbf{r}, \mathbf{u}, s)$ follows the modified diffusion equation (MDE),

$$\frac{\partial}{\partial s} q(\mathbf{r}, \mathbf{u}, s) = \left[\frac{L}{a} \nabla_{\mathbf{u}}^2 - L\mathbf{u} \cdot \nabla_{\mathbf{r}} - w(\mathbf{r}, \mathbf{u}) \right] q(\mathbf{r}, \mathbf{u}, s), \tag{2.9}$$

with the initial condition $q(\mathbf{r}, \mathbf{u}, 0) = 1$ [39]. Eqs. 2.6-2.9 were recently considered for the calculation of the structure of a wormlike brush problem by us and co-workers [27]. The parameter

$$\alpha \equiv L/a \tag{2.10}$$

describes the flexibility of a wormlike chain. In the rod-like chain limit $\alpha = 0$ and in the flexible chain limit $\alpha \gg 1$. The current work focuses on how the isotropic-nematic interface is influenced by the flexibility parameter α over the entire range. Minimizing the free energy, Eq. 2.6, with respect to the external filed $w(\mathbf{r}, \mathbf{u})$ and density $\phi(\mathbf{r}, \mathbf{u})$, we obtain equations based on the saddle-point approximation,

$$\phi(\mathbf{r}, \mathbf{u}) = \frac{1}{4\pi Q} \int_0^1 \mathrm{d}s q(\mathbf{r}, \mathbf{u}, s) q(\mathbf{r}, -\mathbf{u}, 1-s), \tag{2.11}$$

$$w(\mathbf{r}, \mathbf{u}) = \Lambda + 2C \int \mathrm{d}\mathbf{u}' |\mathbf{u} \times \mathbf{u}'| \phi(\mathbf{r}, \mathbf{u}'), \tag{2.12}$$

where Λ is a constant which will be defined later. Eqs. 2.9, 2.11 and 2.12 form a self-consistent set of equations that are numerically solved in the next few sections.

2.2.1 Bulk phases and the isotropic-nematic phase transition

In a spatially homogeneous system, i.e. in a bulk phase, we recover the formalism and results studied earlier by one of us [16]. Dropping the $\mathbf{r}$ dependence and adding a subscript "b" to the physical quantities considered above, we write the Helmholtz free energy per chain in a simplified form,

$$\frac{F}{k_BT} = \ln\left(\frac{C}{Q_\mathrm{b}}\right) + \int \mathrm{d}\mathbf{u}\left[C\int \mathrm{d}\mathbf{u}'\phi_\mathrm{b}(\mathbf{u})|\mathbf{u}\times\mathbf{u}'|\phi_\mathrm{b}(\mathbf{u}') - w_\mathrm{b}(\mathbf{u})\phi_\mathrm{b}(\mathbf{u})\right], \quad (2.13)$$

where the partition function of a single chain can be calculated from $Q_\mathrm{b} = 1/(4\pi)\int \mathrm{d}\mathbf{u}q_b(\mathbf{u}, s=1)$. The free energy Eq. 2.13, together with the MDE [Eq. 2.9 without the $\mathbf{u}\cdot\nabla_\mathbf{r}$ term], was considered earlier [16], where the isotropic-nematic transition for any chain flexibility α was determined. We verify this result in this section.

In our lyotropic system, at a given flexibility parameter α, the only parameter that controls the physical properties of the system is the reduced density C. At the first-order isotropic-nematic phase transition, the chemical potentials calculated from the isotropic density C_i and the nematic density C_n are equal, $\mu(C_\mathrm{i}) = \mu(C_\mathrm{n})$; the osmotic pressures are equal as well, $P(C_\mathrm{i}) = P(C_\mathrm{n})$. Both the chemical potential and osmotic pressure can be calculated from the free energy in the above, by $\mu \equiv [\partial(nF)/\partial n]_{T,V}$ and $P \equiv -[\partial(nF)/\partial V]_{T,n}$ once the reduced density is specified [65, 86, 16, 72]. The two phase-balancing equations are nonlinear in C_i and C_n; we use the Newton-Raphson algorithm [93] to solve this set of nonlinear equations to determine C_i and C_n.

The calculation of the free energy requires an accurate computational algorithm to solve the MDE. In a bulk phase, Eq. 2.9 is reduced to,

$$\frac{\partial}{\partial s}q_\mathrm{b}(\mathbf{u}, s) = \left[\alpha\nabla^2_\mathbf{u} - w_\mathrm{b}(\mathbf{u})\right] q_\mathrm{b}(\mathbf{u}, s), \quad (2.14)$$

with the initial condition $q_\mathrm{b}(\mathbf{u}, 0) = 1$. Chantawansri *et al* introduced a software package, SPHEREPACK, to successfully deal with the two-dimensional Laplacian operator $\nabla^2_\mathbf{u}$ on the surface of a unit sphere in the study of diblock copolymer self-assembly on a sphere with chain statistics described by the Gaussian model [8].

SPHEREPACK promises to provide an efficient spherical harmonic analysis and synthesis transformation [110] and was developed by Adams and Swarztrauber of the National Center for Atomospheric Research [1]. Subroutines written in FORTRAN 77 are available for implementing the fast fourier transform (FFT) on the azimuthal angle $\varphi \in [0, 2\pi)$ and either equally-spaced or Gauss-distributed grid points on the polar angle $\theta \in [0, \pi]$ [111]. The subroutines treat function transformations in real numbers, which save half the computation time compared to those using complex numbers on scalar spherical harmonic functions [47]. We have implemented SPHEREPACK in our treatment of the operator $\nabla^2_{\mathbf{u}}$.

Our treatment of the $\partial/\partial s$ operator followed the unconditionally stable Crank-Nicolson algorithm [93]. Introducing a contour step $\Delta\bar{s}$ for $\bar{s}$, we solved Eq. 2.14 in the form of

$$\left[1 - \frac{\alpha\Delta s}{2}\nabla^2_{\mathbf{u}}\right] q_b(\mathbf{u}, s + \Delta s) = \frac{1 - (\Delta s/2)w_b(\mathbf{u})}{1 + (\Delta s/2)w_b(\mathbf{u})} \left[1 + \frac{\alpha\Delta s}{2}\nabla^2_{\mathbf{u}}\right] q_b(\mathbf{u}, s). \quad (2.15)$$

The entire numerical procedure proceeds as follows, starting with a known $q_b(\mathbf{u}, s)$ at step s. We utilized the analysis and synthesis transformation of SPHEREPACK [1] to calculate $\nabla^2_{\mathbf{u}} q_b(\mathbf{u}, s)$. As the next step we used the analysis transform again on the right side of Eq. 2.15, defined as a new function $f(\mathbf{u}, s)$; we then consider

$$f(\mathbf{u}, s) = \sum_{l=0}^{\bar{L}} \sum_{m=0}^{l} P_l^m(\cos\theta) \left[a_{l,m}(s)\cos(m\varphi) + b_{l,m}(s)\sin(m\varphi)\right] \quad (2.16)$$

where $P_l^m(\cos\theta)$ is the associated Legendre polynomial and the integer $\bar{L}$ controls the precision of the transform. Finally, we set

$$c_{l,m}(s + \Delta s) = a_{l,m}(s) \left[1 + \frac{\alpha\Delta s}{2} l(l+1)\right]^{-1}, \quad (2.17)$$

$$d_{l,m}(s + \Delta s) = b_{l,m}(s) \left[1 + \frac{\alpha\Delta s}{2} l(l+1)\right]^{-1}, \quad (2.18)$$

to calculate

$$q_b(\mathbf{u}, s + \Delta s) = \sum_{l=0}^{\bar{L}} \sum_{m=0}^{l} P_l^m(\cos\theta) \left[c_{l,m}(s + \Delta s)\cos(m\varphi) + d_{l,m}(s + \Delta s)\sin(m\varphi)\right], \quad (2.19)$$

with the assistance of the orthonormality conditions to the spherical harmonics.

In our current numerical calculation, we used evenly spaced grid points in both $\theta \in [0, \pi]$ and $\varphi \in [0, 2\pi)$, broken into N_θ and N_φ slabs, respectively. In a bulk phase, for the nematic phase, the function $q_b(\mathbf{u}, s)$ has no φ dependence due to axial symmetry about the nematic director. The φ dependence in the above algorithm was used for testing the precision of the numerical results in the inhomogeneous case presented below, where the φ dependence becomes important. Taking $\Delta s = 0.0002$, $N_\theta = 36, N_\varphi = 72$ (and in another comparative study, $N_\theta = 72, N_\varphi = 144$), we have calculated the physical properties at the isotropic-nematic phase transition, including the segment density $C_{\rm i}(\alpha)$, the nematic segment density of $C_{\rm n}(\alpha)$ and the nematic order parameter $S_2 \equiv \langle P_2(\cos\theta)\rangle$, which are shown as functions of the flexibility parameter α in Fig. 2.1. Our results of $C_{\rm i}(\alpha = 0) = 4.1963$, $C_{\rm n}(\alpha = 0) = 5.3343$ and $S_2(\alpha = 0) = 0.7902$ fully agree with the results from a number of previous studies [72, 16, 86]. In the large α limit of Fig. 2.1 (A) and (B), we have also added dashed lines representing $C_{\rm i}(\alpha \gg 1) = 13.05\alpha$ and $C_{\rm n}(\alpha \gg 1) = 14.08\alpha$, which agree well with previous results [16, 118]. In the intermediate region of α, our numerical data fully agree with those in Ref. [16] , in which a finite-difference scheme is used to solve Eq. 2.14, rather than the current use of SPHEREPACK. The precision of our calculation can be described by the difference of calculated properties in two runs: those with $N_\theta = 36, N_\varphi = 72$ versus those with $N_\theta = 72, N_\varphi = 144$. The difference is not visually identifiable when plotted in Fig. 2.1.

2.2.2 Isotropic-nematic interface: spatially inhomogeneous case

The main task of this work is the study of the isotropic-nematic interface, where the structure described by the segmental density distribution function varies from an isotropic state to a nematic state smoothly. The presence of the interface destroys the rotational symmetry of ϕ about the nematic director; the propagator q needs to be treated with complete dependencies on the spatial variable $\mathbf{r}$, arc variables s, polar angle θ and azimuthal angle φ, calculated from Eq. 2.9.

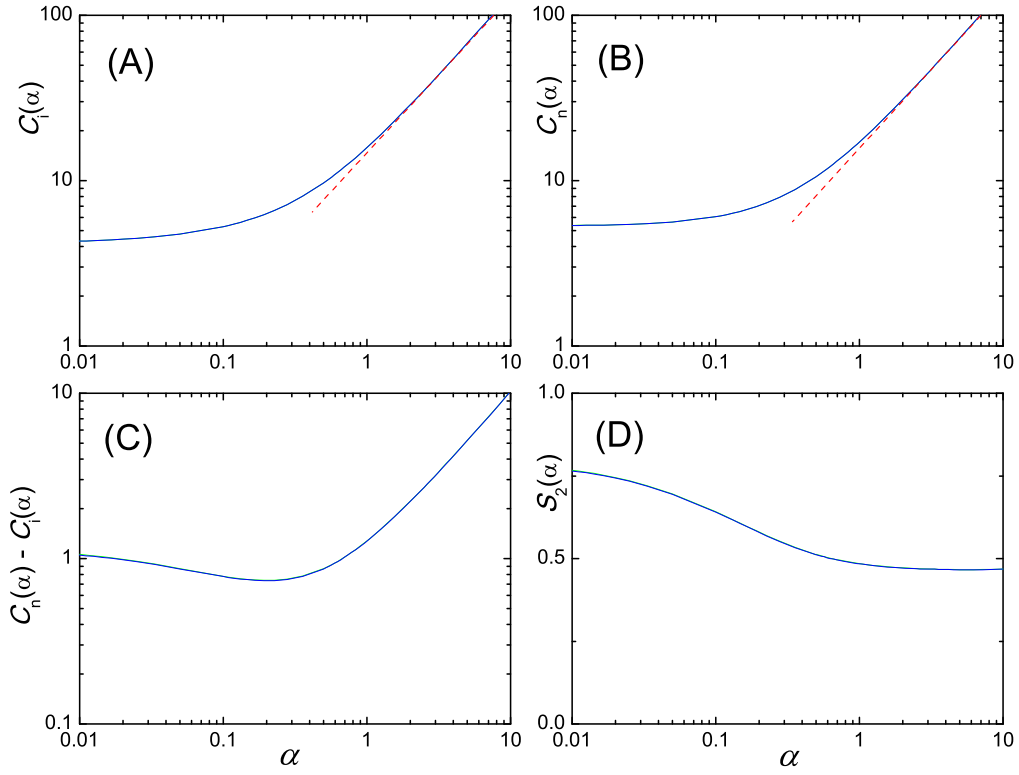

Figure 2.1: (A) Reduced segment density of the isotropic phase $C_{\rm i}$, (B) reduced segment density of the nematic phase $C_{\rm n}$, (C) the difference $C_{\rm n} - C_{\rm i}$, and (D) orientational order parameter S_2 at the isotropic-nematic phase transition as functions of the flexibility parameter $\alpha \equiv L/a$. Our results of $C_{\rm i}(\alpha = 0) = 4.1963$, $C_{\rm n}(\alpha = 0) = 5.3343$ and $S_2(\alpha = 0) = 0.7902$ fully agree with results [72, 16, 86]. We have also added dashed lines to plots (A) and (B), which represent $C_{\rm i}(\alpha \gg 1) = 13.0495\alpha$ and $C_{\rm n}(\alpha \gg 1) = 14.0769\alpha$ and agree with results [16, 118].

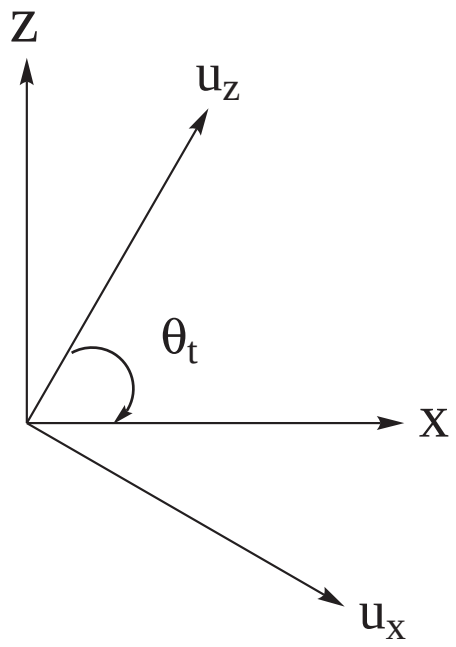

Figure 2.2: Schematic coordinate system. The interface normal is along the x direction and the bulk nematic director is along the $\mathbf{u}_z$ direction, which defines the reference director for the unit vector $\mathbf{u}$. The tilt angle θ_t is defined to be the angle between the x-axis and $\mathbf{u}_z$. The spatial direction y coincides with $\mathbf{u}_y$, both pointing into paper.

It turns out that not all three components of $\mathbf{r}$ are needed to describe the system with a flat interface. Considering the coordinate system shown in Fig. 2.2, we assume that the isotropic-nematic interface is in the y-z plane near $x = 0$, so that the physical properties vary as functions of x and $\mathbf{u}$ only. As previously noted [32, 80, 24], the direction of the nematic director of the nematic phase to the right of the $x = 0$ plane, $\mathbf{u}_z$, should be treated as an independent parameter in the system. The unit vector $\mathbf{u}$ is specified in the $\mathbf{u}$ space, where $\mathbf{u}_z$ makes an tilt angle θ_t with respect to the x axis. With the definition of the coordinate system where $\mathbf{u}_y$ coincides with the y-axis, the polar angle θ can be defined from $\cos\theta = \mathbf{u} \cdot \mathbf{u}_z$ and azimuthal angle φ from $\sin\theta\cos\varphi = \mathbf{u} \cdot \mathbf{u}_x$.

Across the entire x-space, the chemical potential per chain μ remains as a con-

stant. This allows us to define a grand thermodynamic potential, $\Xi = nF - n\mu$, in reduced form,

$$\frac{\Xi L d}{k_B T A C} = -\bar{\mu}\int \mathrm{d}\bar{x}\,\mathrm{d}\mathbf{u}\phi(\bar{x},\mathbf{u}) + \ln\left(\frac{C}{Q}\right)\int \mathrm{d}\bar{x}\mathrm{d}\mathbf{u}\phi(\bar{x},\mathbf{u}) - \int \mathrm{d}\bar{x}\,\mathrm{d}\mathbf{u}w(\bar{x},\mathbf{u})\phi(\bar{x},\mathbf{u}) + C\int \mathrm{d}\bar{x}\,\mathrm{d}\mathbf{u}\mathrm{d}\mathbf{u}'\phi(\bar{x},\mathbf{u})|\mathbf{u}\times\mathbf{u}'|\phi(\bar{x},\mathbf{u}'), \tag{2.20}$$

where A is the area of the flat interface, $\bar{\mu} \equiv \mu/k_B T$, and the spatial variable is rescaled by

$$\bar{x} \equiv x/L. \tag{2.21}$$

The partition function of a single chain can be calculated from $Q = \int \mathrm{d}\bar{x}\int \mathrm{d}\mathbf{u}q(\bar{x},\mathbf{u},1)$ $/[4\pi\int \mathrm{d}\bar{x}\mathrm{d}\mathbf{u}\phi(\bar{x},\mathbf{u})]$.

Using the coordinate system in Fig. 2.2, we rewrite Eq. 2.9 as

$$\frac{\partial}{\partial s}q(\bar{x},\mathbf{u},s) = \left[\alpha\nabla^2_{\mathbf{u}} - (\cos\theta_t u_z + \sin\theta_t u_x)\frac{\partial}{\partial\bar{x}} - w(\bar{x},\mathbf{u})\right]q(\bar{x},\mathbf{u},s) \tag{2.22}$$

where $u_x = \mathbf{u}\cdot\mathbf{u}_x = \sin\theta\cos\varphi$ and $u_z = \mathbf{u}\cdot\mathbf{u}_z = \cos\theta$. The self-consistent field is given by

$$w(\bar{x},\mathbf{u}) = \Lambda + 2C\int \mathrm{d}\mathbf{u}'|\mathbf{u}\times\mathbf{u}'|\phi(\bar{x},\mathbf{u}'). \tag{2.23}$$

from minimization of Eq. 2.20 with respect to $\phi(\bar{x},\mathbf{u})$. Note that we have used a constant $\Lambda = 1 - \bar{\mu} + \ln(C/Q)$ in the actual calculation.

We now illustrate the numerical method used to solve Eq. 2.22, using the notations $\hat{F}_1 \equiv -(\cos\theta_t u_z + \sin\theta_t u_x)(\partial/\partial\bar{x}) - w(\bar{x},\mathbf{u})$ and $\hat{F}_2 \equiv \alpha\nabla^2_{\mathbf{u}}$. According to the Crank-Nicolson algorithm, we can decouple the numerical process of solving $q(\bar{x},\mathbf{u},s)$ into two steps

$$\left[1 - \frac{\Delta s}{2}\hat{F}_1\right]q(\bar{x},\mathbf{u},s+\Delta s/2) = \left[1 + \frac{\Delta s}{2}\hat{F}_2\right]q(\bar{x},\mathbf{u},s), \tag{2.24}$$

$$\left[1 - \frac{\Delta s}{2}\hat{F}_2\right]q(\bar{x},\mathbf{u},s+\Delta s) = \left[1 + \frac{\Delta s}{2}\hat{F}_1\right]q(\bar{x},\mathbf{u},s+\Delta s/2). \tag{2.25}$$

At the first step, the intermediate $q(x,\mathbf{u},s+\Delta s/2)$ is obtained through solving the linear set of equations [93] because of the *tridiagonal* matrix property of the

operator $1-(\Delta s/2)\hat{F}_1$ for the spatial variable $\bar{x}$. At the second step, similar to the processes described by Eqs. 2.16 - 2.19 used to solve Eq. 2.14, $q(\bar{x},\mathbf{u},s+\Delta s)$ can also be calculated directly from Eq. 2.25. Notably, Eqs. 2.24 and 2.25 can be reduced into Eq. 2.15 if the propagator q is independent of $\bar{x}$. Once the properties at the step $s+\Delta s$ are known, we go back to Eqs. 2.24 and 2.25 for the next iteration. The chemical potential $\bar{\mu}$ is determined from the phase balancing condition in section 2.2.1 and can be related to C_{i} in Fig. 2.1 (A) by $\bar{\mu}=\ln C_{\mathrm{i}}+(\pi C_{\mathrm{i}}/2)+1$.

The interface profile changes more drastically at the center and varies more smoothly farther away. Using a rescaled spatial variable $\xi(\bar{x})\equiv\tanh(\bar{x}/\eta)$ instead of $\bar{x}$ to describe the isotropic-nematic interface [24], we can effectively place more grid points near the interface by evenly dividing the ξ space. Then, the spatial differential operator in Eq. 2.22 can be rewritten as $\partial/\partial\bar{x}=[(1-\xi^2)/\eta](\partial/\partial\xi)$, where the parameter η was manually adjusted to approximately match the interfacial width. Note that the interval $\bar{x}\in[-\infty,\infty]$ now becomes $\xi\in[-1,1]$ accordingly. We use $n_\xi=51$ equally spaced discrete points in the interval $[-1,1]$, i.e. $\Delta\xi=0.04$.

The self-consistent calculation started with an initial guess for the self-consistent field $w(\bar{x},\mathbf{u})$, taken as a step function where $w(\bar{x},\mathbf{u})=0$ to the left of $x=0$ and $w(\bar{x},\mathbf{u})=w_b(\mathbf{u})$ (a result from the bulk calculation) to the right. The Picard iteration method used in our previous study of a wormlike chain brush [27] was utilized to update the $w(\bar{x},\mathbf{u})$ function iteratively step-by-step. At every iteration step, a function of $N_\xi\times N_\theta\times N_\varphi\times N_{\bar{s}}=51\times36\times72\times5001=6.61\times10^8$ variables was calculated through Eq. 2.22. The iteration continued until the convergence criterion imposed on the field was met, $\mathrm{MAX}|w^{new}(\bar{x},\mathbf{u})-w^{old}(\bar{x},\mathbf{u})|<10^{-3}$.

2.3 Results and discussion

In this section we discuss the main results obtained through a numerical solution to the SCFT presented in the last section. The orientational ordering of the polymer segments is normally considered by a traceless matrix [26]. This matrix is a function of the spatial variable $\bar{x}$ across the interface and can be calculated from the statistical average of the tensor $(3\mathbf{uu} - \mathbf{I})/2$,

$$\mathbf{S}(\bar{x}) \equiv \frac{1}{2}\frac{\int \mathrm{d}\mathbf{u}(3\mathbf{uu} - \mathbf{I})\phi(\bar{x}, \mathbf{u})}{\int \mathrm{d}\mathbf{u}\phi(\bar{x}, \mathbf{u})}. \tag{2.26}$$

It has been noted before [24] that the principal nematic director changes across the isotropic-nematic interface. Mathematically the principal order parameter $S(\bar{x})$ and the biaxiality parameter $P(\bar{x})$ can be found from the diagonalization of the above matrix [24],

$$\mathcal{U}^{-1}\mathbf{S}(\bar{x})\mathcal{U} = \begin{bmatrix} S(\bar{x}) & 0 & 0 \\ 0 & \frac{1}{2}(P(\bar{x}) - S(\bar{x})) & 0 \\ 0 & 0 & -\frac{1}{2}(P(\bar{x}) + S(\bar{x})) \end{bmatrix},$$

where $\mathcal{U}$ is a 3×3 unitary matrix.

For a number of representative values of α, the profiles of the segmental density $C\phi(\bar{x})$, the order parameter $S(\bar{x})$, and the biaxiality $P(\bar{x})$ are plotted as functions of $\bar{x}$ in Figs. 2.3 - 2.5. Within each plot, we have further displayed curves for a few typical values of the tilt angle θ_t. Both $C\phi(\bar{x})$ and $S(\bar{x})$ display a narrowest interfacial width when $\theta_t = \pi/2$ and a widened interfacial width as θ_t decreases. A comparison between Figs. 2.3 and 2.4 reveals that the variation of the density function slightly moves towards the nematic side in comparison with the variation of the order-parameter profile. In all cases, the density profiles show a depletion before entering into the interface from the isotropic side. The density profiles for most values of α increase smoothly to the values at the nematic side, except for intermediate values of α; an example can be seen in Fig. 2.3 (C) where the density profiles are enhanced before entering into the nematic state on the right hand side, when $\alpha = 2.5$. Correspondingly, a similar enhancement of orientational ordering can be found in Fig. 2.4 (C).

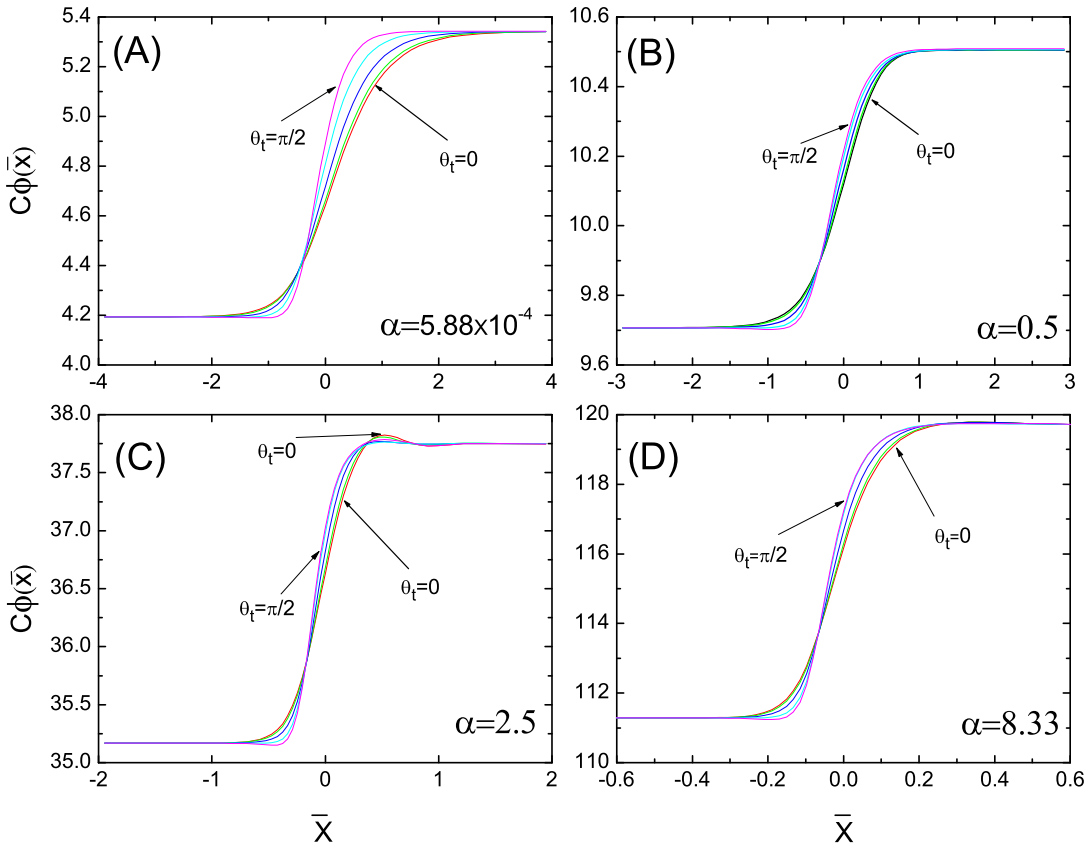

Figure 2.3: Density profile $C\phi(\bar{x})$ of the isotropic-nematic interface as a function of $\bar{x} \equiv x/L$ with a few typical values of the tilt angle θ_t for different flexibilites of wormlike chain, (A) $\alpha = 5.88 \times 10^{-4}$; (B) $\alpha = 0.5$; (C) $\alpha = 2.5$ and (D) $\alpha = 8.33$. Red, green, blue, cyan and pink curves represent $\theta_t = 0, \pi/9, 2\pi/9, \pi/3$ and $\pi/2$, respectively.

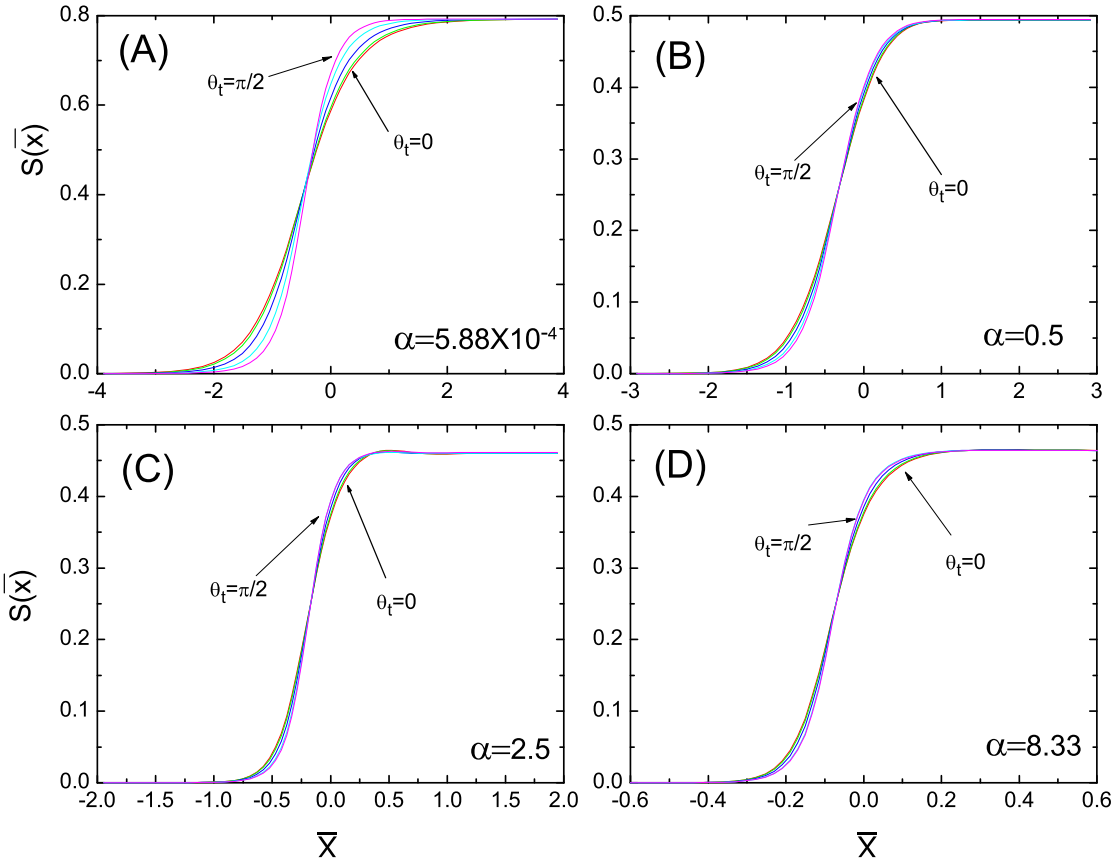

Figure 2.4: Order parameter profile $S(\bar{x})$ of the isotropic-nematic interface as a function of $\bar{x} \equiv x/L$ with a few typical values of tilt angle θ_t for different flexibilities of wormlike chain, (A) $\alpha = 5.88 \times 10^{-4}$; (B) $\alpha = 0.5$; (C) $\alpha = 2.5$ and (D) $\alpha = 8.33$. Red, green, blue, cyan and pink curves represent the tilt angle $\theta_t = 0, \pi/9, 2\pi/9, \pi/3$ and $\pi/2$, respectively.

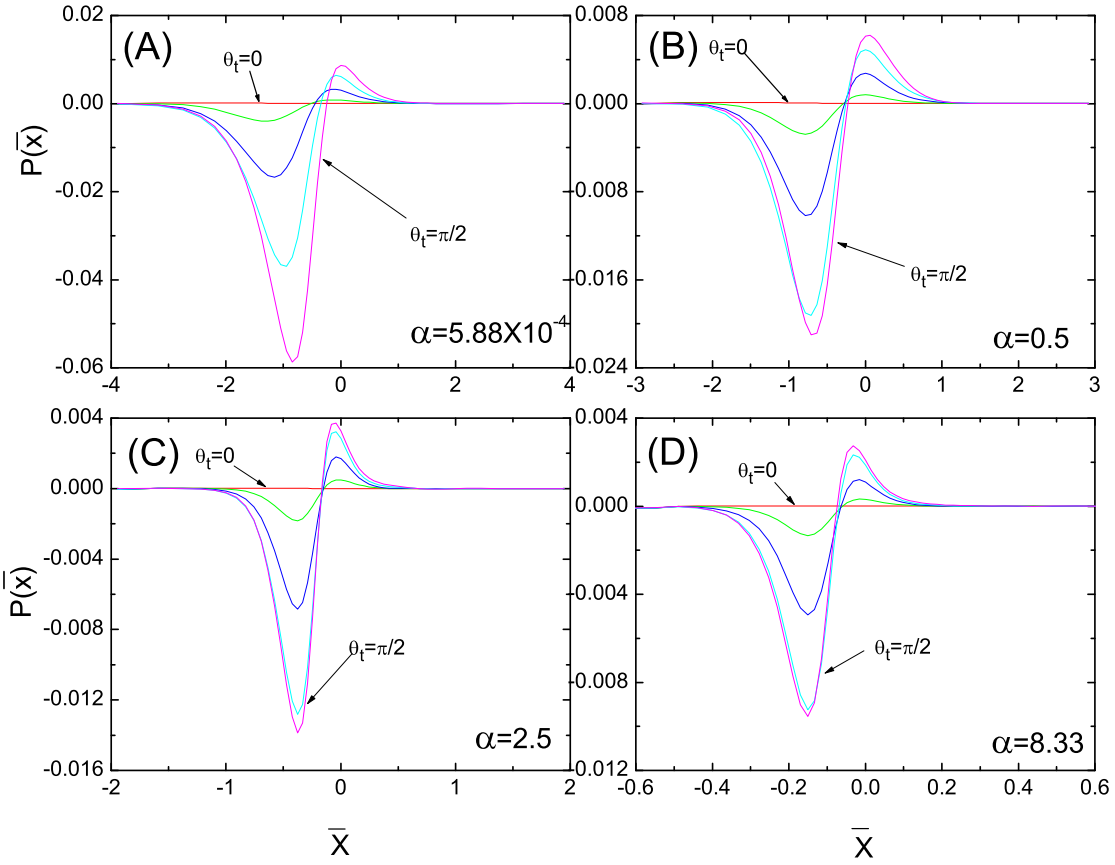

Figure 2.5: Biaxiality profile $P(\bar{x})$ of the isotropic-nematic interface as a function of $\bar{x} \equiv x/L$ with a few typical values of the tilt angle θ_t for different flexibilities of wormlike chains, (A) $\alpha = 5.88 \times 10^{-4}$; (B) $\alpha = 0.5$; (C) $\alpha = 2.5$ and (D) $\alpha = 8.33$. Red, green, blue, cyan and pink curves represent the tilt angle $\theta_t = 0, \pi/9, 2\pi/9, \pi/3$ and $\pi/2$, respectively.

Fig. 2.5 (A) shows a weak but significant biaxiality across the interface. In the $\theta_t = \pi/2$ case, $P(\bar{x})$ varies more drastically because of the anchoring effect. $\theta_t = 0$ is an interesting case where $P(\bar{x})$ reduces to zero across the entire region; the system actually recovers an axial symmetry about the nematic director in the far right-hand side. Another feature in this figure is the reduction of the magnitude of the biaxiality as α increases — a more flexible polymer can make easier structural change to facilitate the crossover from the isotropic to nematic sides.

The interfacial tension is normally defined as the interface excess free energy per area, in comparison to that in a bulk phase. For this purpose we define the interfacial tension,

$$\sigma \equiv \left(\Xi - \Xi_{\text{isotropic}}\right)/A. \tag{2.27}$$

In reduced symbols, this can be calculated from

$$\frac{\sigma L d}{k_B T} = -\int \mathrm{d}\bar{x} \left\{ \int \mathrm{d}\mathbf{u} C\phi(\bar{x}, \mathbf{u}) \left[\frac{1}{2} w(\bar{x}, \mathbf{u}) + 1 \right] + C_i \left[\ln C_i + \frac{\pi C_i}{4} - \bar{\mu} \right] \right\}, \tag{2.28}$$

where it should be understood that Eq. 2.23 was used to reduce the longer version in Eq. 2.20: the minimization of the free energy with respect to the density profile has already been considered. The term associated with the second set of square brackets in the above expression is the negative osmotic pressure of the isotropic phase; subtracting a reference Ξ by using the nematic Ξ works as well, because this term is identical to $\Xi_{\text{isotropic}}$. The term associated with the first set of brackets can be regarded as the osmotic pressure at the position $\bar{x}$. The entire expression can also be considered as the reduced work performed (per unit area) to move polymer segments from $x = -\infty$, overcoming the osmotic pressure difference, to construct an isotropic-nematic interface.

Fig. 2.6 shows the dependence of interfacial tension $\sigma(\alpha, \theta_t)$ on the flexibility parameter α for tilt angle $\theta_t = 0$ and $\pi/2$ in double logarithmic scales. Other cases of θ_t display similar curves, falling between these two curves. Note that the vertical axis is reduced by using, among other parameters, the total polymer L. An increase in flexibility allows rodlike molecules to make easier accommodation to the interface change, hence we see a reduction of the surface tension. Eventually, as polymers become more flexible in the large α region, the dominating length scale

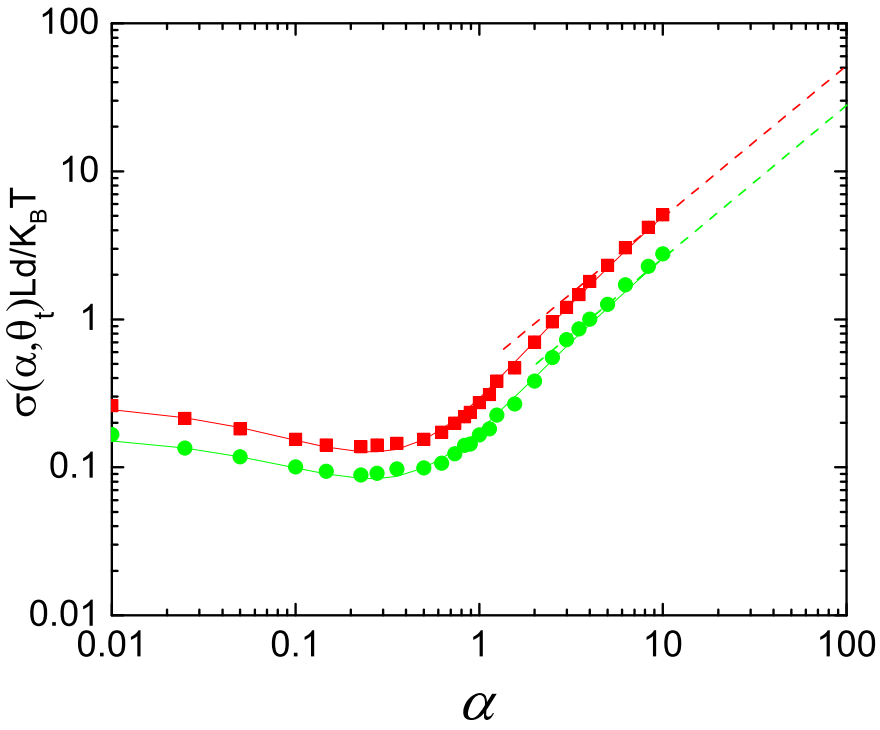

Figure 2.6: The isotropic-nematic interfacial tension for systems having various degrees of flexibility α at tilt angle $\theta_t = 0$ and $\pi/2$ (represented by squares and circles, respectively). Red and green curves are the corresponding fitting results according to Eqs. 2.30-2.32. We also added dashed lines $\sigma(\alpha, \theta_t = 0)Ld/k_BT = 0.5635\alpha$ (red) and $\sigma(\alpha, \theta_t = \pi/2)Ld/k_BT = 0.2818\alpha$ (green) in the large α region to indicate the asymptotic behavior.

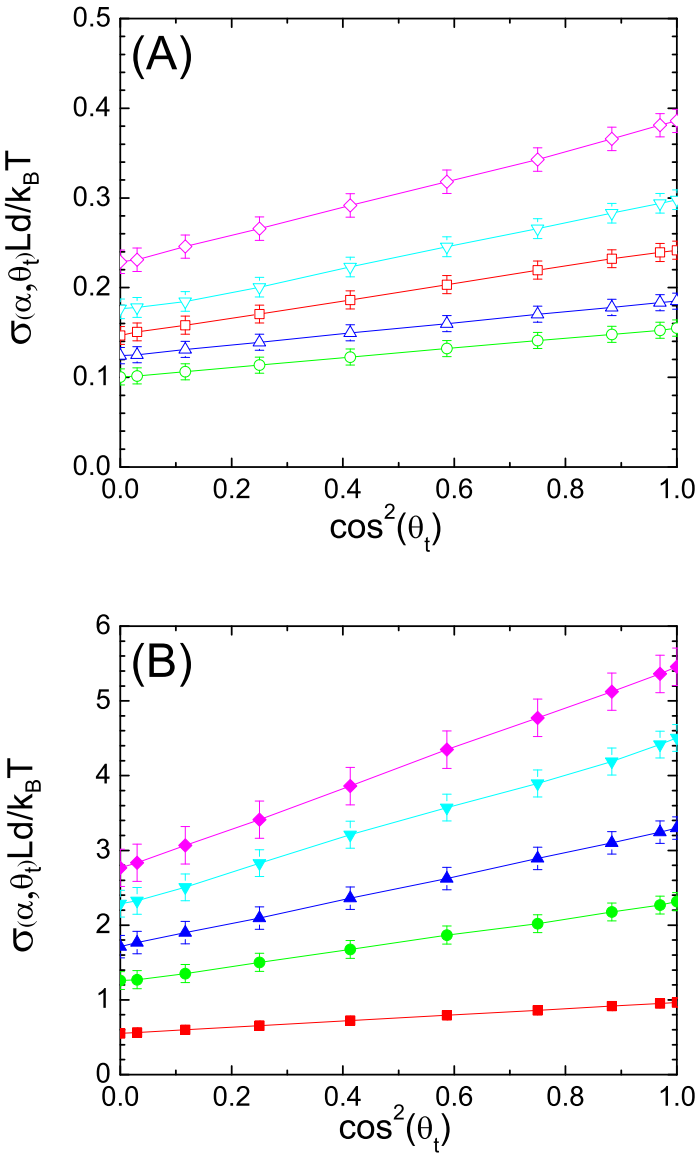

Figure 2.7: Reduced isotropic-nematic interfacial tension defined in Eq. 2.28 as a function of the tilt angle θ_t. (A) Open squares, circles, up triangles, down triangles and diamonds represent $\alpha = 0.01, 0.1, 0.5, 1$ and 1.25, respectively. (B) Filled squares, circles, up triangles and down triangles and diamonds represent $\alpha = 2.5, 5, 6.25, 8.33$ and 10, respectively.

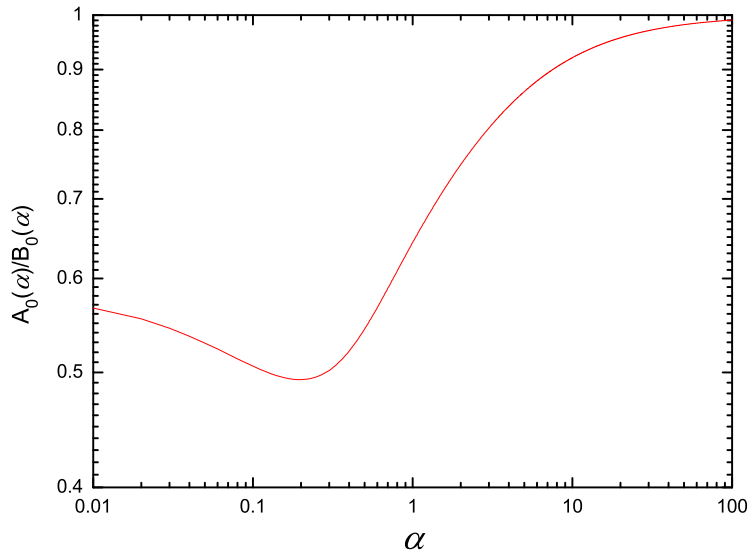

Figure 2.8: The ratio of the anchoring energy and the interfacial tension for systems having various degrees of flexibility α.

Table 2.1: Fitted coefficients in Eqs. 2.30-2.32.

	a_0	a_1	a_2	a_3	b_1	b_2
$A_0(\alpha)$	0.1076	0.4240	0.0721	2.6204	17.710	9.3023
$B_0(\alpha)$	0.1852	1.1654	0.0723	5.0579	17.273	17.948

is a, no longer L. Scaled by a instead of L, the surface tension should approach a constant in this limit [24, 50]. Going back to the plot in Fig. 2.6 where the vertical axis is scaled by L, the interfacial tension is then linearly dependent on L/a which is α. We indeed see that the interfacial curves increase linearly in the large α limit.

An interesting comparison can be seen between the variation of the interfacial tension in Fig. 2.6 and variation of the magnitude of the change in $C_{\mathrm{n}} - C_{\mathrm{i}}$ in Fig. 2.1 (C), which is also reduced in this work by a factor of L. In general, one would expect that the interfacial tension should be inversely proportional to the interface width. In our case, however, as discussed below the interface width has a monotonic decrease as a function of α in the large α region while the interfacial tension has a completely different trend. In fact, the variation of the interfacial tension is also determined by the magnitude of the change the interface goes through; in our case, the change of $C_{\mathrm{n}} - C_{\mathrm{i}}$ is mostly responsible for the change in $\sigma(\alpha, \theta_t)$.

Another important perspective can be gained from plotting the interfacial tension as a function of $\cos\theta_t$ for typical values of α, shown in Fig. 2.7. We found that for any α the interfacial tension monotonically decreases with the increase of the tilt angle θ_t. This implies that the global free energy minimum can be attained at $\theta_t = \pi/2$, if the nematic director on the far right-hand side is allowed to rotate. The same theoretical conclusion was previously drawn for isotropic-nematic interfaces consisting of rigid-rods [18, 104, 32] or flexible wormlike chains [24, 33]. This observation qualitatively agrees with a recent experimental observation [15].

We can generally show from an analysis of the functional dependence on θ_t in Eq. 2.22 that the interface can only be a function of the variable $\cos^2\theta_t$. Physically, this reflects the symmetry property, $\sigma(\alpha,\theta_t) = \sigma(\alpha,\pi+\theta_t)$, because of a reflection symmetry against the $z=0$ plane in Fig. 2.2. Doi and Kuzuu [32], for example, even proposed that the interfacial tension for a rod system ($\alpha = 0$) can be approximated by

$$\frac{\sigma(0,\theta_t)Ld}{k_BT} = 0.257(1+1.75\cos^2\theta_t)^{1/2} \tag{2.29}$$

which has values higher than our results over the entire region of $\cos\theta_t$ when $\alpha = 0$. A somewhat surprising result from the current calculation is that the dependence of σ in $\cos\theta_t$ is parabolic within the numerical errors and our numerical results can be well captured by a simple empirical formula,

$$\frac{\sigma(\alpha,\theta_t)Ld}{k_BT} = A_0(\alpha)\cos^2\theta_t + B_0(\alpha), \tag{2.30}$$

which is similar to the Rapini-Papoular model [96] estimating the interfacial tension. The coefficients $A_0(\alpha)$ and $B_0(\alpha)$ were obtained from fitting to the numerical data and can be further represented by

$$A_0(\alpha) = \sum_{m=0}^{3} a_m\alpha^m \Big/ \left(1+\sum_{m=1}^{2} b_m\alpha^m\right) \tag{2.31}$$

$$B_0(\alpha) = \sum_{m=0}^{3} a_m\alpha^m \Big/ \left(1+\sum_{m=1}^{2} b_m\alpha^m\right) \tag{2.32}$$

where the constants a_m and b_m are listed in Table 2.1. This dependence is displayed in Fig. 2.7 as straight lines, where the horizontal axis is $\cos^2\theta_t$. The dimensionless anchoring strength, i.e., the ratio of the anchoring energy and the interfacial tension as the function of α can be directly calculated from $A_0(\alpha)/B_0(\alpha)$, which is shown in Fig. 2.8 based on Eqs. 2.30 - 2.32 and the fitted coefficients in Table 2.1. In the rod-like chain limit, $\alpha \to 0$, our calculation shows $A_0(0)/B_0(0) \to 0.58$; in the flexible chain limit, $\alpha \to \infty$, $A_0(\infty)/B_0(\infty) \to 1.0$; in the vicinity of $\alpha = 0.3$ there is a minimum value of anchoring strength 0.5. Our theoretical prediction on the dimensionless anchoring strength, however, is far smaller than the experimental

observation in which Puech et al studied on the tactoids in aqueous dispersions of carbon nanotubes and found the corresponding value is approximately equal to 3.4 [95]. So far, the reason is not clear.

The characteristics of the interface can also be examined by interfacial widths measured from the density- and orientational order-parameter profiles as functions of $\bar{x}$. Because of the non-monotonic variation of these profiles, we have decided to use the second-moment definition,

$$\bar{W} = 2\sqrt{\langle \bar{x}^2 \rangle - \langle \bar{x} \rangle^2}, \tag{2.33}$$

where the average is evaluated by

$$< A(\bar{x}) >= \frac{\int_{-\infty}^{\infty} A(\bar{x}) |\frac{\mathrm{d}f(\bar{x})}{\mathrm{d}\bar{x}}| \mathrm{d}\bar{x}}{\int_{-\infty}^{\infty} |\frac{\mathrm{d}f(\bar{x})}{\mathrm{d}\bar{x}}| \mathrm{d}\bar{x}} \tag{2.34}$$

with the function $f(\bar{x})$ being $C\phi(\bar{x})$ for the density interfacial width or $S(\bar{x})$ for the orientational interfacial width.

The interface widths $W_\phi(\alpha, \theta_t)$ calculated from the profile of segmental density and $W_S(\alpha, \theta_t)$ from order parameter for $\theta_t = 0$ (squares) and $\pi/2$ (circles) are displayed in Fig. 2.9. Other values of θ_t give rise to curves in between these two. In both $\bar{W}_\phi \equiv W_\phi/L$ and $\bar{W}_S \equiv W_S/L$, the interfacial widths decrease with an increase in α. Those systems with $\theta_t = 0$ have a broader interface width than those with $\theta_t = \pi/2$, for a fixed α; this result is consistent with earlier studies [18, 24, 33]. In the small α regime, the interface width has a sharp drop with the increase of α. In the large α region, we anticipate that the interface width is predominantly controlled by the Kuhn length a, $W \sim a$. Reflected in these plots where W is scaled by L, we see an $1/\alpha$ behavior in the large α region.

As demonstrated in Appendix A, in the limit of $\alpha \ll 1$, the general formalism developed for the wormlike isotropic-nematic interface in this work exactly recovers that of the interface problem of rigid rods, originally developed by Onsager for the bulk phase [90], and later generalized by others for the description of the interfacial problem [80, 18, 17].

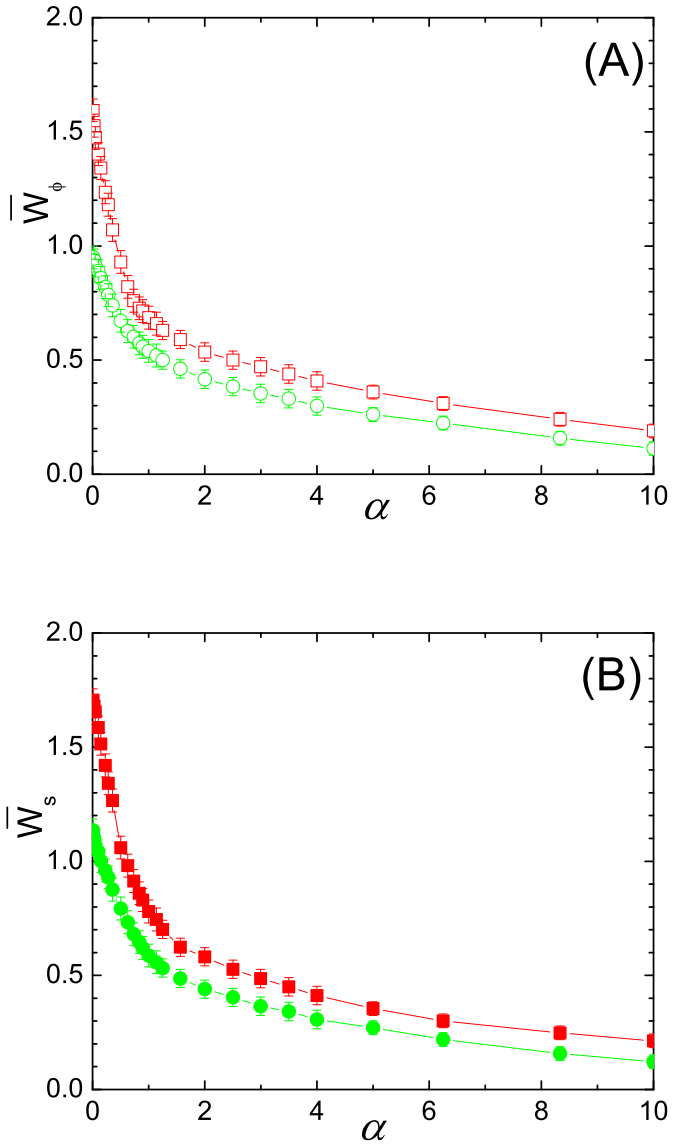

Figure 2.9: Reduced interface width $\bar{W} \equiv W/L$ defined in Eq. 2.33 for systems with various flexibility α at two tilt angles, $\theta_t = 0$(squares) and $\pi/2$ (circles). $\bar{W}_\phi$ (A) and $\bar{W}_S(B)$ represent the interfacial widths calculated from the density and order parameter profiles, respectively.

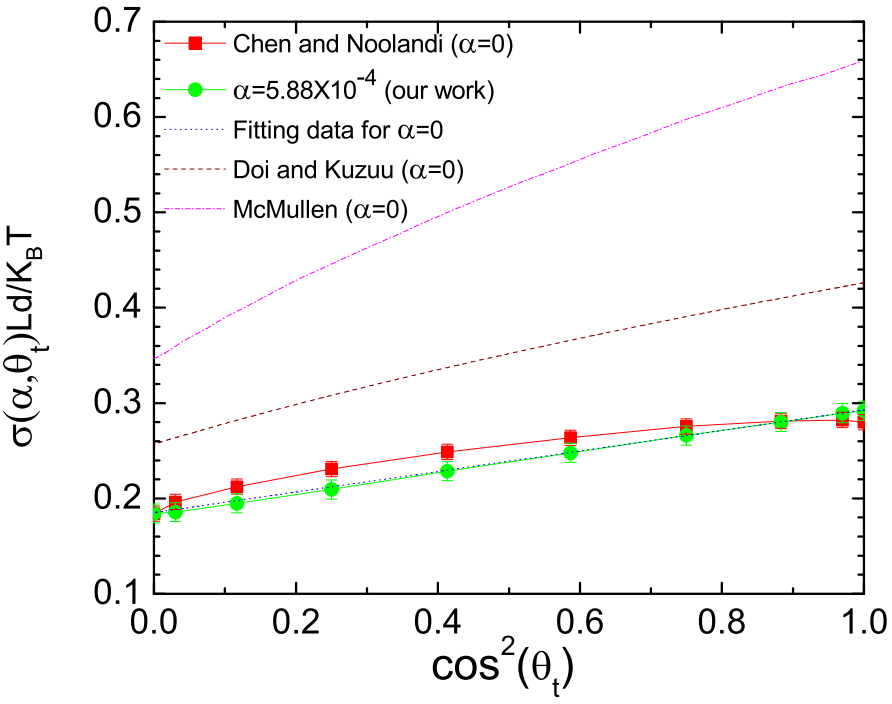

Figure 2.10: Interfacial tension for different tilt angles θ_t in the rod-like chain limit $\alpha \ll 1$. The curve going through squares was obtained by Chen and Noolandi [18], whose results almost overlap with those of van der Schoot [115]. The curve going through circles represents our calculated results for $\alpha = 5.88 \times 10^{-4}$. The dotted curve was extrapolated from Eqs. 2.30-2.32, by setting $\alpha = 0$. The dashed curve was obtained by Doi and Kuzuu [32]. The dash-dotted curve was obtained by McMullen [80].

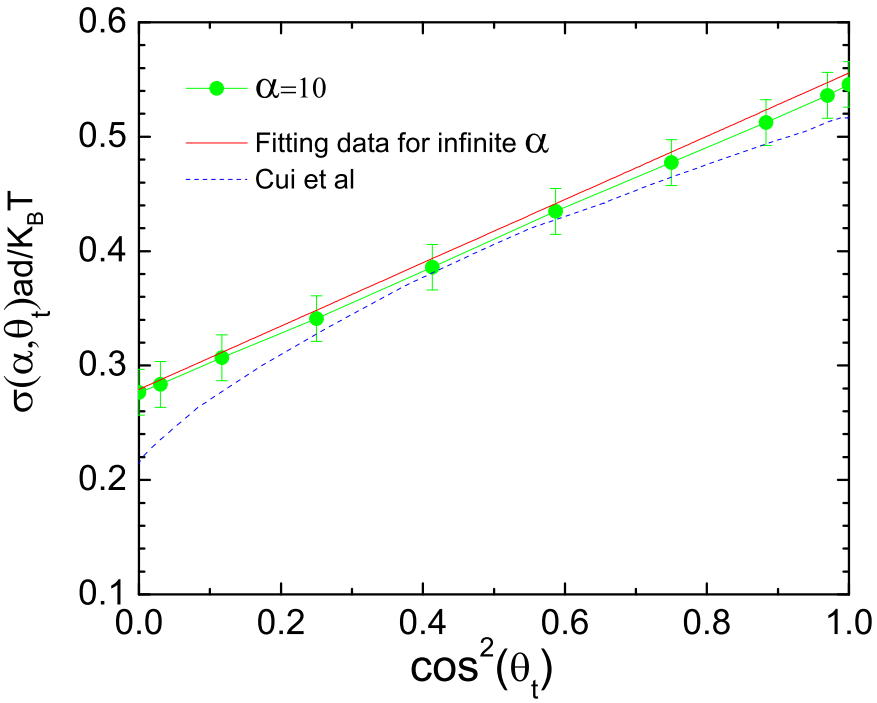

Figure 2.11: Interfacial tension for different tilt angles θ_t in the flexible chain limit, $\alpha \gg 1$. The curve with circles represents our results for $\alpha = 10$, and the solid curve is an extrapolation from Eqs. 2.30-2.32 by taking $\alpha \to \infty$. The dashed curve was obtained by Cui, Akcakir and Chen [24].

In Fig. 2.10, we display the interfacial tension previously found in this limiting case. Both results by Doi-Kuzuu [32] and McMullen [80] can be seen far above the results found in the current work (filled circles); this is caused by the trial density functions used in these theoretical approaches. The result [18] from a numerical treatment of the Onsager problem, without the explicit consideration of the biaxiality, given in the plot as squares, is also above this calculation and cannot be represented by the quadratic function in $\cos\theta_t$; neglecting biaxiality is probably the cause of this deviation.

In the flexible-chain limit, $L \gg a$, the formalism developed in this work also recovers those used by Cui, Akcakir and Chen [24], who have studied the isotropic-

nematic interface formed by long wormlike polymers. In this limit the characteristic length scale is a and we can show that the reduced surface tension $\sigma ad/k_BT$ approaches a constant. In Fig. 2.11, we plot the data found from the current work for $\alpha = 10$, which can be compared with the projected $\alpha \gg 1$ result, taken from Eqs. 2.30 - 2.32 in the large α limit. It is not clear where the discrepancy between the result in Reference [24] and our current calculation comes from, seen in this plot.

Chen, Sato and Teramoto measured the surface tension of polysaccharide molecules as a function of molecular weight M, which can be translated into contour length L in this model. The molecules in these systems can be considered almost rigid. It is interesting to note that their measurement gives a σM that decreases as M increases, which is consistent with the qualitative feature of $\sigma Ld/k_BT$ in the small L/a region, found in this work. Later, Chen and Gray measured the interfacial tension [13] in the system of aqueous suspensions of cellulose crystallites through changing the crystallites concentration and obtained the relatively satisfied results compared to theoretical predictions [18, 80] after considering the equivalent hard-core diameters of the rod-like particles. The theoretical results [18, 17, 80, 32] on the prediction of interfacial tension $\sigma Ld/k_BT$ for $L \ll a$, however, are usually far lower than other experimental observation [15, 13]. It is not clear whether we can ascribe the discrepancy to the flexibility on the polymer chain, to the polydispersity in molecular weight, to the soft attractive interactions between the polysaccharide molecules [15], or the definition of the effective diameter [13] of a polymer segment in the experiment.

2.4 Conclusion

In this work we calculated the interfacial properties of the isotropic-nematic interface, from a model that contains the Onsager interaction for the description of the orientational-dependent interaction and the wormlike-chain statistics for the description of the flexibility of chains [61]. We particularly paid attention to the flexibility dependence, connecting to interfacial properties previously studied in two limits: rods and flexible chains. One particularly interesting case is that the reduced surface tension, $\sigma Ld/k_BT$, where L and d are the polymer's total contour

length and excluded-volume diameter, decreases as a rigid chain is softened, goes through a minimum, and then increases linearly in the flexible limit shown in Fig. 2.6. This decrease near the rigid region qualitatively explains a recent experimental observation [15].

We have also verified that the general trend of the tilt-angle dependence in a lyotropic isotropic-nematic interface, reflected by the surface tension and seen previously in rod- and flexible-chain models, is also valid in the semiflexible case, shown in Fig. 2.7. Weak biaxialities have been found in all systems considered in this work, consistent with that seen in models describing these two limits.

We described the usage of the software package SPHEREPACK in treating the orientational dependence of the physical properties in this system. This method can be easily implemented for related wormlike-polymer problems, that requires the numerical solution to a modified differential equation with both positional and orientational dependencies.

Chapter 3

Microphase Separated Structures in Wormlike Diblock Copolymers

3.1 Introduction

It is now well established experimentally that a melt of AB diblock copolymers can phase-separate into A-rich and B-rich micro-domains on nanoscales [5, 52]. As one of the most successful examples in polymer theory, the self-consistent field theory (SCFT), which originated from the work of Edwards [34] and was developed further by Helfand and co-workers [53, 55, 56, 54], has predicted a phase diagram in terms of essential parameters of the system, that divides into stable regions for idealized AB diblock copolymer micro-structures [39, 77]; the SCFT approach has become an indispensable tool, coupled with various experimental approaches, to explore problems in this research area.

The basic ingredients of a SCFT for an AB diblock copolymer melt with an A/B volume faction f are: a statistical weight for the polymer configuration and the interaction between A-polymer and B-polymer. In most theoretical development so far, an Edwards weight has been employed as the statistical weight [34, 31] and the Flory-Huggins interaction energy between A- and B- polymer components has been adopted by assuming a phenomenological Flory-Huggins parameter χ [38]. The Edwards weight, also known as a Gaussian-chain (GSC) model because it

includes a quadratic Gaussian-type energy, is suitable for description of a *flexible* polymer chain that has a total polymer contour length L and Kuhn length a [31]. According to SCFT, these ingredients yield a theory hence the resulting phase diagram that depends on two simple parameters: f and $\chi L/a$, where $L/a \gg 1$ is normally assumed in the theory, for a copolymer melt consisting of flexible AB diblock copolymers [39].

A much-less explored theoretical system is the phase behavior of a *wormlike* AB diblock copolymer melt. A wormlike polymer model can be used to describe a semiflexible polymer where approximately within a segment of a persistence length λ the polymer appears rigid. In a free space, a discrete version of a wormlike chain (WLC) model was studied by Kratky and Porod [68] and a continuous version was studied by Saito, Takahashi and Yunoki [100]. The model is appropriate for any ratio of L/λ; on one hand, in free space it recovers GSC results in the limit of $L/\lambda \gg 1$ where $2\lambda \sim a$ can be identified, and on the other hand, it crosses over to an interesting rigid molecule limit where $L/\lambda \ll 1$. A SCFT for AB diblock copolymer melt can be formulated based on a WLC model [41, 39], which can be shown to contain three parameters, f, $\chi L/a$, and L/a, where a is now identified with twice persistence length $a \equiv 2\lambda$. The additional L/a dependence gives rise to a theory that can be used to examine the effects of persistency, which is reflected by the finite L/a ratio, on the phase behavior of a AB diblock copolymer melt.

The effective Kuhn length a (or twice the persistence length λ) is a sole relevant length scale within the STY model, which is identified through the mean square end-to-end distance in the $L/a \gg 1$ limit, $\langle R^2 \rangle = La$ [100]. Both a and the persistence length λ are different from the "bare" Kuhn length b, a length scale that is usually attributed to a monomer-to-monomer distance in a polymer consisting of flexible bond segments. In the more original STY version where b was used together with a (large) bending energy penalty $\beta\epsilon$ for two adjacent polymer bonds, $\lambda = \beta\epsilon b$ [100]. The use of the length scale λ in the STY model does not restrict us from exploring physics of short persistent chains; the polymer can only be a few bonds long measured by a short total polymer length L where $L/\lambda \ll 1$. Both versions of the formalism, namely, maintaining a product of two parameters to explicitly indicate the presence of b, $\beta\epsilon b$, and using a single effective a (or λ) without splitting

$\beta\epsilon$ from b, can be found in recent theoretical treatments [11].

A WLC-based SCFT differs from a GSC-based SCFT by the additional orientational dependence, which couples with the positional dependence usually seen in a GSC-based SCFT, in the probability distribution function for a polymer segment. The orientational dependence is essential for dealing with wormlike systems where orientational properties are the major concern, such as in studying the thermodynamics of polymer liquid crystals [86, 102, 16, 49] and spatially inhomogeneous polymer liquid-crystal systems [50, 74, 24, 25, 58, 12, 107, 61]. The orientational dependence is also required to render the correct physical properties for spatially inhomogeneous wormlike polymer problems where the the positional dependence is the main concern, such as the system examined in this work, where the phase separation of AB bulk polymers is considered.

AB diblock copolymers can self-organize many complicated morphologies on nanoscales, due to the immiscibility between components A and B. Matsen studied the disorder-lamellar (DL) phase transition for the symmetric AB diblock copolymer using a WLC based SCFT [76]. In comparison with flexible chains, he found the increase of chain rigidity will highly decrease the Flory-Huggins parameter describing the magnitude of the repulsive potential between segments A and B for a disordered-ordered phase transition. Furthermore, Netz and Schick [83] considered the Maier-Saupe anisotropic interaction and extended the exploration of symmetric AB diblock copolymers into smectic phases. Recently, assuming the extremely opposite chain rigidity for each block, Düchs and Sullivan [25] studied the phase behavior of rod-coil diblock copolymers by considering an Onsager type interaction. Shortly thereafter, Song *et al* [107] extended the theoretical calculations to morphologies without the rotational symmetry imposed, i.e. azimuthal effects involved. Taking a Maier-Saupe interaction into account, Shah and Ganesan [103] present a theoretical study evaluating the bridging/looping fractions in a model of coil-semiflexible multiblock copolymers. Unfortunately, all works mentioned above constrained their calculations only in one spatial dimension, so that more fascinating mesophases in higher dimension kept unexplored.

In this chapter, firstly, a general theory for AB diblock wormlike copolymers based on the SCFT is presented in Section 3.2. Subsequently, in Section 3.3,

the study on the physical properties of disordered-lamellar phase transition for symmetric and asymmetric AB diblock copolymers is illustrated by means of the implementation of split-step algorithm previously proposed by Fredrickson [39]. In Section 3.4, a new numerical strategy incorporating the spherical harmonic expansion and plane-wave spectral collocation method with a multi-step backward differentiation formula (BDF) is developed, in order to explore the complicated 3D morphologies such as hexagonal cylinders, cubic spheres, and net-like gyroids. The full phase diagrams influenced by the chain rigidity effect are shown in this section. Finally, a brief summary can be found in Section 3.5.

3.2 Self-consistent field theory for diblock copolymers

We consider a system of volume V composed of n monodisperse, indistinguishable polymer chains, each having a contour length L and a bare persistence length λ. The polymer consists of two segments, A and B; the segment fractions of the A and B blocks are f and $1-f$, respectively. The persistence length λ is assumed to be the same in both A and B segments, although the theoretical framework below can also be adopted for two segments having different persistence lengths [25, 58, 107]. The joint point between A and B segments continuously connects the two segments with the same persistency. In this section, we briefly outline the procedure that leads to the formalism in a self-consistent field theory. Detailed derivations can be found in standard references [41, 39].

The chains are labeled from $k = 1$ to $k = n$. The configuration of the kth chain is described by a space curve $\mathbf{R}_k(s)$, where s is an arc-variable along the curve which continuously varies from one end ($s = 0$) to the other ($s = 1$). According to the Saito-Takahashi-Yunoki curvature model [100], the configurational energy of the entire system can be written as

$$\mathcal{H}_0 = \frac{\lambda}{2L} \sum_{k=1}^{n} \int_0^1 \mathrm{d}s \left| \frac{\mathrm{d}\mathbf{u}_k(s)}{\mathrm{d}s} \right|^2, \tag{3.1}$$

where the tangent vector $\mathbf{u}_k(s) \equiv (1/L)\mathrm{d}\mathbf{R}_k(s)/\mathrm{d}s$ specifies the local orientation of the kth polymer chain at location s. We treat $\mathbf{u}_k(s)$ as a unit vector in this work.

The energy penalty of mixing A and B segments is assumed to have a typical Flory-Huggins form,

$$\mathcal{H}_1 = \chi\rho_0 \int \mathrm{d}\mathbf{r}\hat{\phi}_A(\mathbf{r})\hat{\phi}_B(\mathbf{r}) \tag{3.2}$$

where $1/\rho_0$ represents the volume occupied by one segment and χ is the Flory-Huggins coefficient [38]. The density operators for components A and B are respectively defined as

$$\hat{\phi}_A(\mathbf{r}) \equiv \frac{L}{a\rho_0}\sum_{k=1}^{n}\int_0^f \mathrm{d}s\delta(\mathbf{r}-\mathbf{R}_k(s)), \tag{3.3}$$

$$\hat{\phi}_B(\mathbf{r}) \equiv \frac{L}{a\rho_0}\sum_{k=1}^{n}\int_f^1 \mathrm{d}s\delta(\mathbf{r}-\mathbf{R}_k(s)), \tag{3.4}$$

where a represents the Kuhn length and is related to the bare persistence length λ by

$$a \equiv 2\lambda. \tag{3.5}$$

The identification can be made by examining the mean-square end-to-end distance of a long wormlike chain in the limit of $L \gg \lambda$ [100]. In the remaining part of this paper, a is directly used instead of λ for the convenience of comparing the results from the current model to those based on the Gaussian-chain (GSC) model [41].

Furthermore we assume that the system is incompressible. The partition function of the system can then be written as,

$$Z = \frac{1}{n!}\int D\mathbf{R}\exp\bigl(-\mathcal{H}_0-\mathcal{H}_1\bigr)\prod_{\mathbf{r}}\delta\Bigl[1-\hat{\phi}_A(\mathbf{r})-\hat{\phi}_B(\mathbf{r})\Bigr], \tag{3.6}$$

where the delta function deals with the incompressibility condition.

In order to obtain the Helmholtz free energy for the system, nF, one takes a Hubbard-Stratonovich transformation, which is a general approach in particle-to-field transformation [39]. Finally we can write the mean-field Helmholtz free energy

per chain, F, as

$$\beta F = -\ln Q + \frac{1}{V}\int \mathrm{d}\mathbf{r}\Big[(\chi L/a)\phi_A(\mathbf{r})\phi_B(\mathbf{r}) - w_A(\mathbf{r})\phi_A(\mathbf{r}) - w_B(\mathbf{r})\phi_B(\mathbf{r}) + \xi(\mathbf{r})(\phi_A(\mathbf{r}) + \phi_B(\mathbf{r}) - 1)\Big]. \quad (3.7)$$

which is a functional of the mean fields $w_A(\mathbf{r})$ and $w_B(\mathbf{r})$ that the components A and B experience, the mean volume fractions $\phi_A(\mathbf{r})$ and $\phi_B(\mathbf{r})$ at coordinate $\mathbf{r}$, and a Lagrangian multiplier $\xi(\mathbf{r})$ which enforces the incompressibility constraint on the system. The prefactor $\beta = 1/k_BT$, where T is the temperature of the system and k_B the Boltzmann constant. The single chain partition function Q is calculated from

$$Q = \frac{1}{4\pi V}\int \mathrm{d}\mathbf{r}\mathrm{d}\mathbf{u}q(\mathbf{r},\mathbf{u},1). \quad (3.8)$$

The propagator $q(\mathbf{r},\mathbf{u},s)$, the main focus in a the self-consistent field treatment, represents the probability at the spatial position $\mathbf{r}$ and at point in a direction specified by the unit vector $\mathbf{u}$ of finding the terminal labeled as s originating at another terminal labeled as 0. In an external field $w(\mathbf{r},s)$, the propagator can be obtained from solving the modified diffusion equation (MDE) [41, 39]

$$\frac{\partial}{\partial s}q(\mathbf{r},\mathbf{u},s) = \left[\frac{L}{a}\nabla^2_{\mathbf{u}} - L\mathbf{u}\cdot\nabla_{\mathbf{r}} - w(\mathbf{r},s)\right]q(\mathbf{r},\mathbf{u},s), \quad (3.9)$$

subject to the initial condition $q(\mathbf{r},\mathbf{u},0) = 1$. For the current system,

$$w(\mathbf{r},s) = \begin{cases} w_A(\mathbf{r}) = w_+(\mathbf{r}) - w_-(\mathbf{r}), & \text{if } 0 \le s \le f \\ w_B(\mathbf{r}) = w_+(\mathbf{r}) + w_-(\mathbf{r}), & \text{if } f < s \le 1. \end{cases}$$

Here, $w_-(\mathbf{r})$ represents the exchange chemical potential conjugate to local concentration difference and $w_+(\mathbf{r})$ enforces the incompressible constraint on the system [40].

Complementary to $q(\mathbf{r},\mathbf{u},s)$ is the propagator $q^*(\mathbf{r},\mathbf{u},s)$, which represents the probability at the spatial position $\mathbf{r}$ and at a point in a direction specified by the unit vector $-\mathbf{u}$ of finding the terminal labeled as s originating at another terminal labeled as 1. It satisfies a similar MDE

$$\frac{\partial}{\partial s}q^*(\mathbf{r},\mathbf{u},s) = \left[-\frac{L}{a}\nabla^2_{\mathbf{u}} - L\mathbf{u}\cdot\nabla_{\mathbf{r}} + w(\mathbf{r},s)\right]q^*(\mathbf{r},\mathbf{u},s), \quad (3.10)$$

and is subject to the initial condition $q^*(\mathbf{r}, \mathbf{u}, 1) = 1$.

Minimization of the free energy functional in Eq. (3.7) with respect to the functions ϕ_A, ϕ_B, ξ, w_A and w_B yields further relations between these functions. They include,

$$w_A(\mathbf{r}) = (\chi L/a)\phi_B(\mathbf{r}) + \xi(\mathbf{r}), \tag{3.11}$$

$$w_B(\mathbf{r}) = (\chi L/a)\phi_A(\mathbf{r}) + \xi(\mathbf{r}), \tag{3.12}$$

$$\phi_A(\mathbf{r}) + \phi_B(\mathbf{r}) = 1, \tag{3.13}$$

$$\phi_A(\mathbf{r}) = \frac{1}{4\pi Q} \int \mathrm{d}\mathbf{u} \int_0^f \mathrm{d}s q(\mathbf{r}, \mathbf{u}, s) q^*(\mathbf{r}, \mathbf{u}, s), \tag{3.14}$$

and

$$\phi_B(\mathbf{r}) = \frac{1}{4\pi Q} \int \mathrm{d}\mathbf{u} \int_f^1 \mathrm{d}s q(\mathbf{r}, \mathbf{u}, s) q^*(\mathbf{r}, \mathbf{u}, s). \tag{3.15}$$

The main task then becomes solving Eqs. (3.9)-(3.15) self-consistently for the functions ϕ_A, ϕ_B, ξ, w_A and w_B. The solution may contain multiple structures, depending on the parameter set, f, L/a, and $\chi L/a$. Together with the definition in Eq. (3.8), the free energy F can then be evaluated according to Eq. (3.7), which is used for determination of the stability of a particular structure.

3.3 Disordered-lamellar phase transition

In this section, we focus on solving such a model to determine the stability boundary and phase behavior between a disordered phase, where A- and B- components are well mixed, and a lamellar phase, where the structure breaks up into A-rich and B-rich domains in a layered form (Fig. 3.1). While we consider the full f-dependence, at $f = 1/2$ our results agree well with the simplest case of symmetric AB diblock copolymers recently studied by Matsen [76]. The order-disorder phase separation of a wormlike AB diblock copolymer was also theoretically considered by Singh et al. [105] and Friedel et al. [43] , who have developed somewhat different theoretical tools for these systems.

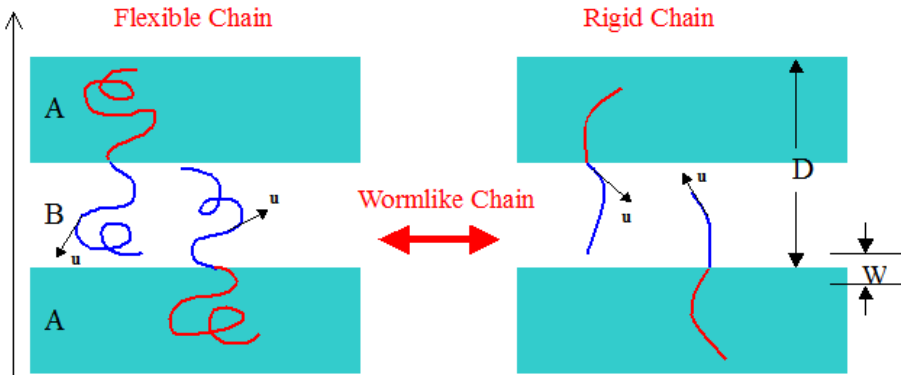

Figure 3.1: Sketches of a lamellar morphology for the AB diblock copolymers: on the left-hand side, flexible polymers that can be described by the Gaussian-chain formalism and the long-chain limit of the current wormlike-chain formalism, and on the right-hand side, the rigid-chain limit that is also covered in this work. The wormlike-chain formalism leads to a smooth crossover between these two limits.

3.3.1 Numerical approach

The computational strategy used in this work depends on iterations that correct a previous estimate. Initially, an approximation for the external fields $w_-(\mathbf{r})$ and $w_+(\mathbf{r})$ is made which can be used to obtain $q(\mathbf{r},\mathbf{u},s)$ and $q^*(\mathbf{r},\mathbf{u},s)$ through solving Eqs. 3.9 and 3.10 numerically for the entire $0 \leq s \leq 1$ range. Then, the density profiles for components A and B can be computed straightforwardly from Eqs. 3.14 and 3.15. As a naive approach the next step would be to calculate an improved approximation for the external fields by directly requiring that Eqs. 3.11 - 3.13 are satisfied. However, this step is not always numerically stable hence is not used in the actually numerical implementation. Following the work done by Fredrickson et al. [40], instead of taking Eqs. 3.11 - 3.13 in their original forms, we used the effective relaxation equations

$$\frac{\partial}{\partial t} w_-(\mathbf{r},t) = -\xi_- \left\{ \phi_B(\mathbf{r},t) - \phi_A(\mathbf{r},t) + \left[\frac{2}{(\chi L/a)} w_-(\mathbf{r},t) + (2f-1) \right] \right\}, \quad (3.16)$$

$$\frac{\partial}{\partial t} w_+(\mathbf{r},t) = \xi_+ \left[\phi_A(\mathbf{r},t) + \phi_B(\mathbf{r},t) - 1 \right], \quad (3.17)$$

in a forward-difference scheme for t with a step length Δt. The coefficients $\Delta t\xi_-$ and $\Delta t\xi_+$ control the relaxation rate of the convergence in solving Eqs. 3.16 and 3.17. Large relaxation coefficients yield a faster search for the equilibrium solution, but are also accompanied by an undesirable instability. We found in our calculation that for the current system an appropriate range is $0.2 \leq \Delta t\xi_-, \Delta t\xi_+ \leq 0.6$. The fields $w_-(\mathbf{r},t)$ and $w_+(\mathbf{r},t)$, which are calculated from the relaxation method, update once after a full calculation of q and q^* is done; then they are used as a new guess in Eqs. 3.9 and 3.10 for the starting point of a new iteration.

Within this computational strategy, a crucial step is accurately and efficiently carrying out the solution to Eqs. 3.9 and 3.10. Formally, an exact expression can be obtained for Eq. 3.9,

$$q(\mathbf{r},\mathbf{u},s+\Delta s) = \exp\left[\Delta s\left(\mathcal{L}^{\nabla^2_{\mathbf{u}}} + \mathcal{L}^{\nabla_{\mathbf{r}}} + \mathcal{L}^{\omega}\right)\right] q(\mathbf{r},\mathbf{u},s), \tag{3.18}$$

which is valid for any size of Δs. The three operators appearing in the above expression are $\mathcal{L}^{\nabla^2_{\mathbf{u}}} \equiv (L/a)\nabla^2_{\mathbf{u}}$, $\mathcal{L}^{\nabla_{\mathbf{r}}} \equiv -L\mathbf{u}\cdot\nabla_{\mathbf{r}}$, and $\mathcal{L}^{w} \equiv -w(\mathbf{r})$. Performing the Baker-Campbell-Hausdorff operator identity twice [97],

$$\begin{aligned} e^{\Delta s\mathcal{L}^{w}} e^{\Delta s\mathcal{L}^{\nabla_{\mathbf{r}}}} e^{\Delta s\mathcal{L}^{\nabla^2_{\mathbf{u}}}} = \exp\Bigg\{ & \Delta s\left(\mathcal{L}^{w} + \mathcal{L}^{\nabla_{\mathbf{r}}} + \mathcal{L}^{\nabla^2_{\mathbf{u}}}\right) \\ & + \frac{\Delta s^2}{2}\left(\left[\mathcal{L}^{w},\mathcal{L}^{\nabla_{\mathbf{r}}}\right] + \left[\mathcal{L}^{w},\mathcal{L}^{\nabla^2_{\mathbf{u}}}\right] + \left[\mathcal{L}^{\nabla_{\mathbf{r}}},\mathcal{L}^{\nabla^2_{\mathbf{u}}}\right]\right) + \mathcal{O}(\Delta s^3)\Bigg\}, \end{aligned} \tag{3.19}$$

where $\left[\mathcal{L}^{w},\mathcal{L}^{\nabla_{\mathbf{r}}}\right] \equiv \mathcal{L}^{w}\mathcal{L}^{\nabla_{\mathbf{r}}} - \mathcal{L}^{\nabla_{\mathbf{r}}}\mathcal{L}^{w}$ represents the operator commutator, we can obtain the solution to the propagator

$$q(\mathbf{r},\mathbf{u},s+\Delta s) = e^{\Delta s\mathcal{L}^{w}/2} e^{\Delta s\mathcal{L}^{\nabla_{\mathbf{r}}}/2} e^{\Delta s\mathcal{L}^{\nabla^2_{\mathbf{u}}}} e^{\Delta s\mathcal{L}^{\nabla_{\mathbf{r}}}/2} e^{\Delta s\mathcal{L}^{w}/2} q(\mathbf{r},\mathbf{u},s) + \mathcal{O}(\Delta s^3). \tag{3.20}$$

The advantage of using the above is that for a small Δs, terms of the order Δs^2 exactly cancel out and the error only amounts to an order of Δs^3 and higher. This can be compared with the Crank-Nicolson method which is commonly used in solving modified diffusion equations such as those in our previous works [27, 61], where a numerical error of the order Δs^2 is introduced [93]. We also note that some forward-difference based algorithms were previously used for the calculation of the propagator [103, 107].

To apply this method further, we need to deal with the $\mathcal{L}$ operators. The spherical harmonics and Fourier bases are the eigenfunctions of the operators $\mathcal{L}^{\nabla^2_{\mathbf{u}}}$ and $\mathcal{L}^{\nabla_{\mathbf{r}}}$, respectively. As long as the transformations connecting the variables $\mathbf{u}$ and $\mathbf{r}$ and the expansion coefficients of spherical harmonics and Fourier functions are provided, the split-step algorithm is efficient for carrying out the calculations associated with the exponential operations [36, 37]; the method is known to be unconditionally stable and highly accurate, which means that fewer expansion coefficients and a relatively large step length Δs can be taken in the actual calculation. A similar algorithm was constructed by Tzeremes et al. [113] to solve the modified diffusion equation deduced from a Gaussian chain model previously. This approach has multiple advantages over a finite-difference scheme, which requires a more careful division of the variable space to match the correct order in Δs, in order to avoid numerical divergence.

In the present work, we only restrict our study to a lamellar phase, where only one spatial variable x and one orientational variable θ (between the axis x and orientational vector $\mathbf{u}$ shown in Fig. 3.1) are considered, although such a dimension reduction is not constrained compulsively in the current method. In principle, we can explore any complex ordered phase such as the well-known gyroid, hexagonal, spherical, etc. through changing the volume fraction of any component of diblock copolymers on the basis of our proposed numerical scheme. But, it is almost impossible in practice due to overlarge 6 dimensional (3 spatial + 2 orientational + 1 diffusion like) variables in Eq. 3.9 and 3.10. The study on the complicated full 3D morphologies will be discussed in section 3.4 by virtue of an efficient numerical algorithm, which has a better performance in treatment of Eq. 3.9 and 3.10 than the split-step approach mentioned here.

For a function of x and the associated Fourier transformation k, we can define the Fourier transform $\hat{F}$ and the inverse Fourier transform $\hat{F}^{-1}$. For a function of θ and its Legendre function of rank l, we can define the Legendre transform $\hat{S}$ and

the synthesis of Legendre transform $\hat{S}^{-1}$. We can then write

$$q(x,\theta,s+\Delta s) \approx e^{-\Delta s w_j(x)/2}\hat{F}^{-1}\Big\{e^{-i\Delta sk\cos\theta/2}\hat{F}\Big[\hat{S}^{-1}\Big(e^{-\Delta s(L/a)l(l+1)} \times \hat{S}\Big\{\hat{F}^{-1}\Big[e^{-i\Delta sk\cos\theta/2}\hat{F}\Big(e^{-\Delta s w_j(x)/2}q(x,\theta,s)\Big)\Big]\Big\}\Big)\Big]\Big\}. \quad (3.21)$$

The Fourier bases used for the lamellar phase can be characterized by a discrete set

$$k_m = 2\pi m/D \quad (3.22)$$

where m is an integer and D is the lamellar domain size considered in Fig. 3.1. The same resolution for x as the one used by Matsen [76] was adopted in this work. In practice, these transformations are performed based on well-established numerical procedures such as those given in *Numerical Recipes in C* [93]. The truncated expansion index l and the corresponding number of the equally divided grids on polar angle θ are appropriately adjusted according to the convergence criteria $\mathrm{MAX}|w_{\pm}^{new}(x) - w_{\pm}^{old}(x)| < 10^{-4}$. In this way the free energy produced depends on the domain size D; an additional computational task is to search for the minimum free energy as a function of D [7]. The results reported below correspond to an optimal D after such minimization.

3.3.2 Results and discussion

We consider the influence of the chain persistency on the physical properties from the disorder-lamellar stability analysis. As discussed in the introduction and shown exactly in the last section, three independent parameters emerge to be important: the scaled Flory-Huggins interaction parameter $\chi L/a$, the volume fraction of the A component f, and the effective number of Kuhn segments in a wormlike chain L/a. Note that f and $\chi L/a$ are the same combination of parameters as in the Gaussian-chain theory for the lamellar phase; in the latter case the parameter L/a is normally related to the number of monomers in a typical theory and is taken to be a large number [39].

In particular, we discuss below the numerical results from our self-consistent field theory in terms of a stability diagram where the disorder-lamellar (DL) boundary

divides the stability regions of the disorder and lamellar states, determined from an examination of the free energy, $F = F(f, L/a, \chi L/a)$. We also discuss the properties of the lamellar domain size, $D/a \equiv \tilde{D}(f, L/a, \chi L/a)$, which was optimized to minimize the lamellar free energy per domain. We further discuss an interfacial width,

$$W = \left[\mathrm{MAX} \left| \frac{\mathrm{d}}{\mathrm{d}x} \phi_A(x) \right| \right]^{-1}, \tag{3.23}$$

where the function MAX takes the maximum value of its argument. The rescaled interfacial width $W/a \equiv \bar{W}(f, L/a, \chi L/a)$ is a function of f, L/a, and $\chi L/a$ as well.

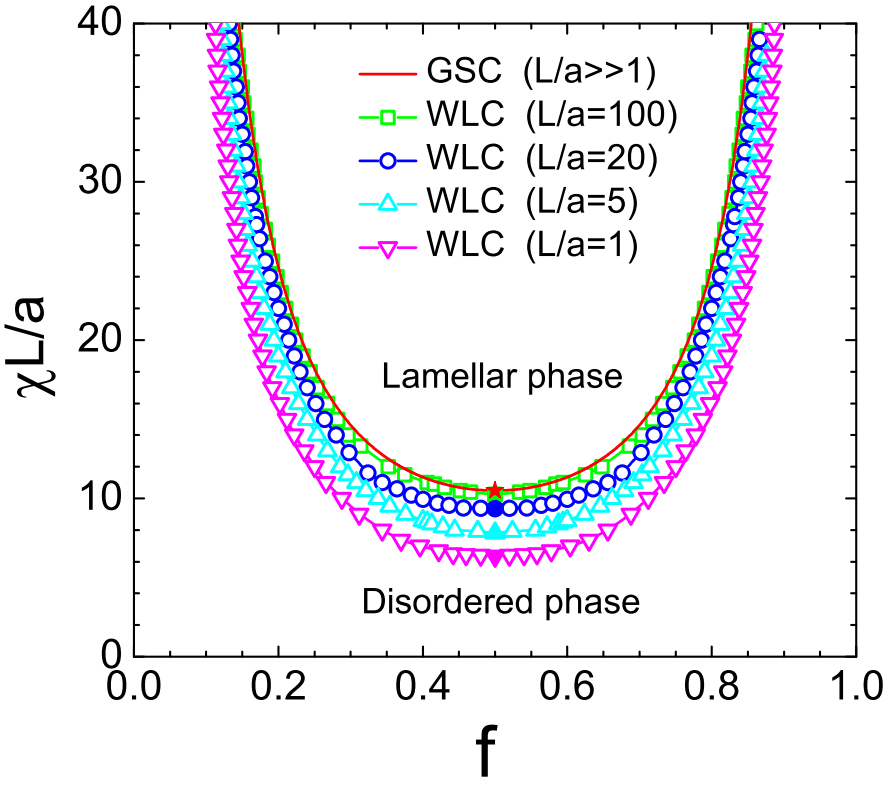

Figure 3.2: Numerical results for the disorder-lamellar stability boundary based on a wormlike-chain (WLC) model for AB diblock copolymers for several selected values of L/a: $100, 20, 5$ and 1, represented by squares, circles, up triangles and down triangles, respectively. These new results can be compared to the stability boundary obtained from calculation based on a random phase approximation of a Gaussian-chain (GSC) model, which is shown by the solid curve. All boundaries have the characteristics of a first-order phase transition, terminating at a second-order point represented by the filled points at $f = 1/2$.

The flexible limit: $L/a \gg 1$

Our first concern is whether the DL stability boundary determined by the current wormlike-chain (WLC) model would recover what we have already known from the classical random phase approximation (RPA) [71] of a Gaussian-chain model in the limit of $L/a \gg 1$. As shown in Fig. 3.2, the DL boundaries (represented by symbols) determined from the WLC model for various values of L/a have a reasonable trend to asymptotically approach the solid curve, which was obtained from a weak-inhomogeneity expansion based on the assumption of Gaussian-type statistical weight of a polymer configuration [71]; the $L/a = 100$ curve (squares in Fig. 3.2) from our calculation even overlaps with the RPA result substantially.

In many wormlike-chain systems, the recovery of the Gaussian-chain result is *not* a trivial notion even in the limit of $L/a \gg 1$ and needs to be carefully justified; the magnitude of a/W, where W characterizes a typical length scale on which the density profile varies drastically, determines whether or not the Gaussian-chain limit is approached [11, 28]. In the current model, the spatial variation of the density profile is reflected in the main equations, Eqs. 3.9 and 3.10, by the derivative term, $L\mathbf{u} \cdot \nabla_{\mathbf{r}} = (L/a)(a/W)\cos\theta d/d\bar{x}$ where $\bar{x} \equiv x/W$. While the L/a prefactor is comparable to the magnitude of the first term in Eqs. 3.9 and 3.10, the magnitude of a/W is responsible for whether or not a Gaussian-weight based SCFT can be recovered from a WLC based SCFT; indeed, taking a simultaneous expansion of the propagator in terms of the Legendre functions and powers of small a/W, we can show that in the lamellar phase,

$$\chi \sim (a/W)^2,$$

and that Eqs. 3.9 and 3.10 exactly recover the counterpart diffusion equation in a Gaussian theory for $L/a \gg 1$ [101].

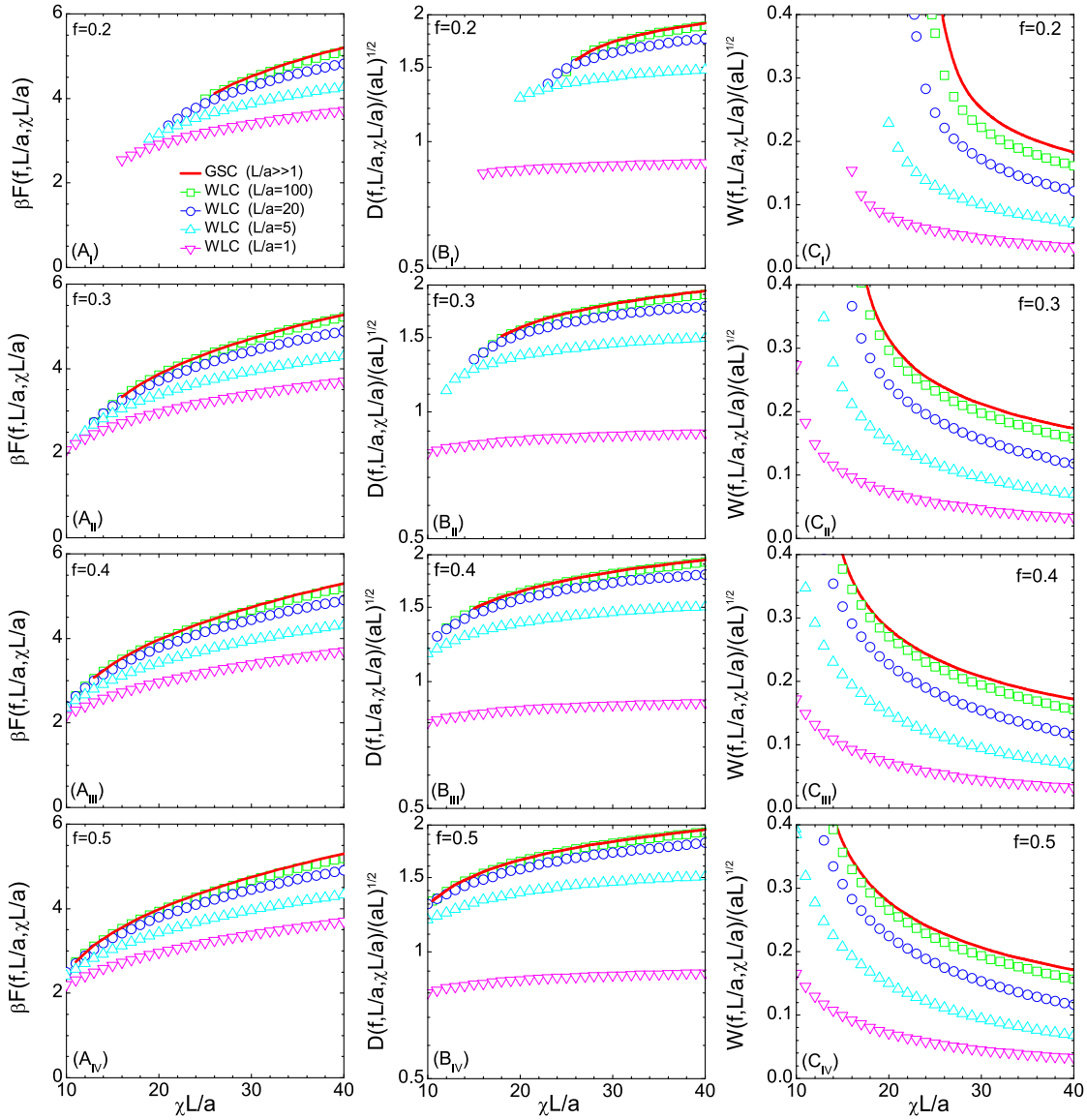

Figure 3.3: (A) Lamellar free energy $F(f, L/a, \chi L/a)$, (B) reduced domain size $D(f, L/a, \chi L/a)/(aL)^{1/2}$ and (C) reduced interfacial width $W(f, L/a, \chi L/a)/(aL)^{1/2}$ as a function of the reduced Flory-Huggins parameter $\chi L/a$ for volume fraction (I) $f = 0.2$, (II) $f = 0.3$, (III) $f = 0.4$, and (IV) $f = 0.5$, computed from the wormlike-chain formalism. In these plots, chain sizes $L/a = 100, 20, 5$ and 1 are represented by squares, circles, up triangles and down triangles, respectively. The results from a Gaussian-chain (GSC) formalism, valid for $L/a \gg 1$, are also plotted as the solid curves.

This can be interpreted in a physical picture. In the flexible polymer limit, $L/a \gg 1$, each wormlike-like polymer approximately has the size of the Gaussian gyration radius in a disordered phase, $(aL)^{1/2}$. Approaching the DL instability boundary from the disordered side, once the phase separation takes place in the form of a continuous or weak first-order transition, both the domain size D and interfacial width W are on the order of $(aL)^{1/2}$. It guarantees that the ratio a/W is approximately $a/W \sim (a/L)^{1/2}$ which is small in the limit of $a/L \ll 1$. For comparison, because $\chi L/a$ represents the immiscibility interaction between polymer segments A and B, we expect that phase separation takes place when $\chi L/a \sim 1$, or $\chi \sim a/L$; hence the estimate $\chi \sim (a/W)^2$ is physically justifiable.

Numerically, Fig. 3.3 (B) and Fig. 3.3 (C) demonstrate how both $D/(aL)^{1/2}$ and $W/(aL)^{1/2}$ in the lamellar state approach a L/a-independent limit as L/a increases, results from a wormlike polymer based SCFT.

Because the DL stability boundary is determined from the free energy, the approaching of the asymptotic GSC result in Fig. 3.2 is the direct consequence of the asymptotic behavior of the free energy, displayed in Fig. 3.3 (A). For a specified value of f and $\chi L/a$, as the function of L/a, a L/a-independent asymptotic limit can be viewed in these plots when $L/a \gg 1$.

Within a GSC model, Leibler showed that the DL stability boundary has the characteristics of a second-order phase transition at $f = 0.5$ and a first-order phase transition for $f \neq 0.5$ [71]. These properties can be directly examined in terms of the lamellar free energy difference $\Delta F = F - F_0$ where F_0 is the free energy of the disordered phase, and the inverse scaled interfacial width $(aL)^{1/2}/W$ as an order parameter which has a value of $(aL)^{1/2}/W = 0$ in the disordered phase. As a function of $(\chi - \chi_{\mathrm{DL}})L/a$ for a given value of f, where χ_{DL} is the value at the DL transition boundary, ΔF is negative inside the lamellar region and displays a quadratic behavior near the transition point for $f = 0.5$ and a straight line near the transition point for $f \neq 0.5$, according to the mean-field understanding of the phase transition theory. The solid curve in the upper panel of Fig. 3.4 (A) and the solid line in the upper panel of Fig. 3.5 (A) are examples of this critical behavior. As the function of the same variable, for $f = 1/2$ where the transition is second-order, the order parameter in the lamellar phase is expected to display a power law with

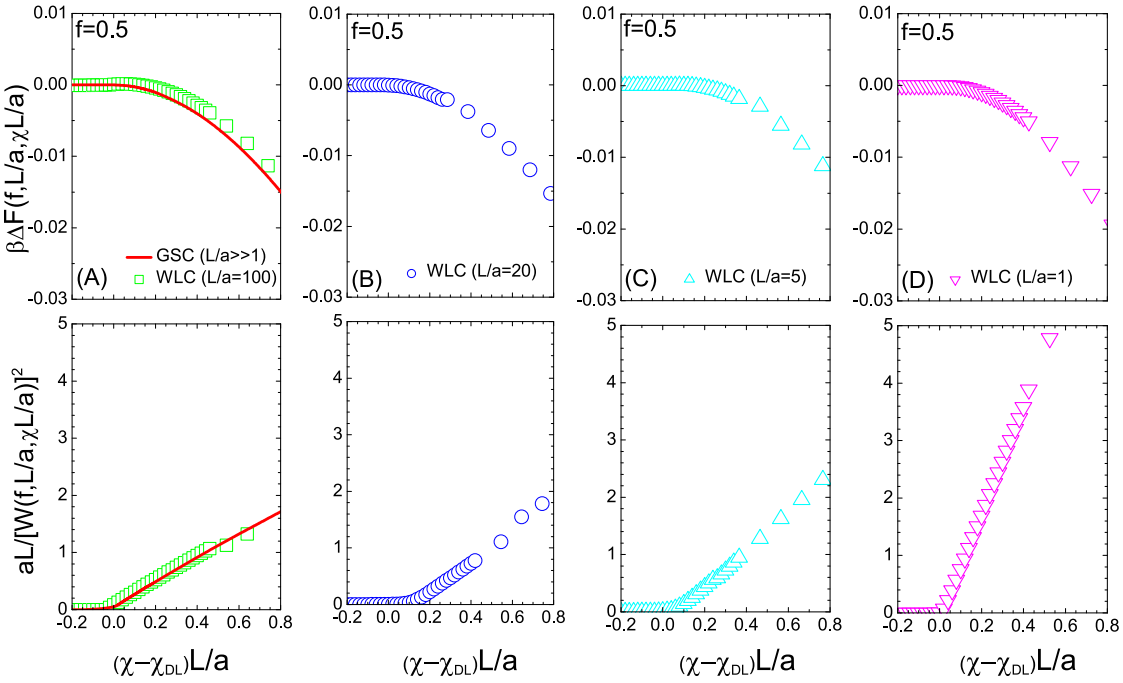

Figure 3.4: Symmetric AB diblock copolymers ($f = 1/2$): numerical results for the lamellar free-energy difference (upper panels) and square order parameter (lower panels) as functions of $\chi - \chi_{\rm DL})L/a$ where $\chi_{\rm DL}L/a$ is the critical point specified by a filled symbol in Fig. 2. We consider the properties for a Gaussian-chain (GSC) model for $L/a \gg 1$ [solid curve in (A)] and a wormlike-chain (WLC) model for $L/a = 100$ (squares), 20 (circles), 5 (up triangles) and 1 (down triangles).

an critical exponent 1/2 hence the square order parameter showing a straight line (solid line in the lower panel of Fig. 3.4 (A); for $f \neq 1/2$ where the transition is first-order, the order parameter abruptly jumps to zero, when the system goes through the transition point from the lamellar phase (solid line in the lower panel of Fig. 3.5 (A)). The long-chain results yielded from the WLC model, displayed in these plots by squares for $L/a = 100$, fully agree with these characteristics near the transitions.

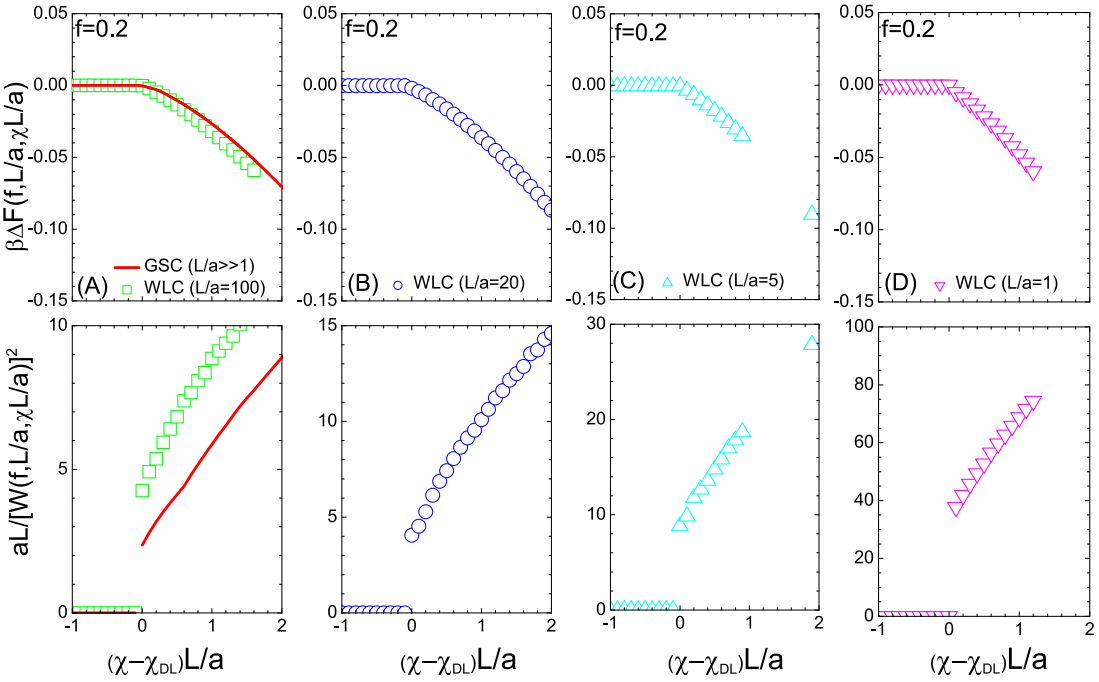

Figure 3.5: An example of asymmetric AB diblock copolymers ($f = 0.2$): numerical results for the lamellar free-energy difference (upper panels) and square order parameter (lower panels) as functions of $\chi - \chi_{\rm DL})L/a$ where $\chi_{\rm DL}L/a$ is the first-order transition point. We consider the properties for a Gaussian-chain (GSC) model for $L/a \gg 1$ [solid curve in (A)] and a wormlike-chain (WLC) model for $L/a = 100$ (squares), 20 (circles), 5 (up triangles) and 1 (down triangles).

Intermediate region: $L/a \sim 1$

Moving away from the extremely large L/a region, we start to see the effects of persistency in the stability diagram, Fig. 3.2. For L/a as large as $L/a = 20$, the stability boundary already moves significantly below the GSC result. The DL stability boundaries deviate even more remarkably from the RPA result in the smaller $L/a = 5$ and 1 cases. According to this diagram, we conclude that one of the main effects of the chain persistency is broadening of the lamellar stability region accompanied by a lower transition $\chi_{\rm DL}L/a$. Physically, a more rigid polymer chain looses less conformational entropy in a stretched conformation in comparison with its Gaussian counterpart of the same length. One consequence in our system is

that persistency makes it easier for the system to phase-separate (which decreases a polymer's entropy) for the same value of the $\chi L/a$ parameter. This is the underlying reason of the broadening for the lamellar stability region in Fig. 3.2, similar to the observation by another research group [43].

Going from the flexible chain limit (large L/a) to a more rigid molecule (small L/a), the typical domain size of the lamellar state crosses over from $D \sim (aL)^{1/2}$ (Gaussian-coil size) to $D \sim L$ (rod size); similarly this happens to a typical interface width which crosses over from $W \sim (aL)^{1/2}$ to $W \sim L$ as well. In the intermediate region, we expect to see that both D and W deviate significantly from these asymptotic behaviors. The crossover can be viewed from the numerical examples shown in Fig. 3.6 where we see that both D/a and W/a scale as $(L/a)^{1/2}$ in the large L/a limit and as L/a in the small L/a limit.

From a phase transition perspective, the phase boundary at $f = 1/2$ is second-order according to the GSC model [71]; this second-order nature is re-assured by our calculation of the WLC model, now valid for any ratio of L/a, even in the small L/a region. The numerical evidence can be found in four plots ($L/a = 100, 20, 5$ and 1) of Fig. 3.4 where the order parameter $(aL)^{1/2}/W$ can be seen to always vary continuously across the transition point $\chi_{\rm DL}$. In all these cases, our data also demonstrate that a mean-field critical exponent of 1/2 is followed by the order parameter in a lamellar phase near the transition point (hence an exponent of 1 for the square order parameter in the figure). Furthermore in the upper panels of these plots, the lamellar free energy difference can be seen to connect to $\Delta F = 0$ in the disordered phase by a smoothly varying slope.

Fig. 3.5 shows the free energy difference and order parameter for an asymmetric case $f = 0.2$, which demonstrates a different behavior. The order parameter $(aL)^{1/2}/W$ goes through a finite jump and the free energy difference displays a straight line approaching the transition point $\chi_{\rm DL}$ from the lamellar phase. These are characteristics of a first-order transition, valid for all other values of f (as long as $f \neq 1/2$) as well (figures not shown). The first-order jump in the order parameter weakens and finally vanishes as f approaches 1/2. That is, along all DL stability boundaries described in Fig. 3.2, only symmetric WLC AB diblock copolymers ($f = 1/2$) have a second-order transition (shown by filled symbols in the figure).

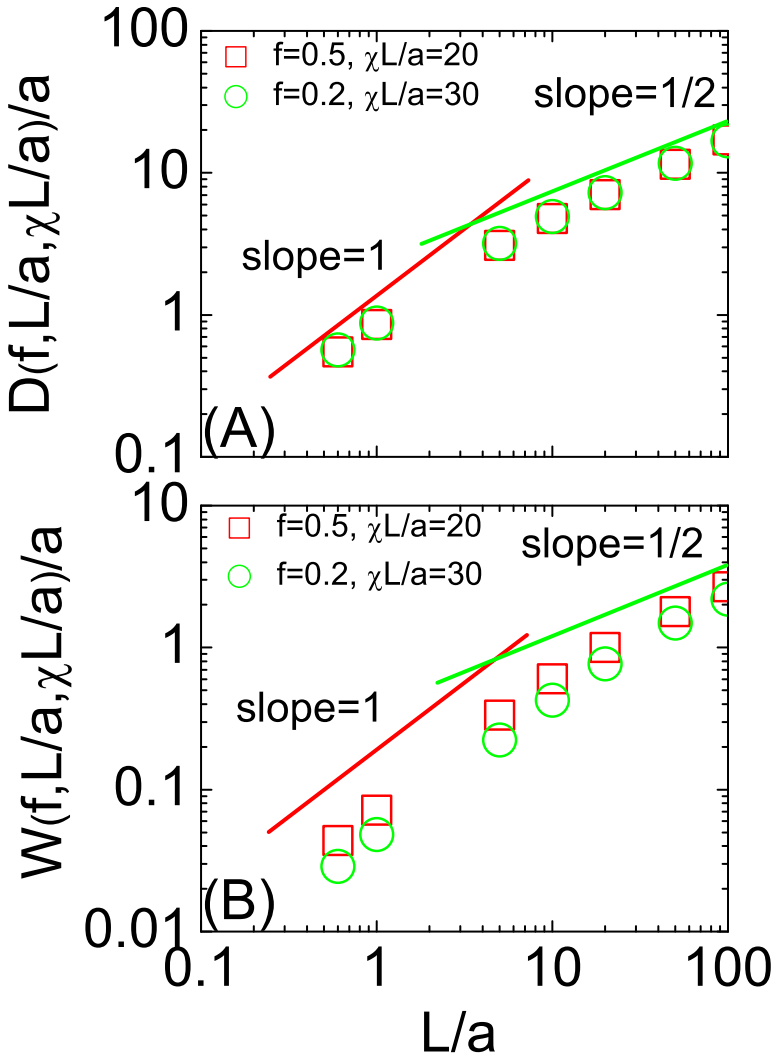

Figure 3.6: Logarithmic plots of (A) reduced domain size $D(f, L/a, \chi L/a)/a$ and (B) interfacial width $W(f, L/a, \chi L/a)/a$ as functions of chain length L/a. Squares and circles represent systems with fixed parameters $(f = 0.5, \chi L/a = 20)$ and $(f = 0.2, \chi L/a = 30)$, respectively. Asymptotic power laws at large and small L/a are indicated by slopes $1/2$ and 1, respectively.

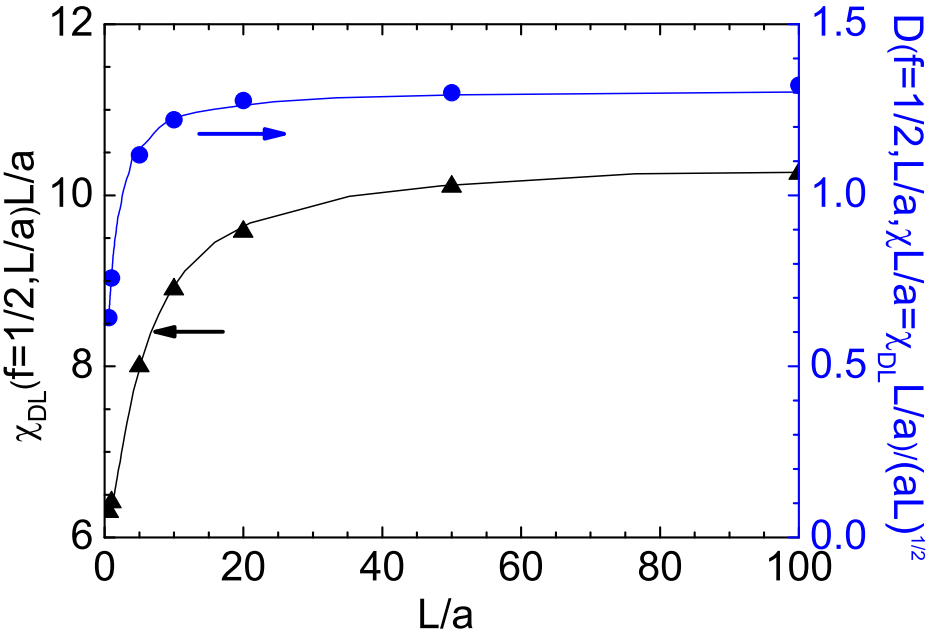

Figure 3.7: Disordered-lamellar stability boundary $\chi_{\rm DL}(f = 1/2, L/a)L/a$ and the corresponding reduced domain size $D(f = 1/2, L/a, \chi_{\rm DL}L/a)/(aL)^{1/2}$ as functions of the chain rigidity parameter L/a, determined from a wormlike-chain formalism. The triangles and circles represent our numerical results for $\chi_{\rm DL}$ and $D_{\rm DL}$, respectively. The solid curves are replotted by using data read off from Fig. 1 of Matsen's work, for comparison [76].

Remarks

For the case of $f = 1/2$ (symmetric lamellar morphology), our WLC results are in full agreement with those considered by Matsen, after making the identification of his κ with 1/2 [76]. In Fig. 3.7, using solid curves we replotted Matsen's DL stability boundary $\chi_{\rm DL}(f = 1/2, L/a)L/a$ and lamellar domain size $D(f = 1/2, L/a, \chi_{DL}L/a)/(aL)^{1/2}$ by reading off data from the figures of his publication. Overlapping on top of the curves are our results for various values of L/a. One interesting limit is $L/a \to 0$, the limit of rigid rod chain. From our data in the figure we see that $\chi_{\rm DL}(f = 1/2, L/a)L/a$ asymptotically approaches 6.18 ± 0.02,

which agrees with Matsen's estimate of 6.135 [76] within numerical error; however, both are far lower than the value of 8.30 suggested by Singh et al. [105] and 7.55 by Friedel et al. [43].

The WLC stability diagram presented in Fig. 3.2 is based on the comparison of the free energy of two possible states occurring in a AB diblock copolymer system: disordered and lamellar. We use this example to demonstrate the importance of the influence of chain persistency in determining the free energy and hence the phase diagram of AB diblock copolymers. Extrapolating to other phases existing in this system, we believe that the classic diblock copolymer phase diagram [79, 20] previously predicted by a GSC model must be significantly revised after the chain rigidity is introduced. This is particularly so for the bcc (body-centred cubic) stable region [79, 20] where $\chi L/a$ is large and the interface width is sharp. Because of computational limitations, we considered the stability of the lamellar phase only in this work, using a one-dimensional spatial variation; future work that explores full three-dimensional spatial mesostructures is needed to complete the WLC AB diblock copolymer phase diagram and is more demanding in numerical computation.

Finally, we wish to mention that there are two basic assumptions taken in the study of WLC AB diblock copolymers: the incompressibility condition, Eq. 3.13, and the Flory-Huggins interaction, Eq. 3.2. These two assumptions are identical to those used in studying AB diblock copolymers based on a Gaussian-chain description, where these assumptions can be made by coarse graining over a volume scale of a^3. One important property of a wormlike chain is associated with the angular distribution of a chain segment; strictly speaking, we must include the orientation dependence, beyond the position-dependence, in both Eqs. 3.2 and 3.13. A proper procedure of handling the orientation dependence of the incompressibility condition and the Flory-Huggins interaction is desirable and currently unavailable for WLC; the development of such a theory may need the inclusion of a solvent component in the model. Nevertheless, most current researches in understanding WLC AB diblock copolymers adopt these two assumptions [82, 74, 76].

3.4 Phase boundaries for complex morphologies

The split-step algorithm presented above amounts to an error corresponding to third order in the steplength of the timelike variable with no restriction on the precision of representing the orientational and spatial variables. This can be compared with the Crank-Nicolson [93] method used previously, which contains a numerical error of second order in the steplength of the timelike variable and has a concurrent requirement on the precision of the orientational and spatial variables. As well, a direct forward time-difference scheme would introduce an error of the same order as the steplength in the time-variable hence requires very small divisions [25, 107]. Fredrickson [39] has estimated that a typical split-step algorithm for solving the MDE amounts to an order of $O(NKM^{3/2}\log_2 M)$ computational operations, where N, K, M denote the number of contour steps, the number of spectral collocation points and number of spherical harmonics, respectively, used in the treatment. Once it was considered as an excellent scheme to solve the MDE, though no one has practically implemented it in the study of three dimensional mesostructures so far.

In this section, a new numerical strategy incorporating the spherical harmonics expansion and plane-wave spectral collocation method with a multi-step backward differentiation formula (BDF) is developed. Computationally, this algorithm achieves an estimated $O(NKM)$ computational operation, which speeds up the computation by one order of magnitude in computation time, in comparison with a split-step algorithm. With this powerful numerical tool in hand, we are capable of broadening our study to more complicated micro-structures in two- and three-dimensional space, especially to the network-like structures Q^{230}.

3.4.1 Numerical approach

Although the actual procedures may vary, the strategy behind the numerical approaches to solve these equations is the same. One would take an initial guess for the fields $w_A(\mathbf{r})$ and $w_B(\mathbf{r})$ and then solve Eqs. (3.9) and (3.10) for the propagators. The density fields $\phi_A(\mathbf{r})$ and $\phi_B(\mathbf{r})$ can then be obtained from Eqs. (3.14)

and (3.15). A new set of fields can then be obtained from

$$w_{A,\text{out}}(\mathbf{r}) = (\chi L/a)\phi_B(\mathbf{r}) + \Big[w_{A,\text{in}}(\mathbf{r}) + w_{B,\text{in}}(\mathbf{r}) - \chi L/a\Big]/2 \tag{3.24}$$

$$w_{B,\text{out}}(\mathbf{r}) = (\chi L/a)\phi_A(\mathbf{r}) + \Big[w_{A,\text{in}}(\mathbf{r}) + w_{B,\text{in}}(\mathbf{r}) - \chi L/a\Big]/2 \tag{3.25}$$

where $w_{\gamma,\text{in(out)}}(\mathbf{r})$ represents the input(output) of field functions for segment component $\gamma = A, B$. The resulting self-consistent field equations can numerically be solved by an iterative strategy correcting the previous evaluations on Eqs. (3.11)-(3.12) accompanied with the incompressible constraint Eq. (3.13), which in turn rely on an accurate and efficient solution of MDEs, i.e. Eqs. (3.9)-(3.10).

In the actual implementation, the computational challenge stems from the fact that $q(\mathbf{r}, \mathbf{u}, s)$ in Eq. (3.9) or $q^*(\mathbf{r}, \mathbf{u}, s)$ in Eq. (3.10) contains 6 variables, including three spatial variables, x, y and z generally represented by $\mathbf{r}$, two angular variables, θ and ϕ, generally represented by $\mathbf{u}$ and one time-like variable s. In this work, we introduce a novel numerical scheme that can attack the computational problem of calculating $q(\mathbf{r}, \mathbf{u}, s)$ by maintaining full six variables. This is necessary to study the three-dimensional structure of the wormlike AB diblock copolymer problem.

Our treatment starts with the usual expansion of the propagator in terms of spherical harmonics in the real-space version. Using the abbreviation j for the integers l and m in a spherical harmonic, we consider

$$q(\mathbf{r}, \mathbf{u}, s) = \sum_{j=0}^{M-1} q_j(\mathbf{r}, s)\ \tilde{Y}_l^m(\mathbf{u}) \tag{3.26}$$

where the real spherical harmonics are defined by

$$\tilde{Y}_l^m(\mathbf{u}) = \begin{cases} \frac{1}{\sqrt{2}}\left[Y_l^m(\mathbf{u}) + (-1)^m Y_l^{-m}(\mathbf{u})\right] & \text{if } m > 0 \\ Y_l^0(\mathbf{u}) & \text{if } m = 0 \\ \frac{1}{i\sqrt{2}}\left[Y_l^{-m}(\mathbf{u}) - (-1)^m Y_l^m(\mathbf{u})\right] & \text{if } m < 0 \end{cases}$$

Here, $Y_l^m(\mathbf{u})$ denotes a standard spherical harmonic function [3]. The summation in Eq. (3.26) is truncated at M, where $M = (\bar{L}+1)^2$ represents the total number of spherical harmonic functions used in the expansion and $\bar{L}$ is the highest order of the truncated Legendre function.

Substituting the expansion in Eq. (3.26) into Eq. (3.9) and using the orthonormality condition, we arrive at

$$\frac{\partial}{\partial s}q_j(\mathbf{r},s) = \left[-l(l+1)\frac{L}{a} - w(\mathbf{r},s)\right] q_j(\mathbf{r},s) - L\sum_{j'=0}^{M-1} \mathbf{R}_{jj'}\cdot\nabla q_{j'}(\mathbf{r},s) \tag{3.27}$$

where a vector matrix has been defined

$$\mathbf{R}_{jj'} \equiv \frac{1}{4\pi}\int \mathrm{d}\mathbf{u}\ \mathbf{u}\tilde{Y}_l^m(\mathbf{u})\tilde{Y}_{l'}^{m'}(\mathbf{u}) \tag{3.28}$$

with the index j' abbreviating l' and m'.

The s-dependence in Eq. (3.27) is dealt with by a multistep implicit-explicit scheme, the backwards differentiation formula (BDF). The method implicitly treats the gradient terms and explicitly treats the source using an Adams-Bashforth formula [69]. The remarkable features of the method in applications of solving a time-dependent partial differential equation similar to our MDE, in terms of improved stability and high frequency decay, were demonstrated previously [4]. Thus, the method is especially suitable for the current problem where sharp-interfaces are expected. We note that BDF was successfully used in a Gaussian-chain based SCFT to study the AB diblock copolymer phase diagram previously [20]. Here we use a third-order BDF (BDF3) scheme, which renders Eq. (3.27) in the form

$$\begin{aligned}
&\frac{11}{6}q_j(\mathbf{r},s) - 3q_j(\mathbf{r},s-\Delta s) + \frac{3}{2}q_j(\mathbf{r},s-2\Delta s) - \frac{1}{3}q_j(\mathbf{r},s-3\Delta s)\\
&= -\Delta s l(l+1)\frac{L}{a}q_j(\mathbf{r},s) - \Delta s L\sum_{j'=0}^{M-1}\mathbf{R}_{jj'}\cdot\nabla q_{j'}(\mathbf{r},s)\\
&- \Delta s w(\mathbf{r},s)\Big[3q_j(\mathbf{r},s-\Delta s) - 3q_j(\mathbf{r},s-2\Delta s) + q_j(\mathbf{r},s-3\Delta s)\Big] + O(\Delta s^4).
\end{aligned} \tag{3.29}$$

where Δs is the step size for s taken in the computation. The method depends on multiple time steps for the calculation of the propagator at a current s. Initially, Euler's method and the Richardson extrapolation [93] were used to produce the function in the first few timesteps.

The $\mathbf{r}$-dependence in the above equation is then dealt with by a spectral collocation method which uses a plane-wave basis. Denoting $\hat{\mathcal{F}}$ as the standard Fourier

transform which manipulates a function from **r**-space- to **k**-space representations, we can simply rewrite Eq. (3.29) as

$$\sum_{j'=0}^{M-1} G_{jj'}(\mathbf{k}) q_{j'}(\mathbf{k}, s) = P_j(\mathbf{k}, s-\Delta s, s-2\Delta s, s-3\Delta s) \tag{3.30}$$

where

$$G_{jj'}(\mathbf{k}) = \frac{11}{6}\delta_{jj'} - \Delta s\left(-\frac{L}{a}l(l+1)\delta_{jj'} - L\mathbf{R}_{jj'}\cdot(i\mathbf{k})\right)$$

$$P_j(\mathbf{k}, s-\Delta s, s-2\Delta s, s-3\Delta s) = \hat{\mathcal{F}}\Bigg[3q_j(\mathbf{r}, s-\Delta s) - \frac{3}{2}q_j(\mathbf{r}, s-2\Delta s)$$

$$+ \frac{1}{3}q_j(\mathbf{r}, s-3\Delta s) - \Delta s w(\mathbf{r})\Big(3q_j(\mathbf{r}, s-\Delta s) - 3q_j(\mathbf{r}, s-2\Delta s) + q_j(\mathbf{r}, s-3\Delta s)\Big)\Bigg]$$

One important advantage of this formalism is that the matrix element $G_{jj'}(\mathbf{k})$ is independent of s and the iterative field $w(\mathbf{r}, s)$; we only need to calculate the inversion matrix $G(\mathbf{k})$ once, just in the initial setup of the computation. Finally, the propagator can be calculated from

$$q_j(\mathbf{k}, s) = \sum_{j'=0}^{M-1} G^{-1}_{jj'}(\mathbf{k}) P_{j'}(\mathbf{k}, s-\Delta s, s-2\Delta s, s-3\Delta s). \tag{3.31}$$

An inverse Fourier transformation yields the real-space propagator $q_j(\mathbf{r}, s)$.

We can estimate the number of computational operations needed in this algorithm. The most time-consuming operation is the multiplication between inverted matrix $G^{-1}(\mathbf{k})$ and vector $P(\mathbf{k}, s-\Delta s, s-2\Delta s, s-3\Delta s)$ at every **k**-space point, which costs $O(KM)$ operations due to the high sparsity of $G^{-1}(\mathbf{k})$, where K denotes the number of collocation points in the **k**-space. The total cost to propagate a solution forward from the initial condition to the end of the chain using N contour steps is thus $O(NKM)$. Compared with the computational cost $O(NKM^{3/2}\log_2 M)$ in the split-step algorithm previously proposed by Fredrickson [39], our current numerical algorithm is much more efficient. Taking an example of using $M \sim 40-60$, which is adequate in some of the calculations presented below, the actual computation time can be almost *one* order of magnitude faster. The fact that BDF3 has

a truncation error of $(\Delta s)^4$ allows us to use larger step size in s. This can be contrasted with the fact that the truncation error is of the order $(\Delta s)^3$ in the split-step algorithm.

The computation of the phase diagram presented in the next section also benefits from a number of other numerical treatments. Once the propagator is calculated, the next step is to revise the fields, $w_A(\mathbf{r})$ and $w_B(\mathbf{r})$, according to the newly obtained density profile. We utilize the Anderson mixing scheme proposed by Thompson et al [112] and developed by Matsen et al [109], to speed up the convergence. The Anderson mixing scheme updates the original field by incorporating the results from several preceding iterations. It has the capability of correcting the occasionally bad field-update. Appendix D explains the method further. The entire self-consistent calculation is considered convergent, once the error functions $d_{A,\text{total}}$ and $d_{B,\text{total}}$, defined in Appendix D, are smaller than a pre-specified tolerance.

To study *periodic* AB diblock copolymer structures, we need to specify the unit-cell size for every calculated structure. The structurally dependent free energy hence is a function of the unit-cell size [7]. The free energy needs to be minimized with respect to the unit cell size, for a given type of structure and given set of parameters, f, L/a, and $\chi L/a$. Because every calculation of F requires going through the entire self-consistent calculation mentioned above, which is a computationally expensive operation, the search for the optimal unit-cell size needs to be efficient and the search steps need to be limited. We found that the parabolic interpolation minimization algorithm is a suitable choice [93].

This work explored several ordered structures; some of them are shown in Fig. 3.8. The first initial guess for the fields, $w_A(\mathbf{r})$ and $w_B(\mathbf{r})$, was made based on the proposed profile of a periodic structure and contained non-vanishing wave vectors corresponding to the lowest wave length only. Such an assumption was used to conveniently guess a structure, though a symmetry constraint is not enforced in our general algorithm. The search for a stable structure at an adjacent point in the phase diagram benefits from a good initial condition, usually taken from an existing solution.

Finally, we list the numerical values for the parameters used in this work. The domain $[0, 1]$ for the contour variable s was divided into $N = 400$ parts, which

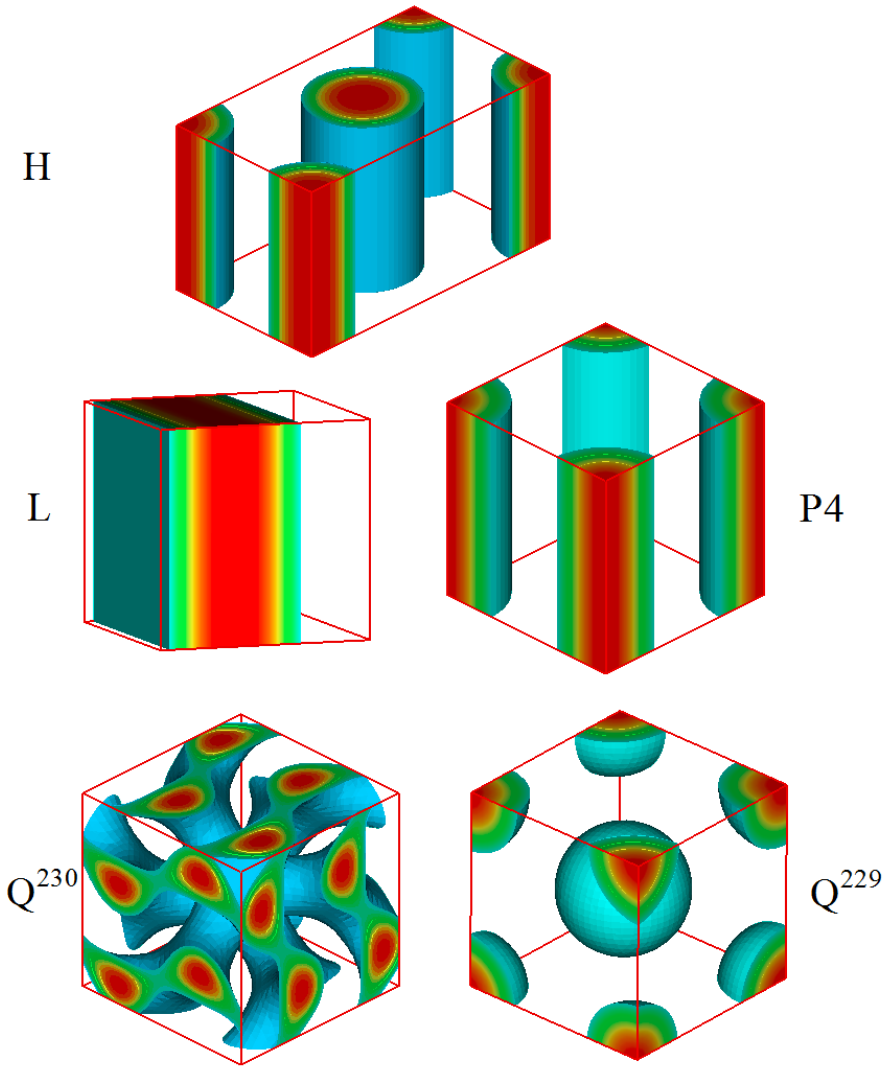

Figure 3.8: Equilibrium structures of H (hexagonally ordered cylinder), L (Lamellar), P4 (square ordered cylinder), Q^{230} (bicontinuous gyroid phase) and Q^{229} (body-centered spheres) obtained from the current work. These density plots show high probability in red and low probability in light blue.

implies a step size $\Delta s = 0.0025$. The three-dimensional spatial domain was divided into 32 spectral collocation points in each of the three x, y and z directions, which means that a total of $32 \times 32 \times 32$ plan-wave bases were used for a three-dimensional structure. In the orientational domain, spherical harmonics are taken up to the $\bar{L} = 8$ rank, which implies that a total of $M = (\bar{L} + 1)^2 = 81$ bases were used. In the calculation, we found that rigid chains (small L/a) require higher order of M to achieve the same precision in comparison with the calculation for more flexible chains. The self-consistent Eqs. 3.11 - 3.15 are solved iteratively until the differences $d_{A,\text{total}}$ and $d_{B,\text{total}}$ are both less than 10^{-5}.

We take the Q^{230} phase for $L/a = 3$, which will be defined in the next section, as an example. The calculation of a converging structure for a specific point on the phase diagram, including minimization with respect to the unit-cell size, took approximately 8 hours on a AMD Opteron 2.2 GHz with 16 parallel processing power, after the implementation of a publicly available fast-Fourier transform (FFTW) package [44]. The total CPU used to accomplish the calculation of the phase diagrams shown in Fig. 3.9 costs approximately 140 CPU years.

3.4.2 Results and discussion

The current work concerns the effects of the persistence length of wormlike chains on the stability boundaries for the ordered phases in AB diblock copolymers. As discussed above, the physical properties are concurrently controlled by three parameters, the volume fraction of the A component f, the number of effective Kuhn segments along the wormlike chain L/a, and the Flory-Huggins parameter χ, which appears in our theory as a combined $\chi L/a$. In comparison with the phase behavior based on the Gaussian chain model, that have been extensively studied in the $L/a \gg 1$ limit [16, 24, 11, 12, 27, 28, 63], we focus here on the important role played by semiflexibity of a wormlike chain, in the moderate L/a range. The numerical strategy developed in this paper has a satisfactory performance in accuracy and efficiency in solving the self-consistent field equations resulting from the wormlike chain model, even for the extraordinarily complicated geometries, such as gyroid structure [64, 79, 114, 20]. Some aspects of the lamellar structure were explored

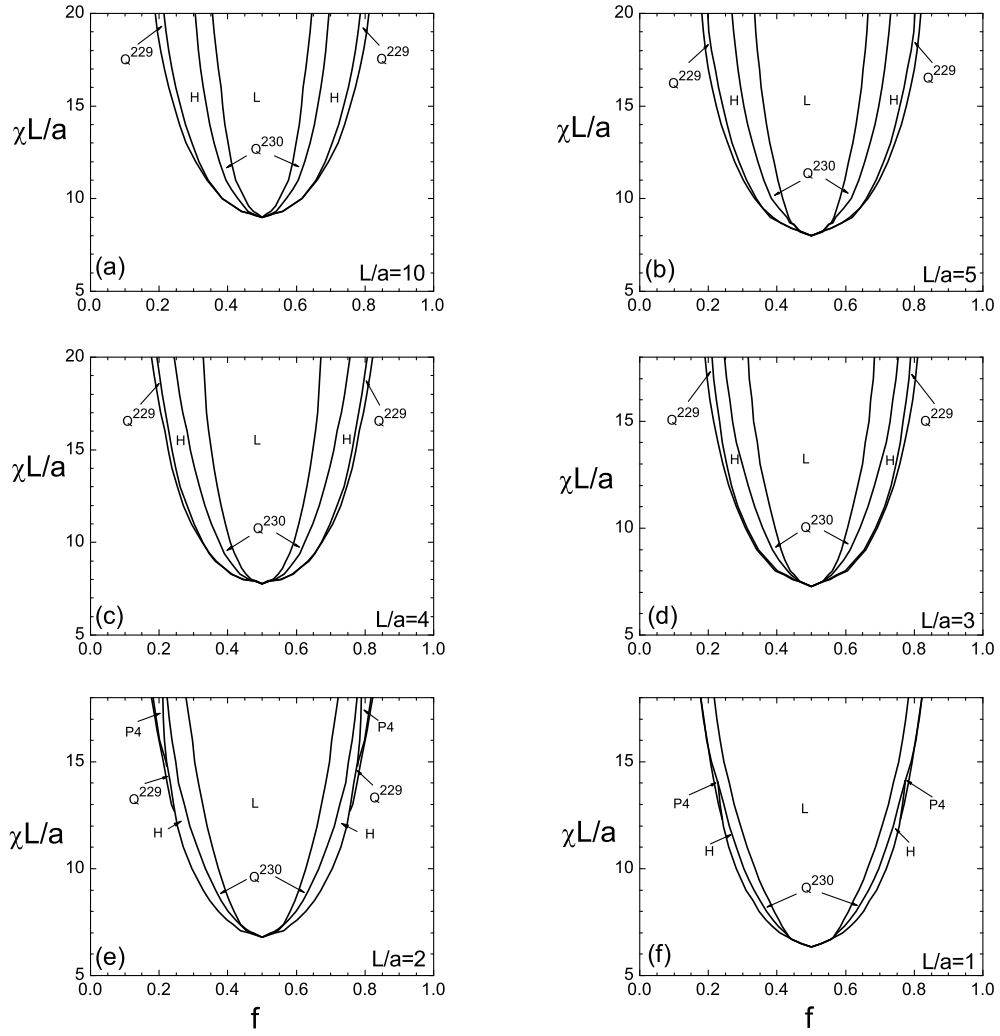

Figure 3.9: The phase diagrams of wormlike AB diblock copolymers, shown in the $\chi L/a$-f space, for various values of persistency: (a) $L/a = 10$, (b) 5, (c) 4, (d) 3, (e) 2 and (f) 1. The the stable regions for L (Lamellar), Q^{230} (bicontinuous gyroid), H (hexagonally ordered cylinder), Q^{229} (body-centered sphere) and P4 (square ordered cylinder) are labeled in the diagrams.

previously [76, 63].

In Fig. 3.9, we present the phase diagrams of wormlike AB diblock copolymers determined in this work in the $\chi L/a - f$ space over a range of chain rigidities ($L/a = 1$ to $L/a = 10$). A large L/a implies that the polymers in the system are flexible; in this limit we expect to see the recovery of the the well-known phase diagram based on the Gaussian-chain model [79, 20]. Indeed, the phase diagram for $L/a = 10$ is very close to the phase diagram of AB diblock copolymers. Numerically, the asymptotic behavior is further illustrated in Table 3.1 by using the locations of the phase boundaries in terms of f for two examples of $\chi L/a$. The phase boundaries for a system consisting of rather flexible chains, $L/a = 100$, for example, are in good agreement with those predicted from the Gaussian-Chain model [79], indicated by parentheses in this Table.

Table 3.1: Two examples ($\chi L/a = 12$ and 16) of the phase boundaries between H and Q^{230}, Q^{230} and L, determined in the current work for wormlike AB diblock copolymers at different flexibilities L/a. The boundaries are specified by the value of f, $f_{H/Q^{230}}$ and $f_{Q^{230}/L}$; the size of the Q^{230} phase is also shown by considering $\Delta f_{Q^{230}} = f_{Q^{230}/L} - f_{H/Q^{230}}$. In the large L/a limit, the data asymptotically approach the phase boundaries determined based on the Gaussian chain model, which are shown in the parentheses, taken from Matsen's previous work [79].

	$\chi L/a = 12$			$\chi L/a = 16$		
L/a	$f_{H/Q^{230}}$	$f_{Q^{230}/L}$	$\Delta f_{Q^{230}}$	$f_{H/Q^{230}}$	$f_{Q^{230}/L}$	$\Delta f_{Q^{230}}$
100	0.412	0.431	0.019	0.355	0.393	0.038
	(0.419)	(0.434)	(0.015)	(0.359)	(0.396)	(0.036)
10	0.377	0.411	0.034	0.328	0.381	0.053
5	0.347	0.392	0.045	0.296	0.354	0.058
4	0.332	0.381	0.049	0.281	0.343	0.062
3	0.315	0.364	0.049	0.262	0.326	0.064
2	0.294	0.340	0.046	0.237	0.295	0.058
1	0.262	0.294	0.032	0.191	0.233	0.042

Can we analytically show that the wormlike-chain MDE recovers the Gaussian-chain MDE in the flexible chain limit of $L/a \gg 1$? The recovery of the Gaussian chain result is not a trivial notion and depends on other length scales in a specific system as well. In the current system, together with L and a, a third length scale, W (unit-cell size or the interfacial width between the A/B domains), needs to be considered. The scaling of W/a as a function of L/a determines whether or not the Gaussian-chain limit is approached, together with the $L/a \gg 1$ requirement. Assuming $W/a \sim \sqrt{L/a}$ in the large L/a limit and expanding the propagator in terms of spherical harmonic functions and powers of small a/W, in Appendix C we analytically show that the MDE of the Gaussian can be exactly recovered in the large L/a limit from the MDE of a wormlike chain. The proof is given in a three-dimensional system, suitable for the current consideration of the phase diagram

for a three-dimensional structure with the complete set of variables, x, y, z, θ and ϕ. Previously, a similar proof was given for one-dimensional symmetric polymer blends by Schmid and Müller, for a reduced dependence of q on z and θ only [101].

Note that $W/a \sim \sqrt{L/a}$ is automatically embedded in the Gaussian-chain MDE, but needs to be tested for the wormlike AB diblock copolymer in the large L/a limit. To examine the length scales in the system, we define two measurements for the ordered structures, the unit-cell size $D(f, L/a, \chi L/a)$ and the interfacial width $W(f, L/a, \chi L/a)$. While the former can be directly measured after optimization of the free energy, the definition of the latter is not straightforward for a three-dimensional structure. To the best of our knowledge, the explicit definitions of interfacial width W were mostly based on a one-dimensional structure such as L, consistent with that originally suggested by Helfand and Tagami [57] and later used by Matsen and Bates [79]. In this paper, we suggest using

$$W \equiv \left[\text{Max} \left| \nabla \phi_A(\mathbf{r}) \right| \right]^{-1} \tag{3.32}$$

where ∇ is a gradient operator and the function Max takes the maximum value of its argument. This definition takes into account any dramatic variation of the density profile at a three-dimensional AB interface; it recovers the simple derivative definition of W for a one-dimensional system previously used. The rescaled interfacial width $W/a \equiv \bar{W}(f, L/a, \chi L/a)$ is a function of f, L/a and $\chi L/a$ as well. Using $\chi L/a = 16$ as an example, we illustrate both $\tilde{D}$ and $\tilde{W}$ in Fig. 3.10 as functions of L/a at various values of f, for most ordered structures studied in this work. The asymptotic slope 1/2 in the large L/a limit on a double-logarithmic plot region indicates that indeed $W/a \sim \sqrt{L/a}$ is satisfied in the current system, independent of the specific micro-structures.

We now move to lower L/a cases. In comparison with the phase diagram in Fig. 3.9(a) for $L/a = 10$, the phase diagrams in Fig. 3.9(b), (c) and (d) for L/a =5, 4 and 3 have basically the same structure: the three classical phases L, H and Q^{229} occupy the majority of the phase diagram while Q^{230} occurs over only a narrow range of composition fraction f. We found that an increase of the chain rigidity alters the relative sizes of the specific stable phases; notably, the L and Q^{230} phase

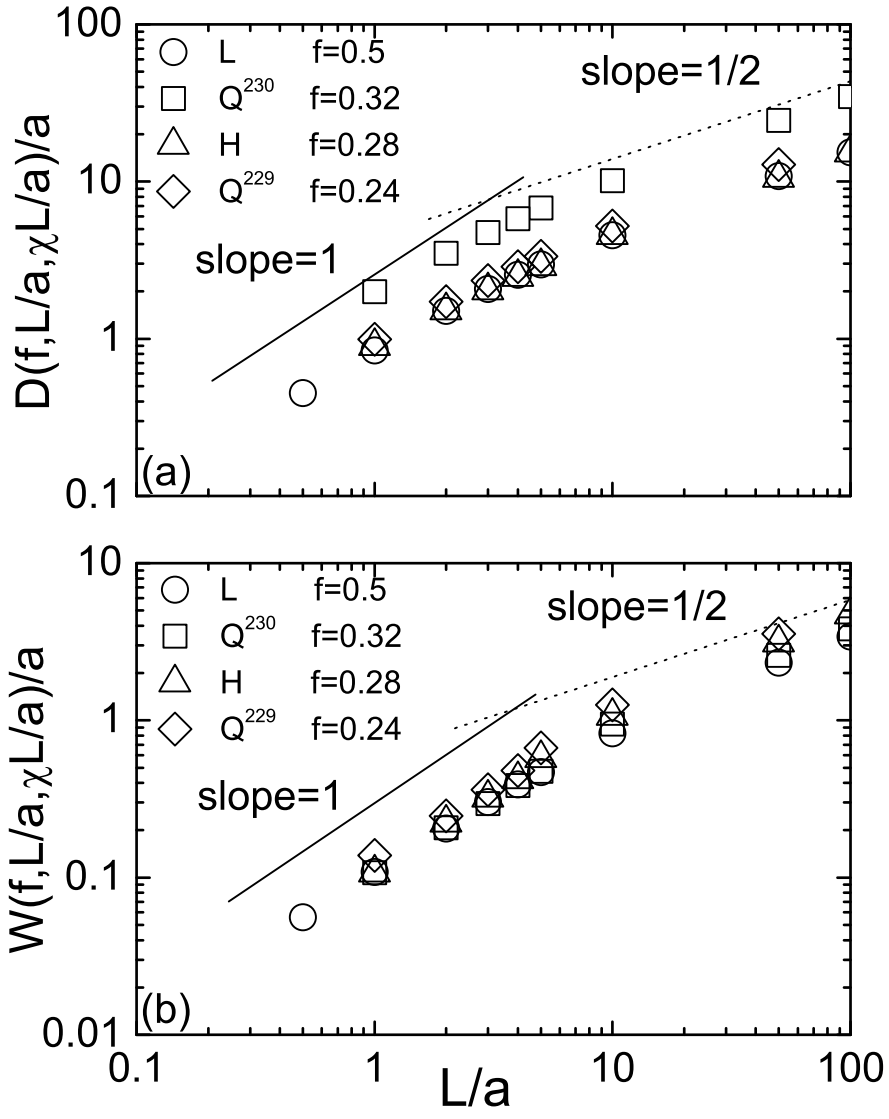

Figure 3.10: Double-logarithmic plots of (a) reduced unit-cell size $D(f, L/a, \chi L/a)/a$ and (b) interfacial width $W(f, L/a, \chi L/a)/a$ as functions of the chain length L/a at $\chi L/a = 16$ for phases L (circle), Q^{230} (square), H (triangle) and Q^{229} (diamond), respectively. Asymptotic power laws at large and small L/a are indicated by slopes 1/2 (dotted line) and 1 (solid line), respectively. The data for the L phase exactly matches those determined earlier by using a different algorithm [63].

regions expand and the H and Q^{229} regions shrink. Physically, a more rigid polymer chain looses less conformational entropy in a stretched conformation in comparison with its Gaussian counterpart of the same length. One consequence in our system is that rigidity makes it easier for the system to phase-separate (which decreases a polymer's entropy) for the same value of the $\chi L/a$ parameter. A similar observation as also obtained by Friedel *et al.* [43], who used an approach based on the random phase approximation in combination with a cumulant expansion for the semiflexible form factor.

As chain rigidity increases further, the Q^{229} phase region starts to disappear and a new stable micro-structure, P4, emerges in the region between the H and disordered region, beyond $\chi L/a = 15.0$ approximately. This can be viewed in Fig. 3.9(e) and (f) for the $L/a = 2$ and 1 cases. Recently, a P4 phase self-assembled from T-shaped liquid crystalline molecules was reported in an experimental study [9]. Our calculation is the first time that predicts P4 shows up in an AB diblock copolymer phase diagram. Our current calculations focus on the region $\chi L/a \leq 18.0$; higher $\chi L/a$ would produce even a sharper interface, which requires a higher spatial resolution, hence more spectral collocation points. A more careful study on the properties of the three phases, H, P4, Q^{229}, in the $\chi L/a \gtrsim 18.0$ region would further reveal the competition between the three phases, but is not done here.

Another interesting feature of these phase diagrams is the expansion of the L region as L/a is lowered. Examining the series of the phase diagrams in Fig. 3.9, there is a tendency that the L phase might take over the entire region of ordered structures in the rod limit, $L/a \ll 1$. This is a limit that is worth further study by including more spherical harmonics in our expansion and refining the divisions in the s-space, for the calculation of the propagator, which poises an even more computational challenge.

The description of the chain configuration changing from the flexible limit to the rod-like limit for wormlike chain model can be illustrated by $\tilde{D}$ and $\tilde{W}$ as well. In the $L/a \ll 1$ limit, we expect that both length scales become proportional to L, characteristic of rodlike polymers, rather than $\sqrt{La}$, characteristic of flexible chains. This can be viewed in Fig. 3.10 for various values of f. Indeed, the asymptotic slope 1 in the small L/a region on a double-logarithmic plot region indicates that

$W \sim D \sim L$, independent of the specific micro-structures.

It is interesting to note that the crossover between the rodlike behavior and the coil-like behavior occurs near $L/a \sim 2$. All major structures display this crossover at approximately the same value, shown in Fig. 3.10. The fact that $L/a \sim 2$ is the crossover point can be found in other wormlike chain systems as well [16, 61]. The solution to the isotropic-nematic phase transition and the isotropic-nematic interface of wormlike polymers, incorporating an Onsager interaction, display a characteristic turning point near this value [16, 61]. Recently, through the calculation of the end-to-end distance distribution function in two dimensions for a wormlike chain without the external field, Spakowitz and Wang argued for the existence of a double-peaked structure for intermediate chain rigidities [108]. As well, in three dimensions Mehraeen et al found that the crossover between rigid rod and flexible chain occurs near $L/a = 1.9$ for a unperturbated wormlike chain [81].

Table 3.1 shows the variation of the phase boundaries associated with Q^{230} as a function of the chain rigidity L/a. As mentioned above, at $L/a = 100$ our results are very close to those found based on the Gaussian chain model. However, the boundaries of Q^{230} for $L/a = 10$ already deviate from Gaussian-chain results, indicating that semiflexibility effects need to be considered even for arelatively flexible chain with L/a as large as 10. Another feature in the Table is that the gradual increase of chain rigidity enlarges the stable region of Q^{230}, pushing away both neighboring boundaries and accompanying a monotonic expansion of the lamellar phase. The variation of phase region size for Q^{230} ($\Delta f_{Q^{230}}$) undergoes an expansion and then contraction as the chain rigidity rises; the phase region approaches a maximal value at $L/a \sim 3$. This coincides with the crossover region discussed in the last paragraph.

Finally, we demonstrate an example, $\chi L/a = 12$, of the original numerical data used for determination of the stability of the Q^{230} phase with respect to the neighboring L and H phases. For such a specified $\chi L/a$, we calculated the free energy by scanning the f space near the transition boundaries, for various values of L/a. In Fig. 3.11, all curves near the transition point cross $\beta\Delta F = 0$ linearly for all considered chain rigidities. Characteristically this is a feature of a first-order transition, according to the mean-field understanding of the phase transition

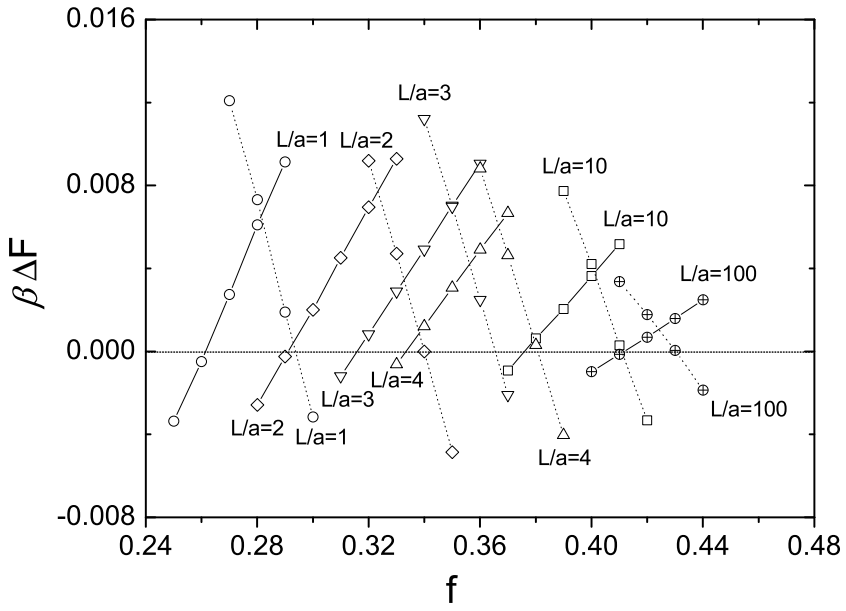

Figure 3.11: The free energy difference between the L and Q^{230} phases, $\beta\Delta F = \beta F_L - \beta F_{Q^{230}}$ (shown by by symbols with dotted lines), and between the H and Q^{230} phases, $\beta\Delta F = \beta F_H - \beta F_{Q^{230}}$ (shown by symbols with solid lines), as a function of f for $\chi L/a = 12$ at various values of persistency: $L/a = 100$ (circle-plus), 10 (square), 4 (up triangle), 3(down triangle), 2 (diamond) and 1 (circle). These plots demonstrate the stability of H and L relative to Q^{230}: H or L becomes stable if the free energy difference is negative.

theory. A similar free energy difference was argued by Leibler previously within a Gaussian-chain model [71]. Furthermore, we find that the stability region for Q^{230} is gradually pushed into smaller volume fraction f with the increase of chain rigidity (small L/a). Some detailed data is presented in Table 3.1. The figure also shows that the competing free energy per chain in the vicinity of a stable Q^{230} phase has an order of 0.01. This requires a high resolution in numerical determination of the free energy, currently available from the algorithm presented here.

3.5 Conclusion

We considered a self-consistent field theory formalism for the calculation of the phase behavior of AB diblock copolymers based on a wormlike chain model [63, 62]. In the flexible chain limit, our prediction based on the wormlike chain model to the DL stability boundary entirely recovers the one from the random phase approximation of the Gaussian chain model. Physically, a more rigid polymer chain looses less conformational entropy in a stretched conformation in comparison with its Gaussian counterpart of the same length. One consequence is that persistency makes it easier for the system to phase-separate for the same interaction parameter. It directly leads to the broadening of the lamellar stability region with increase of the chain rigidity. In addition, we also find that the DL phase transition is continuous for symmetric ($f = 1/2$) diblock copolymers while it is a first-order transition for $f \neq 1/2$ independent of the change of chain rigidity. Then, we extend the study to complicated three-dimensional morphologies by means of our designed numerical algorithm capable of solving the wormlike chain problem in full space, which used to be considered as an intractable task. We found that the extra chain rigidity parameter compared to the GSC model plays a predominant role in determining the wormlike AB diblock phase diagram. The increase of chain rigidity will lead to a swelling of the lamellar phase and a shrinking of the hexagonal phase and vanishing of the cubic phase. However, the net-like gyroid phase will benefit from an appropriate increase of chain rigidity. The domain size and interfacial width for the morphologies observed in our calculation show that the wormlike chain model is able to depict well the polymer chain configuration from the flexible chain limit to the rigid-rod limit.

Chapter 4

Summary and Outlook

The wormlike chain model proposes that the polymer chain is an inextensible thread with a linear-elastic bending energy related to the persistence length λ, over which the orientational correlation between chain segments will decay exponentially. In this thesis, we focus on the application of the wormlike chain model based on the self-consistent field theory (SCFT) in two typical polymeric systems: I). Interface between the *isotropic* phase and *nematic* phase in Chapter 2; II). Self-organization of AB diblock copolymers in Chapter 3.

In Chapter 2, taking the persistence length of the polymer chain as a significant factor, we study the chain rigidity effect on the physical properties of the isotropic-nematic interface continuously ranging from the rigid-rod limit to the flexible chain limit [61]. Our calculations showed that the interfacial tension decreases as the chain softened, reaches a minimum and then has an approximately linear rise in the flexible limit, and polymer chains always have a preferential alignment parallel to the orientation of interface near the phase interface. An empirical formula which is fitted from our numerical calculation is obtained for describing the interfacial tension with the variations of chain rigidity and the angle between the orientation of the interface normal and the assumed orientation of the director of the nematic phase.

In Chapter 3, firstly, the stability of the disordered-lamellar (DL) phase boundary is explored in terms of the variation of the component volume fraction f from

the flexible chain limit to the rigid-rod limit [63]. In the flexible chain limit, our prediction based on the wormlike chain model for the DL stability boundary entirely recovers the one from the random phase approximation of the Gaussian chain model. It directly leads to the broadening of the lamellar stability region with increase of the chain rigidity. In addition, we also find that the DL phase transition is continuous for symmetric ($f = 1/2$) diblock copolymers while it is a first-order transition for $f \neq 1/2$ independent of the change of chain rigidity. Then, we extended the study to complicated three-dimensional morphologies by means of our newly designed numerical algorithm capable of solving the wormlike chain problem in full 3D space [62], which was previously considered as an intractable task. We found that the extra chain rigidity parameter compared to the GSC model plays a predominant role in determining the wormlike AB diblock phase diagram. The increase of chain rigidity will lead to a swelling of the lamellar phase and a shrinking of the hexagonal phase and vanishing of the cubic phase. However, the net-like gyroid phase is benefited from an appropriate increase of chain rigidity. The domain size and interfacial width for the morphologies observed in our calculation show that the wormlike chain model is able to depict well the polymer chain configuration from the flexible chain limit to the rigid-rod limit.

The wormlike chain model can be utilized in a system in the framework of SCFT, where the coupling effect from the positional and orientational variables is the major concern. The efficient and accurate numerical scheme proposed in Chapter 3 eliminates the technical bottleneck and opens the door to applications of the WLC model on many interesting systems which could not be tackled previously. In the following, I will address some of these issues.

The rod-coil system

Of recent interest are systems consisting of rod-coil block copolymers, which appear to have more complicated nanoscale structures in experiments [10, 19]. The experimental phase diagram for rod-coil block copolymers was constructed by Olsen et al [87, 88, 89]. Theoretically, Halperin took the analytical free energy calculations for rod-coil diblock copolymers into account within the scaling approach to study the phase transition between smectic A and smectic C [51]. Shortly thereafter, Williams

and Fredrickson extended the theoretical calculations to "hockey puck" micelles, where the rods are packed axially into cylinders [120]. Matsen and Barrett used the self-consistent mean field theory based on the Semenov-Vasilenko model [102] to study both smectic monolayer and bilayer phases with the assumption that all rods perfectly align along the same orientation [78]. Later, Pryamitsyn and Ganesan used a similar method considering the anisotropic Maier-Saupe interaction and explored the 1D and 2D spatial phase diagram with the variation of volume fraction of the component coil/rod [94]. Recently, the wormlike chain model incorporating the anisotropic interaction was used to study the rod-coil diblock copolymers by Song et al [107] at a self-consistent mean field level. They constructed a lamellar phase diagram consisting of isotropic, nematic, smectic A and smectic C phases. However, the theoretical prediction of SCFT on the three-dimensional structures, which is the main concentration in experiments, is still lacking so far. The formalism in this thesis can be easily generalized to this system provided that different persistence lengths are supposed on both chain blocks. The adjustable persistence in the WLC model will also highly enrich the theoretically explored mesostructures self-assembled from rod-coil block copolymers.

Liquid crystalline polymers

Liquid crystalline polymers combining the properties of both liquid crystals and polymers have potential applications, such as optical displays and information storage, pressure and temperature sensors, shape-memory materials and so on. They can be categorized into two groups in terms of structures: *main-chain polymers*: the backbone of polymers is composed of rigid mesogenic parts connected to each other with flexible links; *side-chain polymers*: the liquid crystal side groups are linked to the backbone via flexible spacers. The competition between the chain configuration entropy and the orientational order from the main-chain or side-chain liquid crystalline polymers leads to various complicated structures. Many experimental research efforts have been dedicated to investigate the factors, such as the flexibility of the backbone [23, 98], the length of the spacer [22, 92], molecular weight [91, 66], and mesogen graft density [99, 21]. Recently, a new theoretical model was built by Prof. Wang's group [119, 126], accounting for both a global coupling

between the polymer backbone and the nematic field and a local coupling between the polymer backbone and its attached liquid crystal group. A WLC-based SCFT can be straightforwardly applied in this topic, to explore the fascinating structures. We also noticed that there have been several works [122] devoted to this topic very recently, but they considered the calculations in homogeneous bulk systems independent of the positional variable **r**.

Chiral polymers

Chiral molecules are those molecules which lack mirror or reflection symmetry and thus chirality has a geometrical essence. They can form a chiral nematic (or cholesteric) phase, which corresponds to a system with the preferred nematic director rotating throughout the sample periodically. Chirality is a well-studied feature in the class of conjugated polymers, which have attracted significant attention due to its applications in LEDs, solar cells *etc* [116]. At the same time, chiral recognition also has the particular significance in biopolymers, such as proteins. Recently, a new theoretical model which accounts for both the thermodynamic costs of developing orientational order in block copolymer melts as well as the costs for gradients of that orientational order was constructed to illustrate the properties of chiral block copolymers by the GSC-based SCFT [125]. In fact, the WLC model is a more obvious choice than the GSC model for this system. It is worth developing a model describing the chirality of polymers in the framework of WLC-based SCFT in the future.

Appendix A

The rod limit: $\alpha = L/a \ll 1$

In this Appendix, we show that our formalism is identical to the Onsager model for a liquid-crystal interface in the limit of $a \gg L$. The modified diffusion equation (Eq. 2.9), can be reduced to

$$\frac{\partial}{\partial s} q(\mathbf{r}, \mathbf{u}, s) = \Big[-L\mathbf{u} \cdot \nabla_{\mathbf{r}} - w(\mathbf{r}, \mathbf{u}) \Big] q(\mathbf{r}, \mathbf{u}, s). \tag{A.1}$$

By directly taking derivative, we can show that A.1 can be formally solved,

$$q(\mathbf{r}, \mathbf{u}, s) = \exp\Big\{ - \int_0^s w(\mathbf{r} - s\,'L\mathbf{u}, \mathbf{u}) \mathrm{d}s' \Big\}. \tag{A.2}$$

We can then write the density of segments, labelled s along rods,

$$\begin{aligned} \phi(\mathbf{r}, \mathbf{u}, s) &= \frac{n}{4\pi V a \rho_0 Q} q(\mathbf{r}, \mathbf{u}, s) q(\mathbf{r}, -\mathbf{u}, 1-s) \\ &= \frac{nL}{4\pi V a \rho_0 Q} \exp\Big[- \int_0^1 w(\mathbf{r} + s'L\mathbf{u} - sL\mathbf{u}, \mathbf{u}) \mathrm{d}s' \Big], \end{aligned} \tag{A.3}$$

which satisfies the normalization condition $\int \mathrm{d}\mathbf{r}\, \mathrm{d}\mathbf{u} \phi(\mathbf{r}, \mathbf{u}, s) = V$. In the above, the partition function of a single chain reads

$$Q = \frac{1}{4\pi V} \int \mathrm{d}\mathbf{r} \mathrm{d}\mathbf{u} \exp\Big[- \int_0^1 w(\mathbf{r} + L\mathbf{u}s, \mathbf{u}) \mathrm{d}s \Big]. \tag{A.4}$$

The above solution of $\phi(\mathbf{r}, \mathbf{u}, s)$ has the mathematical property,

$$\phi\left[\mathbf{r} - L\mathbf{u}(1/2 - s), \mathbf{u}, s\right] = \phi(\mathbf{r}, \mathbf{u}, 1/2)$$

which is valid for rod-like molecules only.

There are three terms in the free energy, Eq. 2.6. The last term on the right-hand side can be expressed as

$$\begin{aligned}\text{Last term} &= -\frac{1}{V}\int \mathrm{d}\mathbf{r}\,\mathrm{d}\mathbf{u} w(\mathbf{r},\mathbf{u})\phi(\mathbf{r},\mathbf{u}) \\ &= -\frac{1}{V}\int_0^1 \mathrm{d}s \int \mathrm{d}\mathbf{r}\,\mathrm{d}\mathbf{u} w(\mathbf{r},\mathbf{u})\phi(\mathbf{r},\mathbf{u},s) \\ &= -\frac{1}{V}\int_0^1 \mathrm{d}s \int \mathrm{d}\mathbf{r}\mathrm{d}\mathbf{u} w(\mathbf{r}+sL\mathbf{u}-L\mathbf{u}/2,\mathbf{u})\phi(\mathbf{r},\mathbf{u},1/2). \quad \text{(A.5)}\end{aligned}$$

On the basis of Eq. A.3, we have

$$\text{Last term} = \frac{a\rho_0}{nL}\int \mathrm{d}\mathbf{r}\mathrm{d}\mathbf{u}\phi(\mathbf{r},\mathbf{u},1/2)\ln[\rho_0\phi(\mathbf{r},\mathbf{u},1/2)] - \ln\left(\frac{n}{Q}\right) - \ln\left(\frac{L}{4\pi V a}\right). \quad \text{(A.6)}$$

The excluded-volume interaction term in Eq. 2.6 can also be written as

$$\begin{aligned}&\frac{a^2 d\rho_0^2}{n}\int \mathrm{d}s\mathrm{d}s'\mathrm{d}\mathbf{r}\mathrm{d}\mathbf{r}'\mathrm{d}\mathbf{u}\mathrm{d}\mathbf{u}'\phi(\mathbf{r},\mathbf{u},s)\phi(\mathbf{r}',\mathbf{u}',s')|\mathbf{u}\times\mathbf{u}'|\delta(\mathbf{r}-\mathbf{r}') \\ &= \frac{a^2 d\rho_0^2}{n}\int \mathrm{d}s\mathrm{d}s'\int \mathrm{d}\mathbf{r}\mathrm{d}\mathbf{r}'\mathrm{d}\mathbf{u}\mathrm{d}\mathbf{u}'\phi(\mathbf{r},\mathbf{u},1/2)\phi(\mathbf{r}',\mathbf{u}',1/2)|\mathbf{u}\times\mathbf{u}'| \\ &\times\delta(\mathbf{r}+sL\mathbf{u}-L\mathbf{u}/2,\mathbf{r}'+s'L\mathbf{u}'-L\mathbf{u}'/2) \quad \text{(A.7)}\end{aligned}$$

Instead of $\phi(\mathbf{r},\mathbf{u},1/2)$, we can introduce the number density of rods, represented by the center of mass of each rod, $\rho(\mathbf{r},\mathbf{u}) \equiv (a/L)\rho_0\phi(\mathbf{r},\mathbf{u},1/2)$, the Helmholtz free energy of the entire system can then be written as

$$\begin{aligned}\frac{nF}{k_BT} &= \int \mathrm{d}\mathbf{r}\mathrm{d}\mathbf{u}\rho(\mathbf{r},\mathbf{u})\ln\rho(\mathbf{r},\mathbf{u}) \\ &+ \frac{1}{2}\int \mathrm{d}\mathbf{r}\mathrm{d}\mathbf{r}'\mathrm{d}\mathbf{u}\mathrm{d}\mathbf{u}'\rho(\mathbf{r},\mathbf{u})\rho(\mathbf{r}',\mathbf{u}')(2d)|\mathbf{u}\times\mathbf{u}'|\omega(\mathbf{r},\mathbf{r}',\mathbf{u},\mathbf{u}'), \quad \text{(A.8)}\end{aligned}$$

where $\omega(\mathbf{r},\mathbf{r}',\mathbf{u},\mathbf{u}') \equiv \int \mathrm{d}s\mathrm{d}s'\delta(\mathbf{r}+sL\mathbf{u}-L\mathbf{u}/2,\mathbf{r}'+s'L\mathbf{u}'-L\mathbf{u}'/2)$, within a trivial $\ln(L/4\pi Va)$ constant shift. The above free energy is the starting point of the model considered in Refs. [18, 17, 80, 115, 32, 104]. Note that the Kuhn length a disappears completely in A.8.

Appendix B

The flexible chain limit: $\alpha = L/a \gg 1$

In this Appendix, we show that our formalism is identical to the free energy model for a liquid-crystal interface formed by lytropic polymers, in the limit of $L \gg a$. One important fact is such that in order to reach the isotropic-nematic transition point, the segmental density [65, 16, 118] can be estimated to have the order of magnitude

$$\frac{nL}{Va} \sim \frac{1}{a^2 d}, \tag{B.1}$$

hence $n^{-1} \sim (L/a)(a^2 d/V)$. Using this estimate we can show that the second and third terms of Eq. 2.6 have the order of magnitude L/a, much greater than the $\ln(L/a)$-order of the $\ln(n/Q)$ term in Eq. 2.6. The latter can thus be dropped in the limit $L \gg a$. The grand thermodynamic potential for the system can then be written as

$$\begin{aligned}\frac{\Xi}{k_B T} = &- \frac{a\rho_0}{L}\int \mathrm{d}\mathbf{r}\,\mathrm{d}\mathbf{u} w(\mathbf{r},\mathbf{u})\phi(\mathbf{r},\mathbf{u}) + a^2 d\rho_0^2 \int \mathrm{d}\mathbf{r}\,\mathrm{d}\mathbf{u}\mathrm{d}\mathbf{u}'\phi(\mathbf{r},\mathbf{u})|\mathbf{u}\times\mathbf{u}'|\phi(\mathbf{r},\mathbf{u}') \\ &- \frac{a\rho_0\bar{\mu}}{L}\int \mathrm{d}\mathbf{r}\,\mathrm{d}\mathbf{u}\phi(\mathbf{r},\mathbf{u})\end{aligned} \tag{B.2}$$

where $\bar{\mu} \equiv \mu/k_B T$ is the chemical potential per chain.

In the long-chain limit, $q(\mathbf{r},\mathbf{u},s)$ becomes s-independent in most regions of s,

$$q(\mathbf{r},\mathbf{u},s) \sim \tilde{q}(\mathbf{r},\mathbf{u}) \tag{B.3}$$

According to Eq. 2.9, we can then consider a solution to

$$\left[\frac{L}{a}\nabla^2_{\mathbf{u}} - L\mathbf{u}\cdot\nabla - w(\mathbf{r},\mathbf{u})\right]\tilde{q}(\mathbf{r},\mathbf{u}) = 0 \tag{B.4}$$

Note that $\phi(\mathbf{r},\mathbf{u})$ is related to $\tilde{q}(\mathbf{r},\mathbf{u})$ by

$$\phi(\mathbf{r},\mathbf{u}) \propto \tilde{q}(\mathbf{r},\mathbf{u})\tilde{q}(\mathbf{r},-\mathbf{u}) \tag{B.5}$$

up to a proportional coefficient.

Eqs. B.2, B.4 and B.5 are identical to Eqs. (1), (4) and (6) in Reference [12] for the segmental density $\phi(\mathbf{r},\mathbf{u})$, which was denoted as $\rho(\mathbf{x},\mathbf{u})$ in Reference [12]. Introducing a chain density $\rho_c(\mathbf{r},\mathbf{u}) = (a/L)\rho_0\phi(\mathbf{r},\mathbf{u})$, we can also show that Eqs. B.2, B.4 and B.5 are the same as the starting Eqs. (1), (2) and (3) in Reference [24] , except for a misprint of factor 1/2 in Eq. (2) of Reference [24] introduced in the writing-up stage while the original calculation was performed correctly with no such a factor.

Appendix C

Recovery of the Gaussian-chain modified diffusion equation in the limit $L/a \gg 1$

In this appendix, we analytically show that the Gaussian-chain modified diffusion equation (MDE) can be recovered by taking the $L/a \gg 1$ limit and assuming the $W \sim \sqrt{La}$ scaling in the wormlike-chain MDE. The main step is to consider the reduced coordinate,

$$\bar{\mathbf{r}} \equiv \mathbf{r}/W, \tag{C.1}$$

in the problem, where W is a typical length scale such as the unit-cell size. Our approach is to take an expansion in powers of a/W, and to identify the leading terms that are important asymptotically.

First we expand the propagator $q(\mathbf{r}, \mathbf{u}, s)$ in terms of spherical harmonic functions $Y_l^m(\mathbf{u})$,

$$q(\mathbf{r}, \mathbf{u}, s) = \sum_{l=0}^{\infty} \sum_{m=-l}^{l} q_l^m(\mathbf{r}, s) Y_l^m(\mathbf{u}). \tag{C.2}$$

where

$$q_l^m(\mathbf{r}, s) = \frac{1}{4\pi} \int \mathrm{d}\mathbf{u} Y_l^{m*}(\mathbf{u}) q(\mathbf{r}, \mathbf{u}, s) \tag{C.3}$$

and * denotes the complex conjugate. Substituting Eq. (C.2) into Eq. (3.9) and using the orthogonality condition, we obtain,

$$\frac{\partial}{\partial s}q_l^m(\mathbf{r},s)=\left[-l(l+1)\frac{L}{a}-w(\mathbf{r})\right]q_l^m(\mathbf{r},s) \\ -\frac{L}{4\pi}\int \mathrm{d}\mathbf{u}\; Y_l^{m*}(\mathbf{u})\left[\sum_{l'=0}^{\infty}\sum_{m'=-l'}^{l'} Y_{l'}^{m'}(\mathbf{u})\mathbf{u}\cdot\nabla_{\mathbf{r}}q_{l'}^{m'}(\mathbf{r},s)\right]. \tag{C.4}$$

By making use of the recurrence formula [3], the last term on the right hand of Eq. (C.4) can be further expressed as

$$\begin{aligned}
&\frac{L}{4\pi}\int \mathrm{d}\mathbf{u}\; Y_l^{m*}(\mathbf{u})\left[\sum_{l'=0}^{\infty}\sum_{m'=-l'}^{l'} Y_{l'}^{m'}(\mathbf{u})\mathbf{u}\cdot\nabla_{\mathbf{r}}q_{l'}^{m'}(\mathbf{r},s)\right] \\
&=\frac{L}{a}\frac{a}{W}\frac{1}{2}\left[\sqrt{\frac{(l-m+1)(l-m+2)}{(2l+1)(2l+3)}}\frac{\partial}{\partial\bar{x}}q_{l+1}^{m-1}-\sqrt{\frac{(l+m)(l+m-1)}{(2l-1)(2l+1)}}\frac{\partial}{\partial\bar{x}}q_{l-1}^{m-1}\right. \\
&\left.-\sqrt{\frac{(l+m+1)(l+m+2)}{(2l+1)(2l+3)}}\frac{\partial}{\partial\bar{x}}q_{l+1}^{m+1}+\sqrt{\frac{(l-m)(l-m-1)}{(2l-1)(2l+1)}}\frac{\partial}{\partial\bar{x}}q_{l-1}^{m+1}\right] \\
&+\frac{L}{a}\frac{a}{W}\frac{1}{2i}\left[\sqrt{\frac{(l-m+1)(l-m+2)}{(2l+1)(2l+3)}}\frac{\partial}{\partial\bar{y}}q_{l+1}^{m-1}-\sqrt{\frac{(l+m)(l+m-1)}{(2l-1)(2l+1)}}\frac{\partial}{\partial\bar{y}}q_{l-1}^{m-1}\right. \\
&\left.+\sqrt{\frac{(l+m+1)(l+m+2)}{(2l+1)(2l+3)}}\frac{\partial}{\partial\bar{y}}q_{l+1}^{m+1}-\sqrt{\frac{(l-m)(l-m-1)}{(2l-1)(2l+1)}}\frac{\partial}{\partial\bar{y}}q_{l-1}^{m+1}\right] \\
&+\frac{L}{a}\frac{a}{W}\left[\sqrt{\frac{(l+m+1)(l-m+1)}{(2l+1)(2l+3)}}\frac{\partial}{\partial\bar{z}}q_{l+1}^{m}+\sqrt{\frac{(l+m)(l-m)}{(2l-1)(2l+1)}}\frac{\partial}{\partial\bar{z}}q_{l-1}^{m}\right]
\end{aligned} \tag{C.5}$$

where $q_l^m(\bar{\mathbf{r}},s)$ is the expansion coefficient in terms of spherical harmonics and here $\bar{x}$, $\bar{y}$ and $\bar{z}$ are the Cartesian components of $\bar{\mathbf{r}}$ in Eq. (C.1).

Combining Eq. (C.5) with Eq. (C.4) and comparing the terms related to the lth- and $(l-1)$th ranks on the right hand of Eq. (C.4), we can conclude that for any l, the lth-order function $q_l^m(\bar{\mathbf{r}},s)$ has the leading magnitude for small a/W,

$$q_l^m(\bar{\mathbf{r}},s)\propto\left(\frac{a}{W}\right)^l+\cdots, \tag{C.6}$$

where $a/W \ll 1$. In particular, taking $l = 0$ and $m = 0$ in Eq. (C.4) yields

$$\begin{aligned}\frac{\partial}{\partial s}q_0^0(\bar{\mathbf{r}},s) = &- w(\bar{\mathbf{r}})q_0^0(\bar{\mathbf{r}},s) \\ &- \Bigg\{\frac{L}{a}\frac{a}{W}\frac{1}{2}\Big[\sqrt{\frac{2}{3}}\frac{\partial}{\partial\bar{x}}q_1^{-1}(\bar{\mathbf{r}},s) - \sqrt{\frac{2}{3}}\frac{\partial}{\partial\bar{x}}q_1^{1}(\bar{\mathbf{r}},s)\Big] \\ &+ \frac{L}{a}\frac{a}{W}\frac{1}{2i}\Big[\sqrt{\frac{2}{3}}\frac{\partial}{\partial\bar{y}}q_1^{-1}(\bar{\mathbf{r}},s) + \sqrt{\frac{2}{3}}\frac{\partial}{\partial\bar{y}}q_1^{1}(\bar{\mathbf{r}},s)\Big] \\ &+ \frac{L}{a}\frac{a}{W}\Big[\sqrt{\frac{1}{3}}\frac{\partial}{\partial\bar{z}}q_1^{0}(\bar{\mathbf{r}},s)\Big]\Bigg\}. \end{aligned} \tag{C.7}$$

According to Eq. (C.6), the left-hand side has an order or magnitude

$$\frac{\partial}{\partial s}q_0^0(\bar{\mathbf{r}},s) \propto \Big(\frac{a}{W}\Big)^0 \sim 1; \tag{C.8}$$

this implies that if we wish to retain the terms inside the curly brackets on the right-hand side, which is needed to recover the Gausian-chain based MDF, the system must have $L/a(a/W)^2 \sim 1$. Conversely, we speak of this as the assumption to recover the Gaussian-chain limit. As shown in the text, for the current problem in the large L/a limit, this scaling is asymptotically followed. A balance of all terms also indicates that

$$w(\bar{\mathbf{r}}) \propto \Big(\frac{a}{W}\Big)^0 \tag{C.9}$$

is required to keep it in the Gaussian theory. Note that the field itself has a prefactor $\chi L/a$, hence this term is important when

$$\chi L/a \sim (a/W)^0, \tag{C.10}$$

which is the normal range of χ considered in most AB diblock polymer problems.

Setting $l = 1$ in Eq. (C.4), we obtain

$$\frac{\partial}{\partial s}q_1^m(\bar{\mathbf{r}},s) = -w(\bar{\mathbf{r}})q_1^m(\bar{\mathbf{r}},s) - \frac{2L}{a}q_1^m(\bar{\mathbf{r}},s)$$
$$-\left\{\frac{L}{a}\frac{a}{W}\frac{1}{2}\Big[-\sqrt{\frac{(m+1)m}{3}}\frac{\partial}{\partial\bar{x}}q_0^{m-1}(\bar{\mathbf{r}},s) + \sqrt{\frac{(1-m)(-m)}{3}}\frac{\partial}{\partial\bar{x}}q_0^{m+1}(\bar{\mathbf{r}},s)\Big]\right.$$
$$+\frac{L}{a}\frac{a}{W}\frac{1}{2i}\Big[-\sqrt{\frac{(1+m)m}{3}}\frac{\partial}{\partial\bar{y}}q_0^{m-1}(\bar{\mathbf{r}},s) - \sqrt{\frac{(1-m)(-m)}{3}}\frac{\partial}{\partial\bar{y}}q_0^{m+1}(\bar{\mathbf{r}},s)\Big]$$
$$\left.+\frac{L}{a}\frac{a}{W}\Big[\sqrt{\frac{(1+m)(1-m)}{3}}\frac{\partial}{\partial\bar{z}}q_0^m(\bar{\mathbf{r}},s)\Big]\right\} + \frac{L}{a}\mathcal{O}\left(\frac{a}{W}\right)^3 \tag{C.11}$$

The terms insider the curly brackets have an order $L/W \sim \sqrt{L/a}$, which is much greater than the first term on the right-hand side and the term on the left-hand side, both having an order $(a/W) \sim \sqrt{a/L}$, according to Eqs. (C.6) and (C.9). Thus, the above equation can then be written, for $m = 0, 1$ and -1, as

$$2q_1^0(\bar{\mathbf{r}},s) = -\frac{a}{W}\sqrt{\frac{1}{3}}\frac{\partial}{\partial\bar{z}}q_0^0(\bar{\mathbf{r}},s) + \mathcal{O}\left(\frac{a}{W}\right)^3 \tag{C.12}$$

$$2q_1^1(\bar{\mathbf{r}},s) = \frac{a}{W}\frac{1}{2}\sqrt{\frac{2}{3}}\frac{\partial}{\partial\bar{x}}q_0^0(\bar{\mathbf{r}},s) + \frac{a}{W}\frac{1}{2i}\sqrt{\frac{2}{3}}\frac{\partial}{\partial\bar{y}}q_0^0(\bar{\mathbf{r}},s) + \mathcal{O}\left(\frac{a}{W}\right)^3 \tag{C.13}$$

$$2q_1^{-1}(\bar{\mathbf{r}},s) = -\frac{a}{W}\frac{1}{2}\sqrt{\frac{2}{3}}\frac{\partial}{\partial\bar{x}}q_0^0(\bar{\mathbf{r}},s) + \frac{a}{W}\frac{1}{2i}\sqrt{\frac{2}{3}}\frac{\partial}{\partial\bar{y}}q_0^0(\bar{\mathbf{r}},s) + \mathcal{O}\left(\frac{a}{W}\right)^3 \tag{C.14}$$

Finally, substituting Eq. (C.12)-(C.14) into Eq. (C.7), we obtain a closed equation for q_0^0,

$$\frac{\partial}{\partial s}q_0^0(\bar{\mathbf{r}},s) = -w(\bar{\mathbf{r}})q_0^0(\bar{\mathbf{r}},s) + \frac{1}{6}\frac{L}{a}\left(\frac{a}{W}\right)^2\left[\frac{\partial^2}{\partial\bar{x}^2} + \frac{\partial^2}{\partial\bar{y}^2} + \frac{\partial^2}{\partial\bar{z}^2}\right]q_0^0(\bar{\mathbf{r}},s) + \mathcal{O}\left(\frac{a}{W}\right)^2 \tag{C.15}$$

This diffusion-like partial differential equation has an identical form as the MDE resulting from the Gaussian chain model for an orientationally independent propagator $q_0^0(\bar{\mathbf{r}},s)$ [39].

To conclude the argument, we observe that one of the most important assumptions is the existence of a typical length scale in the considered system, $W \sim \sqrt{La}$, in order to recover the Gaussian-chain based MDE; considering the condition $L \gg a$

alone is insufficient in the derivation. This is consistent with how the Gaussian theory was originally developed. Accordingly, we can state that the Gaussian theory breaks down, if we examine a physical system where a typical length scale W significantly differs from the scaling behavior $\sqrt{La}$, which, in our case, can happen when the wormlike chain becomes semiflexible, $L/a \sim 1$ or when a flexible chain is in a highly stretched region, $\chi L/a \gg 1$. In contrast, the wormlike-chain formalism can handle the physical properties covering the entire range of parameters W/a, L/a and $\chi L/a$.

The characteristic length W may vary from system to system. For example, in the study of a wormlike chain confined in a slit, the slit width is on this scale [11, 12]; in the study of a wormlike chain adsorbed in a one-dimensional potential well near a hard-wall surface, the potential-well width is of this scale [28]. While in these systems, and also in the current work, we can discuss the crossover from the rodlike behavior to the Gaussian-chain behavior, there are also wormlike-chain systems in which even in the $L/a \gg 1$ limit, the Gaussian-chain behavior does not exist. For example, the interfacial width of the isotropic-nematic interface is of order a in the $L/a \gg 1$ limit, hence inherently this liquid crystal problem does not have a Gaussian limit [61]; in another example, a closely grafted, $L/a \gg 1$ wormlike brush spans a surface region $W \sim L$, which can be described by the workmlike chain formalism [27], but cannot be dealt with by unrevised Gaussian theories [84].

The analytic derivation that recovers the Gaussian-chain MDE from the wormlike-chain MDE was previously discussed for reduced dimensionality. Morse and Fredrickson considered the interface problem of AB wormlike polymer blends in the long-chain limit, removing the d/ds-term [82]. Schmid and Müller [101] considered the same problem by retaining this term and restricted themselves to variations in z and θ only; their derivation can be generalized to the AB wormlike lamella problem with little modification. Chen and Sullivan [11] considered a wormlike chain confined between two walls where the ground-state dominating approximation can be used, for variables z and θ. The general discussion in this appendix is for a full consideration of variables including $\mathbf{r}$, $\mathbf{u}$ and s.

Appendix D

Anderson mixing

Anderson mixing is a numerical scheme that updates the targeted function by tracing back multiple steps [112]. In our work, we wish to update the fields $w_\gamma(\mathbf{r})$, where γ = A and B, at the kth iteration, where we obtain a new $w^{(k)}_{\gamma,\mathrm{out}}(\mathbf{r})$ on the basis of the initial input $w^{(k)}_{\gamma,\mathrm{in}}(\mathbf{r})$.

First, we define the difference between the input and output fields,

$$d^{(k)}_\gamma(\mathbf{r}) = w^{(k)}_{\gamma,\mathrm{out}}(\mathbf{r}) - w^{(k)}_{\gamma,\mathrm{in}}(\mathbf{r}), \qquad (\gamma = A, B). \tag{D.1}$$

The total deviation, which can be used as a measure of the numerical accuracy, is

$$d_{\gamma,\mathrm{total}} = \left| \frac{\left(d^{(k)}_\gamma(\mathbf{r}), d^{(k)}_\gamma(\mathbf{r}) \right)}{\left(w^{(k)}_{\gamma,\mathrm{out}}(\mathbf{r}), w^{(k)}_{\gamma,\mathrm{out}}(\mathbf{r}) \right)} \right|^{1/2} \tag{D.2}$$

where the definition of an inner product

$$\left(g(\mathbf{r}), h(\mathbf{r}) \right) \equiv \frac{1}{V} \int \mathrm{d}\mathbf{r} g(\mathbf{r}) h(\mathbf{r}) \tag{D.3}$$

is used for two functions $g(\mathbf{r})$ and $h(\mathbf{r})$.

Following Thompson et al [112], we define the element of a symmetric matrix,

$$U_{mn} = \sum_\gamma \left(d^{(k)}_\gamma(\mathbf{r}) - d^{(k-m)}_\gamma(\mathbf{r}), d^{(k)}_\gamma(\mathbf{r}) - d^{(k-n)}_\gamma(\mathbf{r}) \right), \tag{D.4}$$

and the element of a vector

$$V_m = \sum_\gamma \left(d_\gamma^{(k)}(\mathbf{r}) - d_\gamma^{(k-m)}(\mathbf{r}), d_\gamma^{(k)}(\mathbf{r}) \right), \tag{D.5}$$

for $m, n = 1, 2, \cdots, n_r$. Here, n_r is the maximum number of past iterations that are incorporated in the mixing. Calculating the coefficients,

$$A_n = \sum_{m=1}^{n_r} U_{nm}^{-1} V_m, \tag{D.6}$$

we update the fields by

$$w_{\gamma,\mathrm{in}}^{(k+1)}(\mathbf{r}) = w_{\gamma,\mathrm{out}}^{(k)}(\mathbf{r}) + \sum_{n=1}^{n_r} A_n \left(w_{\gamma,\mathrm{out}}^{(k-n)}(\mathbf{r}) - w_{\gamma,\mathrm{out}}^{(k)}(\mathbf{r}) \right), \tag{D.7}$$

which is used as the guessed input for the $(k+1)$th iteration.

Appendix E

Publications

Ying Jiang and Jeff Z. Y. Chen, *Submitted*, (2012);
Wu-Yang Zhang, **Ying Jiang**, and Jeff Z. Y. Chen, *Phys. Rev. E*, **85**, 061710 (2012);
Wu-Yang Zhang, **Ying Jiang**, and Jeff Z. Y. Chen, *Phys. Rev. Lett.*, **108**, 057801 (2012);
Ying Jiang, Wu-Yang Zhang, and Jeff Z. Y. Chen, *Phys. Rev. E*, **84**, 041803 (2011);
Ying Jiang and Jeff Z. Y. Chen, *Macromolecules*, **43**, 10668 (2010);
Mingge Deng, **Ying Jiang**, Haojun Liang and Jeff Z. Y. Chen, *J. Chem. Phys.*, **133**, 034902 (2010);
Mingge Deng, **Ying Jiang**, Haojun Liang and Jeff Z. Y. Chen, *Macromolecules*, **43**, 3455 (2010);

Bibliography

[1] J. C. Adams and P. N. Swarztrauber. *computer code SPHEREPACK 3.2, (2009).* http://www.cisl.ucar.edu/css/software/spherepack/.

[2] M. S. Al-Barwani and M. P. Allen. *Phys. Rev. E*, 62:6706, 2000.

[3] G. B. Arfken and H. J. Weber. *Mathematical Methods for Physicists.* Academic Press, Fifth Edition, 2000.

[4] U. M. Ascher, S. J. Ruuth, and R. J. Spiteri. *Appl. Numer. Math.*, 25:151, 1997.

[5] F. S. Bates and G. H. Fredrickson. *Physics Today*, 52:32, 1999.

[6] F. S. Bates, M. F. Schultz, A. K. Khandpur, S. Förster, J. H. Rosedale, K. Almdal, and K. Mortensen. *Faraday Discuss*, 98:7, 1994.

[7] Y. Bohbot-Raviv and Z. G. Wang. *Phys. Rev. Lett.*, 85:3428, 2000.

[8] T. L. Chantawansri, A. W. Bosse, A. Hexemer, H. D. Ceniceros, C. J. Garcia-Cervera, E. J. Kramer, and Glenn H. Fredrickson. *Phys. Rev. E*, 75:031802, 2007.

[9] B. Chen, X. B. Zeng, U. Baumeister, G. Ungar, and C. Tschierske. *Science*, 307:96, 2005.

[10] J. T. Chen, E. L. Thomas, C. K. Ober, and G. P. Mao. *Science*, 273:343, 1996.

[11] J. Z. Y. Chen and D. E. Sullivan. *Macromolecules*, 39:7769, 2006.

[12] J. Z. Y. Chen, D. E. Sullivan, and X. Q. Yuan. *Macromolecules*, 40:1187, 2007.

[13] W. Chen and D. G. Gray. *Langmuir*, 18:633, 2002.

[14] W. L. Chen, T. Sato, and A. Teramoto. *Macromolecules*, 29:4283, 1996.

[15] W. L. Chen, T. Sato, and A. Teramoto. *Macromolecules*, 32:1549, 1999.

[16] Z. Y. Chen. *Macromolecules*, 26:3419, 1993.

[17] Z. Y. Chen. *Phys. Rev. E*, 47:3765, 1993.

[18] Z. Y. Chen and J. Noolandi. *Phys. Rev. A*, 45:2389, 1992.

[19] B. K. Cho, Y. W. Chung, and M. Lee. *Macromolecules*, 38:10261, 2005.

[20] E. W. Cochran, C. J. Garcia-Cervera, and G. H. Fredrickson. *Macromolecules*, 39:2449, 2006.

[21] J. P. Cotton and F. Hardouin. *Prog. Polym. Sci.*, 22:795, 1997.

[22] A. A. Craig and C. T. Imrie. *Macromolecules*, 28:3617, 1995.

[23] A. A. Craig and C. T. Imrie. *Macromolecules*, 32:6215, 1999.

[24] S. M. Cui, O. Akcakir, and Z. Y. Chen. *Phys. Rev. E*, 51:4548, 1995.

[25] D. Düchs and D. E. Sullivan. *J. Phys.: Condens. Matter*, 14:12189, 2002.

[26] P. G. de Gennes. *The Physics of Liquid Crystals, 2nd Edition.* Clarendon, Oxford, 1993.

[27] M. G. Deng, Y. Jiang, H. J. Liang, and J. Z. Y. Chen. *Macromolecules*, 43:3455, 2010.

[28] M. G. Deng, Y. Jiang, H. J. Liang, and J. Z. Y. Chen. *J. Chem. Phys.*, 133:034902, 2010.

[29] Z. Dogic and S. Fraden. *Langmuir*, 16:7820, 2000.

[30] Z. Dogic, K. R. Purdy, E. Grelet, M. Adams, and S. Fraden. *Phys. Rev. E*, 69:051702, 2004.

[31] M. Doi and S. F. Edwards. *The Theory of Polymer Dynamics.* Oxford Univ. Press, New York, 1986.

[32] M. Doi and N. Kuzuu. *J. Appl. Polym. Sci., Polym. Symp.*, 41:65, 1985.

[33] B. Y. Drovetsky, A. J. Liu, and C. H. Mak. *J. Chem. Phys.*, 111:4334, 1999.

[34] S. F. Edwards. *Proc. Phys. Soc. London*, 85:613, 1965.

[35] R. P. Feynman and A. R. Hibbs. *Quantum Mechanics and Path Integrals.* McGraw-Hill Book Company, New York, 1965.

[36] R. A. Fisher and W. K. Bischel. *Appl. Phys. Lett.*, 23:661, 1973.

[37] R. A. Fisher and W. K. Bischel. *J. Appl. Phys.*, 46:4921, 1975.

[38] P. J. Flory. *Principles of Polymer Chemistry.* Cornell University Press, Ithaca, 1953.

[39] G. H. Fredrickson. *The Equilibrium Theory of Inhomogeneous Polymers.* Oxford University Press, 2006.

[40] G. H. Fredrickson, V. Ganesan, and F. Drolet. *Macromolecules*, 35:16, 2002.

[41] K. F. Freed. *Adv. Chem. Phys.*, 22:1, 1972.

[42] D. Frenkel and B. Smit. *Understanding Molecular Simulation: From Algorithms to Applications.* Academic Press, 2002.

[43] P. Friedel, A. John, D. Pospiech, D. Jehnichen, and R. R. Netz. *Macromol. Theory Simul.*, 11:785, 2002.

[44] M. Frigo and S. G. Johnson. *Proc. ICASSP*, page 1381, 1998.

[45] V. Ganesan, L. Khounlavong, and V. Pryamitsyn. *Physical Rev. E*, 78:051804, 2008.

[46] J. Gao, W. D. Song, P. Tang, and Y. L. Yang. *Soft Matter*, 7:5208, 2011.

[47] I. S. Gradshteyn and I. M. Ryzhik. *Tables of Integrals, Series, and Products*. Academic, New York, 1980.

[48] A. Grosberg. *Theoretical and Mathematical Models in Polymer Research: Modern Methods in Polymer Research and Technology (Polymers, Interfaces and Biomaterials)*. Academic Press, Boston, 1998.

[49] A. Grosberg and A. R. Khokhlov. *Statistical physics of macromolecules*. AIP, New York, 1994.

[50] A. Y. Grosberg and D. V. Pachomov. *Liq. Cryst.*, 10:539, 1991.

[51] A. Halperin. *Macromolecules*, 23:2724, 1990.

[52] I. W. Hamley. *Developments in Block Copolymer Science and Technology*. Wiely, New York, 2004.

[53] E. Helfand. *J. Chem. Phys.*, 62:999, 1975.

[54] E. Helfand and A. M. Sapse. *J. Chem. Phys.*, 62:1327, 1975.

[55] E. Helfand and Y. Tagami. *J. Polym. Sci. B*, 9:741, 1971.

[56] E. Helfand and Y. Tagami. *J. Chem. Phys.*, 57:1812, 1972.

[57] E. Helfand and Y. Tagami. *J. Chem. Phys.*, 56:3592, 1972.

[58] R. C. Hidalgo, D. E. Sullivan, and J. Z. Y. Chen. *J. Phys.: Condens. Matter*, 19:376107, 2007.

[59] R. Holyst and A. Poniewierski. *Phys. Rev. A*, 38:1527, 1988.

[60] K. M. Hong and J. Noolandi. *Macromolecules*, 14:727, 1981.

[61] Y. Jiang and J. Z. Y. Chen. *Macromolecules*, 43:10668, 2010.

[62] Y. Jiang and J. Z. Y. Chen. *Phys. Rev. Lett.*, 110:138305, 2013.

[63] Y. Jiang, W. Y. Zhang, and J. Z. Y. Chen. *Phys. Rev. E*, 84:041803, 2011.

[64] A. K. Khandpur, S. Foerster, F. S. Bates, I. W. Hamley, A. J. Ryan, W. Bras, K. Almdal, and K. Mortensen. *Macromolecules*, 28:8796, 1995.

[65] A. R. Khokhlov and A. N. Semenov. *Physica*, 112:605, 1982.

[66] M. Kikuchi, L. T. N. Lien, A. Narumi, Y. Jinbo, Y. Izumi, K. Nagai, and S. Kawaguchi. *Macromolecules*, 41:6564, 2008.

[67] D. L. Koch and O. G. Harlen. *Macromolecules*, 32:219, 1999.

[68] O. Kratky and G. Porod. *Recl. Trav. Chim.*, 68:1106, 1949.

[69] J. D. Lambert. The initial value problem. In *Numerical Methods for Ordinary Differential Systems*. John Wiley & Sons: Chichester, 1991.

[70] Leon Lapidus and George F. Pinder. *Numerical Solution of Partial Differential Equations in Science and Engineering*. Wiley, 1982.

[71] L. Leibler. *Macromolecules*, 13:1602, 1980.

[72] H. N. W. Lekkerkerker, P. Coulon, R. van der Haegen, and R. Deblieck. *J. Chem. Phys.*, 80:3427, 1984.

[73] E. M. Lennon, K. Katsov, and G. H. Fredrickson. *Phys. Rev. Lett.*, 101:138302, 2008.

[74] A. J. Liu and G. H. Fredrickson. *Macromolecules*, 26:2817, 1993.

[75] W. Maier and A. Saupe. *Z. Naturforsch*, A13:564, 1958.

[76] M. W. Matsen. *J. Chem. Phys*, 104:7758, 1996.

[77] M. W. Matsen. *J. Phys.: Condens. Matter*, 14:R21, 2002.

[78] M. W. Matsen and C. Barrett. *J. Chem. Phys.*, 109:4108, 1998.

[79] M. W. Matsen and F. S. Bates. *Macromolecules*, 29:1091, 1996.

[80] W. E. McMullen. *Phys. Rev. A*, 38:6384, 1988.

[81] S. Mehraeen, B. Sudhanshu, E. F. Koslover, and A. J. Spakowitz. *Physical Rev. E*, 77:061803, 2008.

[82] D. C. Morse and G. H. Fredrickson. *Phys. Rev. Lett.*, 73:3235, 1994.

[83] R. R. Netz and M. Schick. *Phys. Rev. Lett.*, 77:302, 1996.

[84] R. R. Netz and M. Schick. *Macromolecules*, 31:5105, 1998.

[85] P. W. Oakes, J. Viamontes, and J. X. Tang. *Phys. Rev. E*, 75:061902, 2007.

[86] T. Odijk. *Macromolecules*, 19:2313, 1986.

[87] B. D. Olsen and R. A. Segalman. *Macromolecules*, 38:10127, 2005.

[88] B. D. Olsen and R. A. Segalman. *Macromolecules*, 39:7078, 2006.

[89] B. D. Olsen, M. Shah, V. Ganesan, and R. A. Segalman. *Macromolecules*, 41:6809, 2008.

[90] L. Onsager. *Ann. N. Y. Acad. Sci.*, 51:627, 1949.

[91] V. Percec and A. Keller. *Macromolecules*, 23:4347, 1990.

[92] X. L. Piao, J. S. Kim, Y. K. Yun, J. L. Jin, and S. K. Hong. *Macromolecules*, 30:2294, 1997.

[93] W. H. Press, S. A. Teukolsky, W. T. Vetterling, and B. P. Flannary. *Numerical Recipes in C, 2nd Edition*. Cambridge University Press, 1992.

[94] V. Pryamitsyn and V. Ganesan. *J. Chem. Phys.*, 120:5284, 2004.

[95] N. Puech, E. Grelet, P. Poulin, C. Blanc, and P. van der Schoot. *Phys. Rev. E*, 82:020702(R), 2010.

[96] A. Rapini and M. J. Papoular. *J. Phys. (Paris), Colloq.*, 30:C4–54, 1969.

[97] M. W. Reinsch. *J. Math. Phys.*, 41:2434, 2000.

[98] P. Riala, A. Andreopoulou, J. Kallitsis, A. Gitsas, and G. Floudas. *Polymers*, 47:7241, 2006.

[99] D. Rousseau, J. D. Marty, M. Mauzac, P. Martinoty, A. Brandt, and J. M. Guenet. *Polymer*, 44:2049, 2003.

[100] N. Saito, K. Takahashi, and Y. Yunoki. *J. Phys. Soc. Jpn*, 22:219, 1967.

[101] F. Schmid and M. Müller. *Macromolecules*, 28:8639, 1995.

[102] A. N. Semenov and S. V. Vasilenko. *Zh. Eksp. Teor. Fiz.*, 90:124, 1986.

[103] M. Shah and V. Ganesan. *J. Chem. Phys.*, 130:054904, 2009.

[104] K. Shundyak and R. van Roij. *J. Phys. Condens. Matter*, 13:4789, 2001.

[105] C. Singh, M. Goulian, J. Liu. Andrea, and G. H. Fredrickson. *Macromolecules*, 27:2974, 1994.

[106] W. D. Song, P. Tang, F. Qiu, Y. L. Yang, and A. C. Shi. *Soft Matter*, 7:929, 2011.

[107] W. D. Song, P. Tang, H. D. Zhang, Y. L. Yang, and A. C. Shi. *Macromolecules*, 42:6300, 2009.

[108] A. J. Spakowitz and Z.-G. Wang. *Physical Rev. E*, 72:041802, 2005.

[109] P. Stasiak and M. W. Matsen. *Eur. Phys. J. E*, 34:110, 2011.

[110] P. N. Swarztrauber. *Mon. Weather Rev.*, 121:3415, 1993.

[111] P. N. Swarztrauber. *J. Comput. Phys.*, 159:213, 2000.

[112] R. B. Thompson, K. Ø. Rasmussen, and T. Lookman. *J. Chem. Phys.*, 120:31, 2004.

[113] G. Tzeremes, K. Ø. Rasmussen, T. Lookman, and A. Saxena. *Phys. Rev. E*, 65:041806, 2002.

[114] A. M. Urbas, M. Maldovan, P. DeRege, and E. L. Thomas. *Adv. Mater.*, 14:1850, 2002.

[115] P. van der Schoot. *J. Phys. Chem. B*, 103:8804, 1999.

[116] M. Verswyvel and G. Koeckelberghs. *Polym. Chem.*, 3:3203, 2012.

[117] J. Viamontes, P. W. Oakes, and J. X. Tang. *Phys. Rev. Lett.*, 97:118103, 2006.

[118] G. J. Vroege and T. Odijk. *Macromolecules*, 21:2848, 1988.

[119] R. Wang and Z. G. Wang. *Macromolecules*, 43:10096, 2010.

[120] D. R. M. Williams and G. H. Fredrickson. *Macromolecules*, 25:3561, 1992.

[121] H. Yamakawa. *Helical Wormlike Chains in Polymer Solutions*. Springer-Verlag, Berlin, 1997.

[122] G. Yang, P. Tang, and Y. L. Yang. *Macromolecules*, 45:3590, 2012.

[123] W. Y. Zhang, Y. Jiang, and J. Z. Y. Chen. *Phys. Rev. Lett.*, 108:057801, 2012.

[124] W. Y. Zhang, Y. Jiang, and J. Z. Y. Chen. *Phys. Rev. E*, 85:061710, 2012.

[125] W. Zhao, T. P. Russell, and G. M. Grason. *J. Chem. Phys.*, 137:104911, 2012.

[126] B. L. Zhuang and Z. G. Wang. *Macromolecules*, 45:6220, 2012.